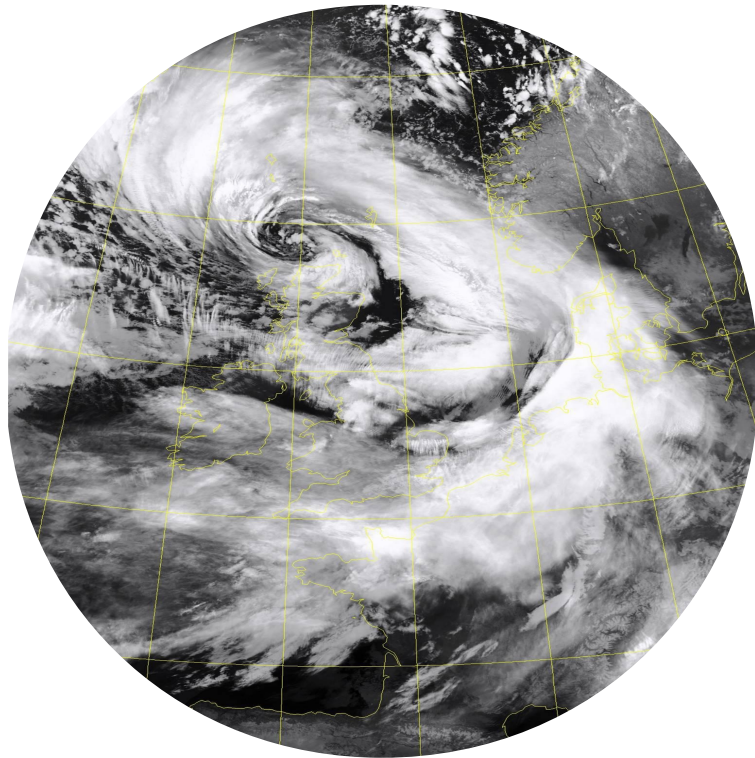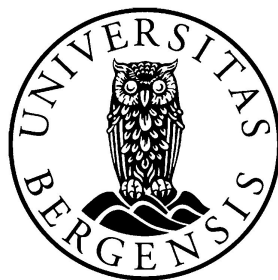# Dynamics and Predictability of the Extreme Extratropical Cyclone Nina

A Master Thesis in Meteorology by

Lars Andreas Selberg

Geophysical Institute

University of Bergen

1 June 2016

The front page image is a satellite image of the extreme extratropical cyclone Nina at approximately six hours before landfall at the west coast of Norway. Image taken by the Dundee Satellite[1]

---

[1]http://www.sat.dundee.ac.uk/

Abstract

An extreme extratropical cyclone struck western Norway at 12 UTC 10 January 2015 causing significant damage to property due to extreme winds. The European region has a history of being struck by extreme cyclones that cause significant damage to property. Thus, it is important to investigate how these cyclones evolve and to find the cause of their strength.

In this study a synoptic analysis of Nina, following a method developed by Boettcher and Wernli (2013), is performed. From the method, it was found that the synoptic environment during Nina featured large low level baroclincity and high moisture content, which are favorable ingredients for formation of a Diabatic Rossby Vortex. It was also found that the presence of an upstream upper level trough, eventually overtaking Nina, caused explosive intensification of the cyclone. Based on the synoptic analysis, strong evidence was found to conclude that Nina evolved similar to a Diabatic Rossby Vortex.

In addition, due to significant forecast uncertainty of Nina with respect to the track and location, a sensitivity analysis of the cyclone was performed. From the sensitivity analysis it was found that Nina was heavily influenced by moisture in the low-to mid-levels of the atmosphere, providing additional evidence that Nina evolved similar to a Diabatic Rossby Vortex. By choosing kinetic energy and potential vorticity as response functions in an Adjoint Modeling system at the time of landfall of the cyclone, it was possible to relate the strength and track of Nina to the dynamics at the initial nonlinear field of a forecast. It was found where the initial nonlinear model field could be perturbed to create a stronger storm, and where the initial nonlinear model field could be perturbed to change the track of Nina at landfall.

Preceding the synoptic analysis and sensitivity analysis of Nina all relevant theory needed to explain the results is presented. For the sensitivity analysis an accuracy test was performed, to show that the results from the adjoint modeling system are realistic and consistent with the output from the nonlinear model.

Acknowledgements

Contents

List of Abbreviations

AM   Adjoint Model

APE   Available Potential Energy

CAA   Cold Air Advection

COAMPS   Coupled Ocean/Atmosphere Mesoscale Predicition System

COVIP   COAMPS Visualization In Python

DH   Diabatic Heating

DRV   Diabatic Rossby Vortex

ECMWF   European Centre for Medium-Range Forecasting

IFS   Integrated Forecasting System

KE   Kinetic Energy

MET   Norwegian Meteorological Institute

NLM   Nonlinear Model

PV   Potential Vorticity

QG   Quasi-Geostrophic

SLP   Sea Level Pressure

TLM   Tangent Linear Model

UTC   Coordinated Universal Time

WAA   Warm Air Advection

1   Introduction

Extratropical cyclones are low pressure systems that dominate the day-to-day weather conditions in the middle and high latitudes (Wernli and Schwierz, 2006). Everyone that lives within the middle and high latitudes can relate to extratropical cyclones in one way or another. The extratropical cyclones bring wind and precipitation in the form of rain or snow. Thus, in many cases they have a an effect on the day-to-day activities of the general public.
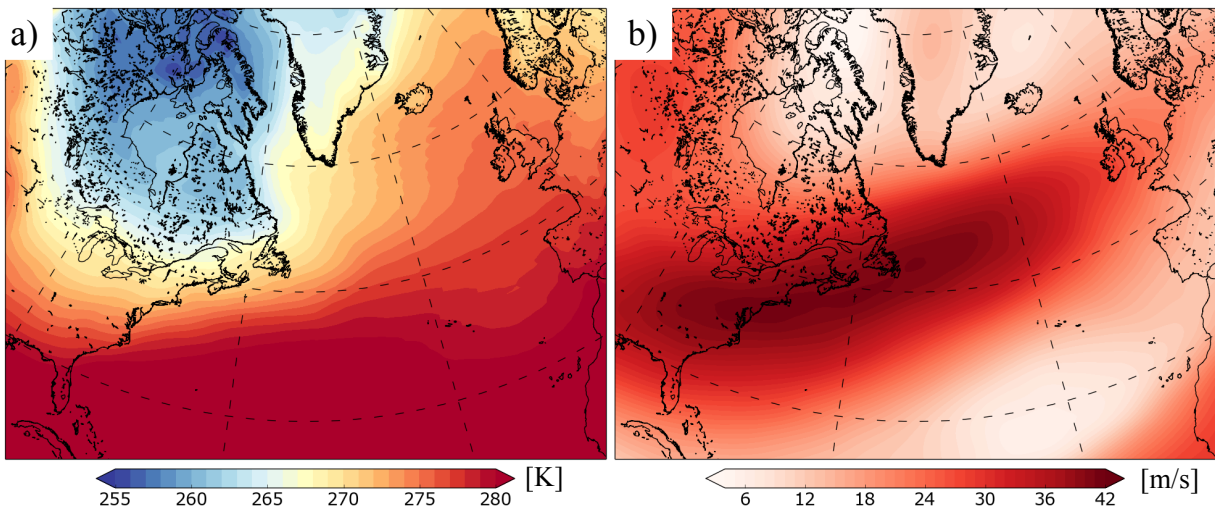
Figure 1: 92 day long term mean: 1 November 2014 - 31 January 2015, ERA-Interim reanalysis data. (a): 950 hPa temperature (K), (b): 250 hPa total horizontal wind component (m/s)

Extratropical cyclones form in the region where the temperature has the largest change with latitude. This region is located within 30°- 60° latitude (see figure 1a) on average. The change of temperature with latitude gives rise to vertical wind shear and a jet stream. A jet stream is a narrow, elongated region of strong winds at about $\sim$ 200-300 hPa, the height of the dynamic tropopause (see figure 1b). The extratropical cyclones tend to follow the position of the jet stream. On occasion, when the jet stream is anomalously strong, some of these extratropical cyclones will evolve into extreme systems that are hazardous to people living in its pathway (Rommetveit, 2014). When the winds and precipitation within these systems reach a certain threshold, defined by the Norwegian Meteorological Institute (MET Norway)[2], the extratropical cyclone is defined as extreme, and an extreme

---

[2]http://www.yr.no/artikkel/hva-er-et-ekstremvaer_1.7890946

weather warning is issued for the communities located in its pathway. When MET Norway monitor an extreme extratropical cyclone, they name the system to aid communication with the public[3].

1.1   Genesis, lifecycle and predictability of Nina
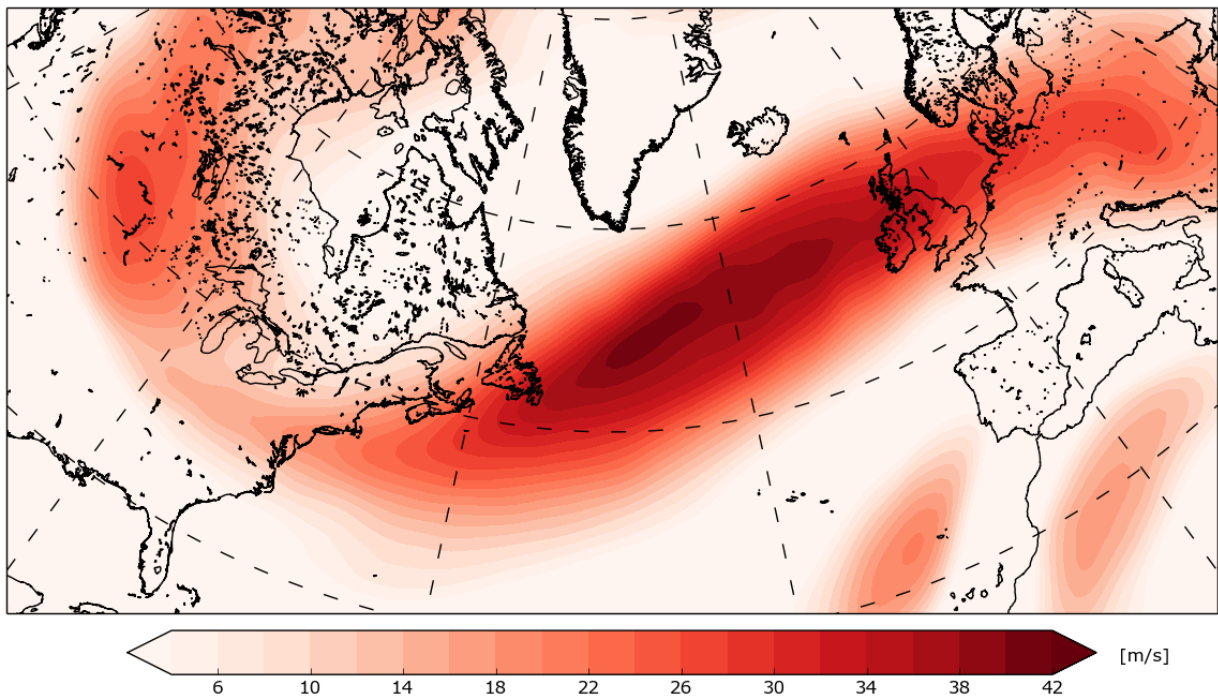
Figure 2: The difference between the average total horizontal wind (m/s) 7 January 2015 - 11 January 2015 and winter season (December, January, February), 1979 - 2015 at 250 hPa. ERA-interim reanalysis data.

A highly anomalous jet stream was located over the North Atlantic 7 January 2015 - 11 January 2015. Compared to the average jet stream from 1979 - 2015, the jet stream from 7 January 2015 - 11 January 2015 was about $\sim$ 42 m/s stronger (see figure 2). During this highly anomalous jet stream, an extratropical cyclone was formed. This extratropical cyclone evolved into an intense weather that struck western Norway with extreme winds and heavy precipitation at about 12 UTC 10 January 2015. The extreme extratropical cyclone was named 'Nina' by MET Norway. During Nina the maximum average wind over

---

[3]http://met.no/Meteorologi/A_varsle_varet/Varsling_av_farlig_var/

ten minutes was about ~ 30 m/s and wind gusts reached 45 m/s along the west coast from Vest-Agder to Møre and Romsdal (see figure 3). In Bergen and Stavanger, the two biggest cities along the Norwegian west coast, maximum surface winds over ten minutes reached a magnitude of 21.8 m/s and 24.9 m/s, and wind gusts reached 37.7 m/s and 34.4 m/s, respectively. In some local regions accumulated precipitation reached > 70 mm/24h, for instance in Voss in the county Hordaland (see figure 3).
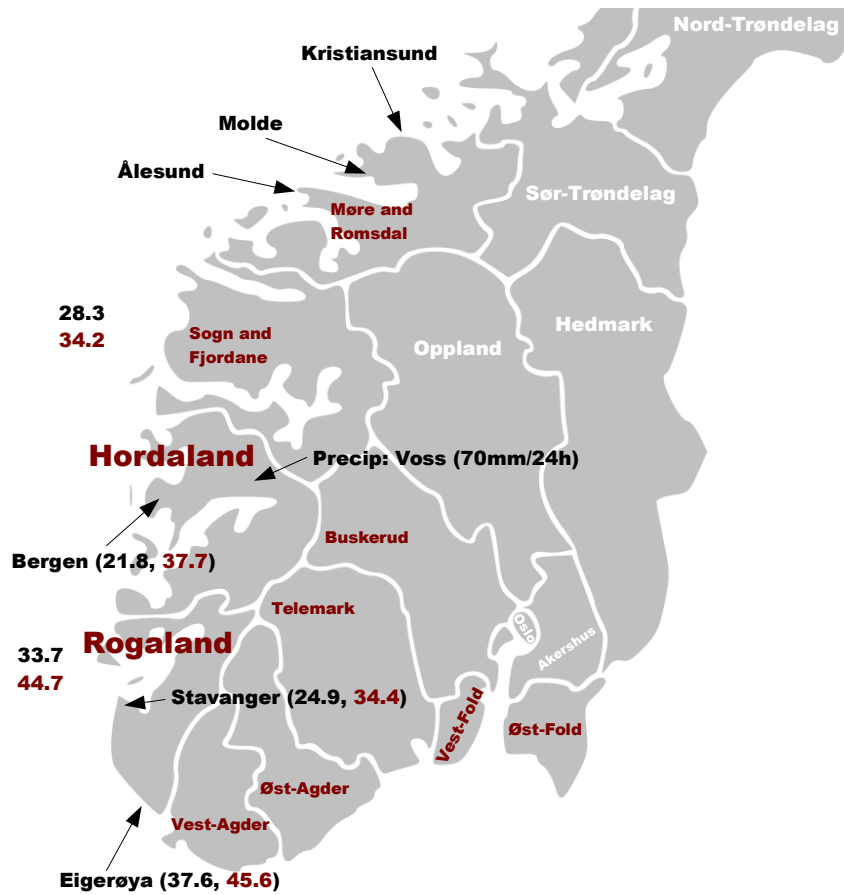
Figure 3: Map of southern Norway, showing the counties affected by Nina (red, font size adjusted according to the economical impact of Nina). Counties not economically impacted by Nina are given in white. Maximum average wind over ten minutes (black) and wind gusts (red), by the coast, in Bergen, Stavanger and Eigerøya during Nina is shown. To indicate the significance of precipitation during Nina, accumulated precipitation over 24 hours at Voss in Hordaland is shown. Maximum average wind over ten minutes and wind gusts are from the External Extreme Weather Report of Nina (Olsen *et al.*, 2015). Precipitation from Yr[4].

3
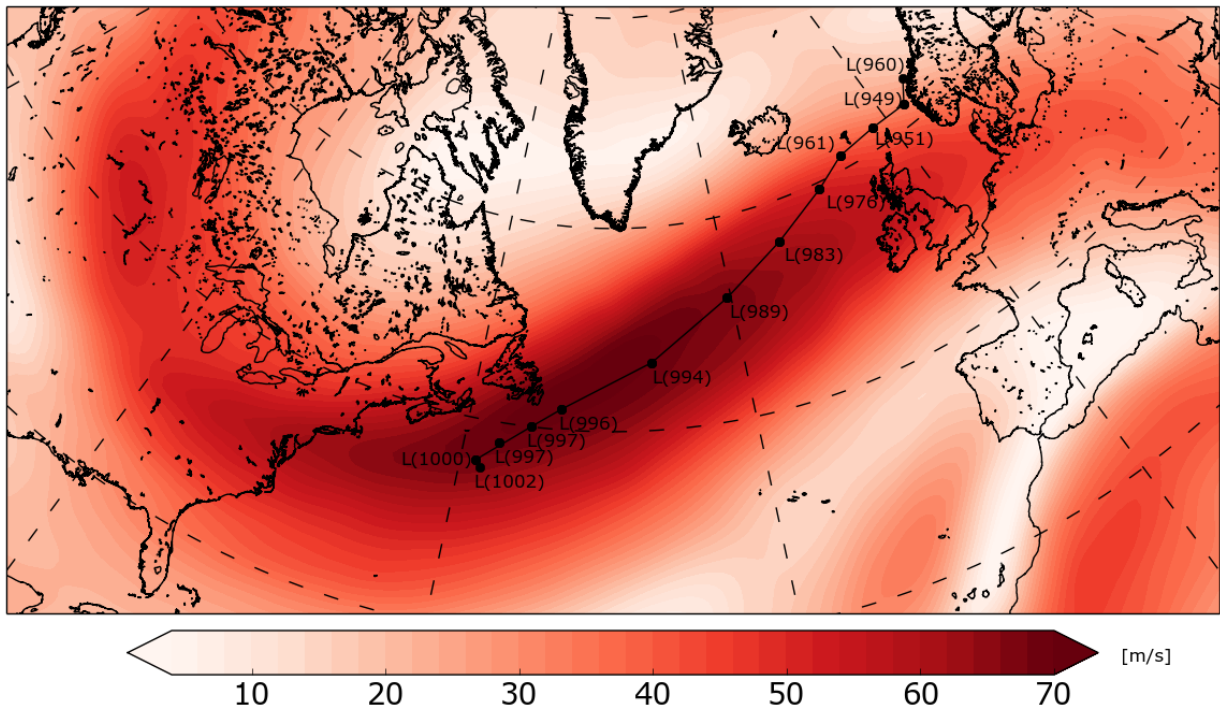
Figure 4: The average total horizontal wind (m/s) at 250 hPa from 7 January - 11 January 2015. The black line is the track of Nina. The black circles show the position of the minimum sea level pressure (SLP) of Nina every 6 hours (00, 06, 12, 18 UTC) from genesis to landfall (18 UTC 7 January 2015 - 12 UTC 10 January 2015). The 'L' together with the numbers signifies the minimum SLP (hPa) of the cyclone every timestep.

Genesis (first minimum SLP signal) of Nina took place 18 UTC 7 January 2015 southeast of Nova Scotia. Nina propagated beneath the jet stream across the North Atlantic to western Norway, and decayed north of Møre and Romsdal 18 UTC 11 January, 2015 (see figure 3 and 4).

The life cycle of Nina is divided into four stages following Boettcher and Wernli (2013): A genesis phase (18 UTC 7 January 2015 - 12 UTC 8 January, 2015), a propagation phase (12 UTC 8 January 2015 - 12 UTC 9 January 2015), an intensification phase (12 UTC 9 January 2015 - 12 UTC 10 January 2015) and a decay phase (12 UTC 10 January 2015 - 18 UTC 11 January 2015). The life cycle stages of Nina are based on the development of the mean SLP in the center of the cyclone with time (see figure 5). During the genesis stage, there was little intensification ($\sim$ 0.3 hPa/hr). During the propagation phase the cyclone underwent modest intensification ($\sim$ 0.6 hPa/hr). During the intensification stage the cyclone underwent an extreme deepening of $\sim$ 1.4 hPa/hr.

---

[4]http://www.yr.no/place/Norway/Hordaland/Voss/Voss/detailed_statistics.html

Sanders and Gyakum (1980) defined a classification for cyclones that underwent extreme pressure drops for twenty four hours over the average latitude during the intensification phase (see section 2.1 and 11, for more information on this classification of a cyclone). If the value calculated from equation 11 is at least 1 Bergeron the cyclone can be classified as a 'bomb'. With the extreme pressure drop of $\sim$ 1.4 hPa/hr, and 1.4 Bergeron, Nina is classified as a 'bomb'. The fact that Nina classifies as a 'bomb' cyclone indicates the extreme nature of the cyclone and provides further motivation to better understand this event.

The decay phase of Nina is defined as the time when the SLP in the center of Nina started increasing, approximately at landfall, 12 UTC 10 January 2015 (see figure 5).
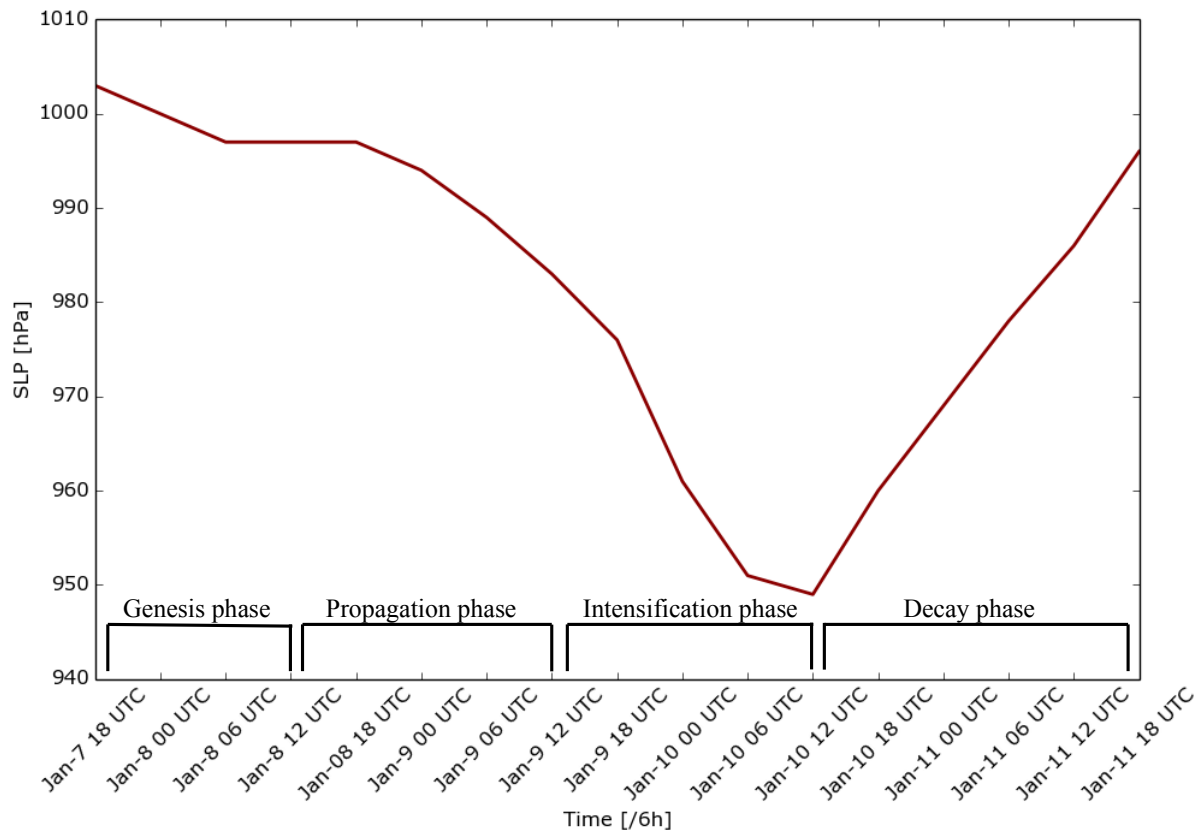
Figure 5: Mean SLP (hPa) in center of Nina versus time (/6h). The four stages of Nina's life cycle have been marked.

There was large forecast uncertainty for Nina. Due to the relatively small scale of the cyclone, a change in the track would have a large impact on where the strongest winds would strike (Engdahl, 2015). The impact of the storm depended heavily on location, as

5

there are several cities of varying size along the Norwegian coast. Another issue regarding the storm was its location. The location uncertainty made it difficult to determine the time Nina would strike the west coast of Norway. The combination of the track and location uncertainty made it extra challenging for MET Norway to forecast Nina[5].

The European Centre for Medium-Range Forecasting (ECMWF) Integrated Forecasting System (IFS) (see section 3.1.4 for details of this model) provided forecasts and analysis fields of Nina. By taking the difference between a forecast of Nina initialized 12 UTC 8 January 2015 (2 days before landfall) and an analysis field, both from the ECMWF IFS model, the large uncertainty of where Nina could make landfall at the west coast of Norway can be seen (see figure 6). The forecast indicated that the cyclone would strike the cities Ålesund, Molde, and Kristiansund in Møre and Romsdal the hardest (see figure 3). The analysis fields, created after Nina struck the Norwegian coastline, shows that the system made landfall much further south causing the maximum winds to strike the counties Hordaland and Rogaland.
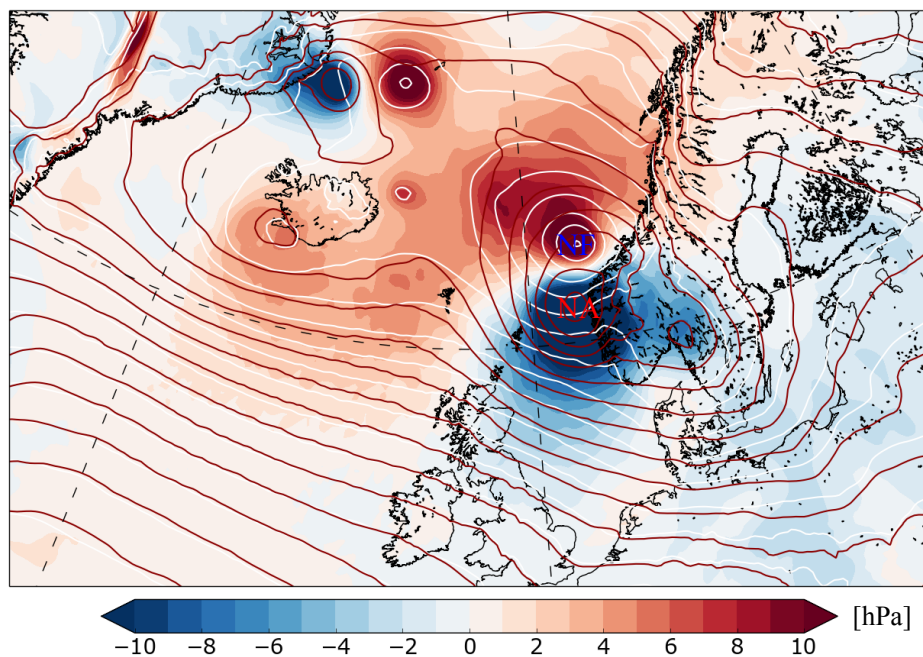
Figure 6: Mean SLP Analysis field - Mean SLP Forecast field (shading, hPa) from the ECMWF IFS. Analysis mean SLP (red contours, 5 hPa interval). A two day forecast of the mean SLP with initialization time 12 UTC 8 January 2015 (white contours, 5 hPa interval). 'NF' designates the position of Nina by the forecast, while 'NA' designates the position of Nina by the analysis.

---

[5]http://www.yr.no/artikkel/_-dette-er-fryktelig-vanskelig-1.12138200

1.2   Aftermath of Nina

Due to Nina's extreme wind and precipitation upon landfall in western Norway, Nina caused significant damage to property. Figure 7, shows an example of the influence of the extreme wind from the cyclone. The winds tore down many trees over roads, houses and electrical equipment, and generated large waves. Up to 170,000 people lost power and telephone service for several days. Hordaland, and Rogaland was struck the hardest with 90% of the damage. In Bergen there were five registered personal injuries (Olsen *et al.*, 2015).

The remaining reports were from Sogn and Fjordane, Buskerud, Telemark, Vest-Agder, Øst-Agder, Vest-fold and Øst-fold (see figure 3). By 22 January 2015 the estimated cost of Nina's damage was approximately 450 million NOK. The high damage cost was due to Nina's intense winds which struck more densely populated areas like Bergen and Stavanger. Nina was one of the five strongest storms to strike western Norway with a westerly/northwesterly wind direction in the last 60 years. Last time the westerly winds were this anomalous over such a large area was 23 January 1994 (Olsen *et al.*, 2015).

Figure 7: Examples of large waves generated by Nina (left) and a tree that was tore down by the extreme wind (right). Pictures taken from Bergensavisen[6].

1.3   Motivation and history

It is not the first time Norway, and other neighbouring countries in Europe, have been struck by extreme extratropical cyclones. Examples of other extreme systems that struck the European regions include; 'New years storm', 1 January 1992 (Harstveit and

---

[6]http://www.ba.no/nyheter/ekstremvaret-nina-gar-fra-orkan-til-frisk-bris/s/1-41-7744193

Aune, 1992), 'Anatol', 2 December 1999 (Ulbrich *et al.*, 2001), 'Lothar', 24 December 1999 (Wernli *et al.*, 2002), 'Martin', 28 December 1999 (Ulbrich *et al.*, 2001), 'Xynthia', 27 February 2010 (Doyle *et al.*, 2013), 'Dagmar', 26 December 2011 (Olsen *et al.*, 2015). Norway and Europe receive most of these extratropical cyclones because the European region is situated at the termination of the North Atlantic storm track.

The North Atlantic storm track is known as the average region where the extratropical cyclones form (Dacre *et al.*, 2012). Since the jet stream's average position is in the midlatitudes, with a southwest to northeast orientation towards Norway and Europe (see figure 1b), and since the extratropical cyclones tend to follow the jet stream, the systems are guided towards this region (Wernli and Schwierz, 2006). As long as the average position of the jet stream does not change, the European region will keep receiving the impact of extratropical cyclones, because of the jet stream position.

Factors which determine how extratropical cyclones evolve, determines what type of destruction they bring. Prevalence of strong winds in a storm may impact mass transportation and result in power loss due to destruction of power lines, as in the case of Nina (see figure 7). Strong winds may also generate large waves and high water levels (National Academy of Sciences, 1963). The large waves may cause destruction of bridges and other infrastructure along the coastline. If there is prevalence of strong precipitation in the storm, it may lead to avalanches, floods and mud slides resulting in damage to houses. Some of these extreme systems even lead to casualties. 'Xynthia, a storm which struck the central European regions 27 February 2010, generated waves as high as eight meters and caused sixty four casualties (Liberato *et al.*, 2013). The high number of casualties caused by 'Xynthia' underscores the importance of further investigation of extratropical cyclones

By investigating the dynamics of extratropical cyclones, an increased understanding of why these system have such a impact may be obtained. Research may also help improve our ability to predict these high-impact systems further in advance. An increased understanding of the dynamics of the system and how it interacts with orography during landfall may also enhance our ability to forecast the strength and location of the hazardous features in relation to these extratropical cyclones. Identifying a potentially dangerous extratropical cyclone at an earlier stage and accurately estimating the strength of the winds and the amount of precipitation, is of vital importance, because it may increase the preparedness of the public. If an extreme weather warning is issued for the wrong area or if the general public is not warned that an extreme extratropical cyclone is on its way, it could have a much more extensive impact, particularly for those not properly warned in advance. This

was the case for the 'New Years Storm' that struck Norway 1 January 1992; most of the general public was not aware of this cyclone, and thus it caused much more damage to property, because the general public that was struck by the cyclone was not prepared[7]. A false warning or a lack of distribution of extreme weather warnings may also destroy the credibility of the forecasters. The increased preparedness of the public can mitigate the economic impact for the country that is struck by a hazardous system, and it may even save lives.

Because of the position of Europe relative to the North Atlantic Storm track (see figure 1 and for instance figure 1 in Dacre *et al.* (2012)), this region will receive more extreme extratropical cyclones. Because of the large economical impact the extreme extratropical cyclones can have (for instance the case of Nina, see section 1.2), and the fact that the extreme systems can take lives, like for the Xynthia storm (Liberato *et al.*, 2013), continued research of extratropical cyclones is important.

1.4   Outline

Previous research of the atmosphere has provided meteorological tools (Holton and Hakim, 2012; Markowski and Richardson, 2010; Wallace and Hobbs, 2006) that can be utilized for identification of atmospheric features like extratropical cyclones. Research of extratropical cyclones has provided categories of which the cyclones can undergo, to better define their dynamics (Petterssen and Smebye, 1971; Deveson *et al.*, 2002; Moore and Montgomery, 2004; Boettcher and Wernli, 2013).

By utilizing the meteorological tools (see section 2 and 3.1.1, for details on the meteorological tools utilized in this study) and methods (see section 3, for details on methods utilized in this study) for classification of extratropical cyclones, a synoptic analysis of Nina is performed to learn how this extratropical cyclone underwent cyclogenesis and evolved into such an intense and dangerous system. In section 3.1, the method for the synoptic analysis is presented. In section 4, the synoptic analysis is provided, with a discussion of salient points.

Since there was significant forecast uncertainty when forecasting Nina, an adjoint model is utilized (Kalnay, 2003) to address the strength of the winds and the track of Nina with respect to its dynamics. The sensitivities calculated by the adjoint model can be utilized to see which parameters were of importance during the evolution of the storm and where

---

[7]http://met.no/Varsling+av+farlig+v%C3%A6r+-+ekstremv%C3%A6r.9UFRrWYm.ips

the forcing regions are located with respect to Nina. By locating sensitive regions with respect to an initial nonlinear field, the parameters in the nonlinear field within the sensitive regions can be adjusted, so that it can be given an understanding of what makes the winds stronger and which adjustments changes the track in relation to the dynamics of Nina at landfall. There are other valid methods of parameter estimation available, such as ensemble kalman filter, extended kalman filter, and 4DVar (Kalnay, 2003), but in this study the use of an adjoint model was preferred.

In section 3.2, the method for the sensitivity analysis is explained, in addition to the reason for the choice of forecast aspects. The results and discussion of the sensitivity analysis is presented in section 5. A summary and conclusion is given in section 6. Finally, suggestions of further research of Nina is given in section 7. But before going into the method and results some general theory must be explained.

2 Theory

2.1 Extratropical cyclones

A typical extratropical cyclone has a warm front and a trailing cold front (see figure 8). Following Markowski and Richardson (2010), a front refers to the boundary between two air masses of different densities, they are elongated zones of strong horizontal temperature gradients. A front intensifies (weakens) when the horizontal density gradient increases (decreases) in magnitude and this is defined as frontogenesis (frontolysis).

By utilizing the potential temperature, and the thermodynamic equation, a mathematical description of how a front can undergo frontogenesis (frontolysis) can be given. The potential temperature is defined as the temperature of a parcel of air if that has been compressed or expanded adiabatically to a reference pressure ($p_0 = 1000$ hPa) and it is given by:

$$\theta = T \left(\frac{p_0}{p} \right)^{\frac{R}{c_p}} \tag{1}$$

where T is the temperature (K), p_0 is the reference pressure (1000 hPa), p is the pressure height of the air parcel, R is the gas constant, and c_p is the heat capacity of constant pressure (Wallace and Hobbs, 2006). The thermodynamic equation describes how the internal energy of a system can undergo change mathematically, and is given by:

$$q = c_p \frac{dT}{dt} - \alpha \frac{dp}{dt} \tag{2}$$

where q is the specific heating rate, p is pressure, and α is the inverse of the density, ρ (Wallace and Hobbs, 2006). Following Markowski and Richardson (2010), equation 1 can be rewritten as:

$$\ln T = \ln \theta - \frac{R}{c_p}(\ln p_0 - \ln p) \tag{3}$$

Multiplying the result (equation 3) with $\frac{d}{dt}$, gives:

$$\frac{d \ln T}{dt} = \frac{d \ln \theta}{dt} + \frac{R}{c_p} \frac{d \ln p}{dt} \implies \frac{dT}{dtT} = \frac{d\theta}{\theta dt} + \frac{R}{c_p} \frac{dp}{dtp} \tag{4}$$

If the end result of equation 4 is put into equation 2, then the thermodynamic equation can be written as:

$$\frac{d \ln \theta}{dt} = \frac{d\theta}{dt\theta} = \frac{q}{c_p T} \tag{5}$$

11

By differentiating equation 5 with respect to y $(\frac{\delta}{\delta y})$, the equation can be utilized to describe how a front can undergo frontogenesis (frontolysis) mathematically . The change of the meridional potential temperature gradient following the motion $(-\frac{\delta\theta}{\delta y})$ has been set as the measure of front strength, since the potential temperature gradient is proportional to density gradients. The x-axis is directed along the front, while the y-axis points towards colder air. The frontogenesis equation is given by,

$$\frac{d}{dt}(-\frac{\delta\theta}{\delta y}) = \underbrace{\frac{\delta u}{\delta y}\frac{\delta\theta}{\delta x}}_{\text{Horizontal shear}} + \underbrace{\frac{\delta v}{\delta y}\frac{\delta\theta}{\delta y}}_{\text{Confluence}} + \underbrace{\frac{\delta w}{\delta y}\frac{\delta\theta}{\delta z}}_{\text{Tilting}} - \underbrace{\frac{\delta}{\delta y}(\frac{q\theta}{c_p T})}_{\text{Diabatic heating}} \tag{6}$$

According to equation 6, front strength can change in the following ways: by horizontal shear, confluence, tilting, and diabatic heating, respectively (Markowski and Richardson, 2010).
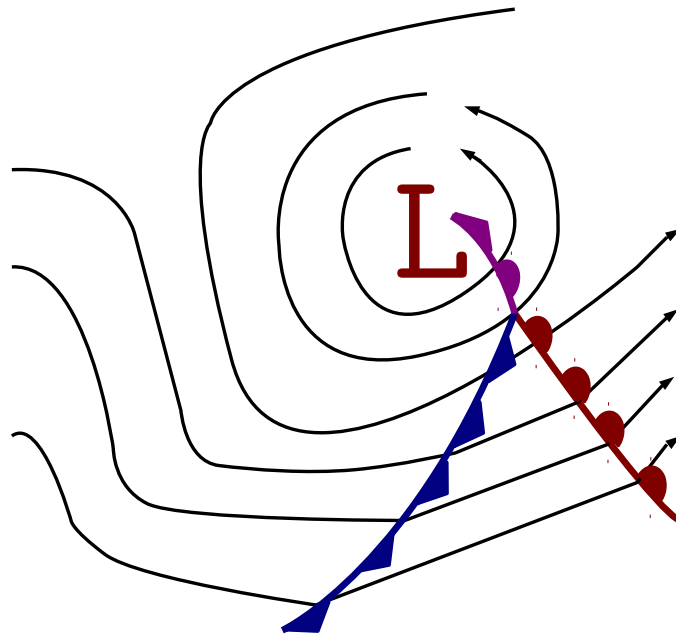
Figure 8: Schematic of a mature extratropical cyclone with a cold front (blue line), a warm front (red line) and an occluded front (purple). The 'L' designates the center of the extratropical cyclone, and the arrows are air trajectories. The triangles and half circles designate the fronts direction of movement. Figure made with inspiration from the National Weather Service[8].

---

[8]http://www.srh.weather.gov/srh/jetstream/synoptic/cyclone.html

Following Markowski and Richardson (2010) the most common fronts are cold fronts, warm fronts, stationary fronts and occluded fronts. A cold front is a front where the cold air mass advances relative to the warm air mass. These fronts usually move equatorward or eastward. A warm front is a front where the warm air mass advances relative to the cold air mass; these fronts usually have a poleward or eastward component. Fronts that show little or no movement are stationary fronts. If a cold or warm front stops moving, it becomes a stationary front. Finally, there are occluded fronts. These fronts can form when an extratropical cyclone reaches its mature stage. Since the cold front moves more rapidly than the warm front, it will eventually overtake the warm front. When this occurs, the surface boundary between the warm front and the cold front is called an occluded front.

Equivalent potential temperature is often used as a measure to show the approximate position of the front. Equivalent potential temperature is defined as the potential temperature an air parcel would attain if all its water vapor were to condense in an adiabatic, isobaric process and is most accurately given by,

$$\theta_e = T \left(\frac{p_0}{p_d}\right)^{\frac{R_d}{c_{pd}+r_t c}} H^{\frac{-r_v R_v}{c_{pd}+r_t c}} exp\left[\frac{l_v r_v}{(c_{pd}+r_t c)T}\right] \tag{7}$$

where T is the temperature (K), p_0 is the reference pressure, p_d is the partial pressure of dry air, R_d is the gas constant for dry air, c_{pd} is the heat capacity at constant pressure of dry air, r_t is the total water mixing ratio, c is the heat capacity of liquid water, H is the relative humidity, r_v is the vapor mixing ratio, R_v is the gas constant for water vapor, l_v is the latent heat of vaporization. For our calculations utilizing equation 7 we have neglected $r_t c$, as this makes a simpler equation without decreasing its accuracy substantially (American Meteorological Society, 2016; Davies-Jones, 2009). It is because the equivalent potential temperature takes water vapor into consideration that it can be used to indicate the location of a front, since cold air is not able to hold moisture, while warm air is able to hold moisture.

Relative humidity, H (%), in equation 7 is given by the ratio between vapor pressure, e_v, and saturation vapor pressure, e_{sv}, times one hundred:

$$H = \frac{e_v}{e_s} \times 100 \tag{8}$$

The relative humidity measures the percentage of water vapor present, compared to the water vapor needed for saturation (Taylor, 1954).

Extratropical cyclones rotate cyclonically, which is defined as counter-clockwise rotation on the northern hemisphere and clockwise rotation on the southern hemisphere. The rotation of the extratropical cyclone is caused by the Coriolis effect. The Coriolis effect deflects the winds to the right side of the actual movement of the wind in the northern hemisphere and left side in the southern hemisphere. The Coriolis effect is an apparent force on moving particles relative to Earth's surface and exists due to the Earth's rotation. This apparent force is given by:

$$-2\vec{\Omega} \times \vec{U}, \tag{9}$$

where Ω is the angular velocity of the Earth and $\vec{U}$ is the (relative) velocity of the particle. The Coriolis effect is often approximated as:

$$f\vec{k} \times \vec{u}, \tag{10}$$

where $\vec{k}$ is the vertical unit vector, $\vec{u}$ is the horizontal velocity, and f is the Coriolis parameter, $f = 2\Omega \sin(\phi)$, where Ω is the angular velocity of Earth, and ϕ is latitude (Holton and Hakim, 2012)

When an extratropical cyclone intensifies, the intensification refers to the strengthening of relative vorticity of the cyclone (i.e stronger cyclonic circulation)(Holton, 1992). Sometimes a cyclone can undergo rapid intensification; this is known as explosive cyclogenesis. A cyclone undergoes explosive cyclogenesis if the sea level pressure in the center of the cyclone decreases at least 1 hPa/hr for 24 hours. Sanders and Gyakum (1980) defined an equation that can be utilized to check if an extratropical cyclone can be classified as undergoing explosive cyclogenesis. This equation is given by:

$$x = \Delta SLP * \frac{\frac{sin(60)}{sin(\phi)}}{24} \tag{11}$$

where x is the maximum deepening rate during the cyclones life cycle (in Bergerons), Δ SLP is the maximum change in SLP (hPa) during the cyclones life cycle over 24 hours, and

ϕ is the latitude of the cyclone. Sanders and Gyakum (1980) defined 24 hPa decrease of pressure in 24 hours over the respective latitude the cyclone moves during this time, as 1 Bergeron. If the calculated value during the rapid intensification of the cyclone in question is above this threshold of 1 Bergeron, then the cyclone undergoes explosive cyclogenesis and can be labeled as a 'bomb'.

2.2 Existence of extratropical cyclones

Because Earth is a sphere and has an angle of $\sim$23.4 degrees between the equatorial plane and the orbital plane, the amount of incoming radiation varies with latitude and time of year. This creates a radiative imbalance that maintains temperature differences between the poles and equator on Earth (Hartmann, 1994). Extratropical cyclones continuously tries to mitigate the temperature differences. However, as long as the radiative imbalance is present, extratropical cyclones will never be able to erase the temperature gradient and they will keep forming on a regular basis within the midlatitudes ($\sim 30° - 60°$), the region where the temperature gradient ∇T is largest on average (see figure 1a).

As mentioned in the introduction (section 1), the temperature gradient gives rise to vertical wind shear and a jet stream at the dynamic tropopause. The relation between the temperature gradient and the vertical wind shear is defined as the thermal wind relation. Before presenting the thermal wind relation, the geostrophic wind must be explained. Following Holton and Hakim (2012), the geostrophic wind is a theoretical wind that results from an exact balance between the Coriolis force (see equation 9 and 10) and the pressure gradient force, $\frac{1}{\rho}\nabla P$,

$$\vec{V_g} = \vec{k} \times \frac{1}{\rho f}\nabla P \qquad (12)$$

The thermal wind relation is defined as the change of the geostrophic wind vector (equation 12) with respect to the natural logarithm of pressure, $\frac{\delta \vec{V_g}}{\delta \ln p}$, and it is proportional to the temperature gradient on a constant pressure surface, $\nabla_p T$:

$$\frac{\delta \vec{V_g}}{\delta \ln p} = -\frac{R}{f}\vec{k} \times \nabla_p T, \qquad (13)$$

where $\vec{k}$ is the vertical unit vector, R is the gas constant, and f is the Coriolis parameter (Holton and Hakim, 2012).

Following Holton and Hakim (2012), when the atmosphere has a temperature gradient

15

and thus thermal wind (see equation 13), it is defined as a baroclinic atmosphere. In a baroclinic atmosphere the density, ρ, depends on both temperature and pressure, $\rho(T, p)$. In the baroclinic atmosphere, the isotherm surfaces (surface of constant temperature) and isobar surfaces (surfaces of constant pressure) are not aligned, and the temperature gradient on constant pressure surfaces is not zero, $\nabla_p T \neq 0$. Under these conditions the distribution of potential energy is uneven and there can be growth of a disturbance. This is known as baroclinic instability. Baroclinic instability is a viable mechanism which can make potential energy of the atmosphere, available for conversion into eddy kinetic energy. The potential energy is made available because warm air has a lower density compared to cold air. The lower density of warm air relative to cold air can be explained via the ideal gas law given by:

$$P = \rho R T \Rightarrow \rho = \frac{P}{RT} \tag{14}$$

where P is the pressure (Pa), ρ is the density (kg/m^3), R is the gas constant and T is the temperature (K) (Markowski and Richardson, 2010). There are more complexities in relation to the density due to the presence of moisture in warm air, however equation 14 is sufficient to prove our point. With equation 14, it can be seen that an increase of T, will decrease ρ, hence warm air will have a lower density compared to cold air. Because warm air has a lower density than cold air the pressure surfaces tilt downwards towards higher latitudes. So an air parcel at the equator will be higher above the surface compared to an air parcel at higher latitudes. Thus, there will be a difference in potential energy between the parcels. If an air parcel from equator displaces an air parcel from high latitudes, the lighter air parcel is surrounded by heavier air parcels and vice versa. This will lower the center of mass, and convert potential energy into kinetic energy. This available energy is known as available potential energy (APE), and can be converted into eddy kinetic energy (Holton and Hakim, 2012). It is because of this available potential energy that extratropical cyclones form within the baroclinic atmosphere that is located in the midlatitudes (see figure 1). APE can be made available for extratropical cyclones, diabatically through high sea surface temperatures, precipitation via latent heat release and radiation. Following Papritz and Spengler (2015), high sea surface temperature can deform the isentropes, creating a steeper isentropic slope and a stronger horizontal temperature gradient, causing enhanced ascent and enhanced APE (see figure 2a in Papritz and Spengler (2015)). While midtropospheric heating, caused by latent heat release or absorption of radiation by the air also deforms the isentropes, making them steeper, thus increasing APE (see figure 2b in Papritz and Spengler (2015)). Adiabatically, APE can be made available via a horizontal

temperature gradient and the jet stream (Holton and Hakim, 2012).

To summarize, a jet stream is linked to a temperature gradient, which is again linked to baroclinicity via the thermal wind relation. Baroclincity is linked to available potential energy that can be converted to eddy kinetic energy for the extratropical cyclones via the horizontal temperature gradient (Holton and Hakim, 2012)

Following Holton and Hakim (2012), when an atmosphere is not baroclinic it is defined as a barotropic atmosphere. A barotropic atmosphere is an atmosphere where the density, ρ, depends on pressure only, $\rho(p)$. In the barotropic atmosphere the isopycnic surfaces (lines of constant density), are aligned with the isobars (lines of constant pressure). If the gas is ideal, the isotherms (lines of constant temperature) will also be aligned with the isobars, which means that the temperature gradient on isobars is equal to zero, $\nabla_p T = 0$. A purely barotropic atmosphere does not contain fronts and baroclinically generated extratropical cyclones, because there is no APE for extratropical cyclones to grow. In some cases the atmosphere is equivalent barotropic. If the atmosphere is equivalent barotropic, the isothermal surfaces and the geopotential height surfaces on isobaric surfaces are parallel. In a equivalent barotropic atmosphere the wind direction does not change with height, thus this atmosphere can have a temperature gradient (Sun, 2005). If the atmosphere is equivalent barotropic, there can be no temperature advection, which is required for an extratropical cyclone to grow (Moore, R. W., Private Communication, 2016).

A useful meteorological tool to check if an atmosphere is equivalent barotropic is the geopotential. Following Holton and Hakim (2012), the geopotential is the potential energy of a unit mass relative to the sea level. It is the amount of work needed to lift this unit mass from the sea level up to the height which it is located. Geopotential height, is the height of which this unit mass is located and is given by:

$$Z_T = Z_2 - Z_1 = \frac{R}{g_0} \int_{p_1}^{p_2} T \, d\ln p, \tag{15}$$

where Z_T is the thickness of the atmospheric layer, between two pressure surfaces p_2 and p_1, T is the temperature (K), g_0 is the gravitational constant, p is the pressure (Pa), and R is the gas constant (Holton and Hakim, 2012). If the geopotential contours or the isobaric contours at different heights align, it implies that the atmosphere is equivalent barotropic, which means that an extratropical cyclone cannot grow (Moore, R. W., Private Communication, 2016).

2.3   Tangent linear model and adjoint model

An adjoint model (AM) gives information about sensitivity of a forecast aspect at a final time and location of interest, relative to an initial nonlinear field and time of interest. The AM can provide good estimates of a final nonlinear forecast fields sensitivity to the actual dynamics of an initial nonlinear forecast field (Errico, 1997). To explain what an AM is, a basic description of a nonlinear model (Kalnay, 2003) and a tangent linear model (TLM) (Kalnay, 2003; Errico, 1997) must be introduced.

A NLM computes the evolution of an atmospheric field in space and time. The NLM consists of equations, for instance the equations of motion (Holton and Hakim, 2012), which has to be discretized in space and time. When the model equations are discretized in space, using a space discretization method (finite differences or spectral expansion (Kalnay, 2003)), they become a set of n nonlinear coupled differential equations,

$$\frac{d\vec{x}}{dt} = \vec{F}(x) \qquad \vec{x} = \begin{bmatrix} x_1 \\ x_2 \\ \vdots \\ x_n \end{bmatrix} \qquad \vec{F} = \begin{bmatrix} F_1 \\ F_2 \\ \vdots \\ F_n \end{bmatrix} \tag{16}$$

To compute the evolution of the NLM equations with time, these equations must also be discretized in time. Following Kalnay (2003), the time discretization can be done by applying a time difference scheme. Once the NLM equations have been discretized in both space and time, the model can compute the evolution of the NLM equations with time. By giving the NLM, M, a field of variables, x_0, at t_0, the model will evolve this field of variables with time and give an output value, x_f, at t_f.

$$\vec{x}(t_0) = M(\vec{x}(t_f)) \tag{17}$$

The concept of a TLM was introduced by Lorenz (1965). A TLM is a tangent linear version of a NLM. If a perturbation, $y(t_0)$, is added to equation 17, it becomes:

$$M[\vec{x}(t_0) + \vec{y}(t_0)] = M[\vec{x}(t_0)] + \frac{\delta M}{\delta \vec{x}}\vec{y}(t_0) + O[\vec{y}(t_0)^2] = \vec{x}(t) + \vec{y}(t) + O[\vec{y}(t_0)^2] \tag{18}$$

Taking the perturbation, y, and differentiating this with time leads to:

$$\frac{d\vec{y}}{dt} = J\vec{y} \quad \text{with} \quad J = \frac{\delta \vec{F}}{\delta x} \tag{19}$$

where the J is the Jacobian of F in equation 16. Equation 19 is the linear differential form of the NLM equations and the solution is:

$$\vec{y}(t_0) = L\vec{y}(t_f), \quad \text{where the tangent linear operator} \quad L = \frac{\delta M}{\delta x} \tag{20}$$

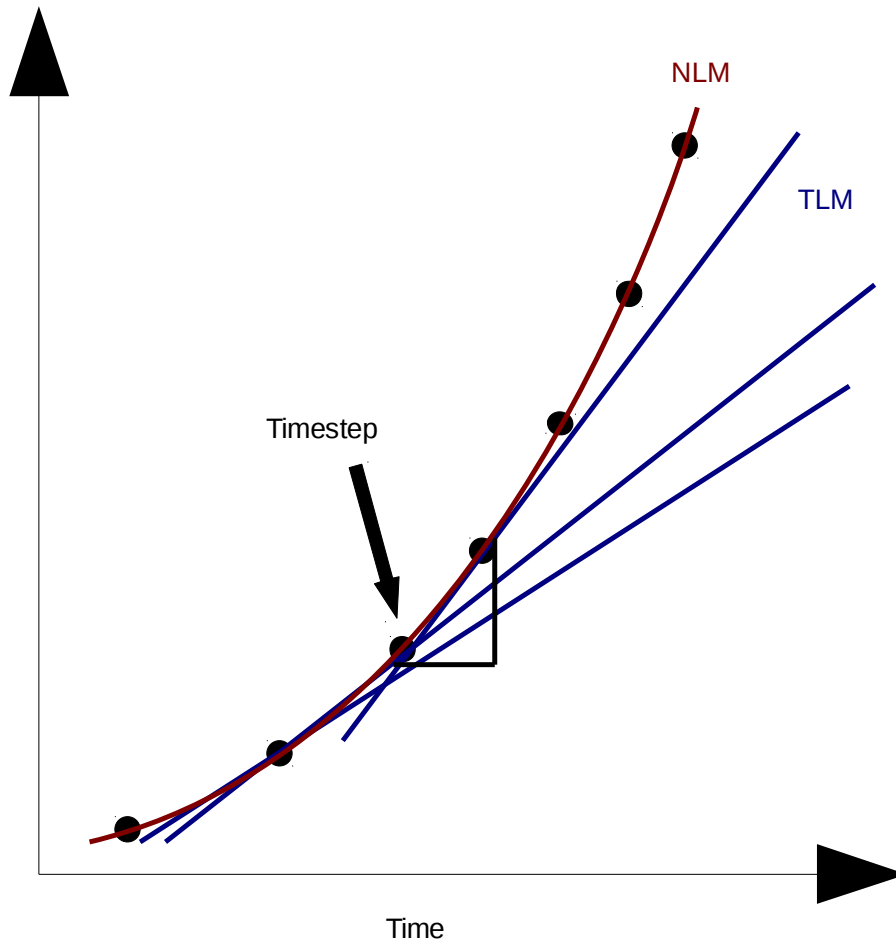The TLM maps a perturbation vector $(\vec{y})$ from timestep t_0 to t_f.

Figure 9: Schematic explaning difference between a TLM (blue trajectory, TLM) and a NLM (red trajectory, NLM). The black dots designate the timesteps which the TLM is saved and utilized by the TLM.

To describe the difference between a NLM and a TLM more clearly, a graph has been made (see figure 9). The NLM is updated and saved at each timestep, where the time intervals are specified by the user, then the TLM trajectory is updated accordingly by the NLM trajectory (i.e TLM is not a purely linear approximation). By saving the NLM fields at many timesteps the TLM trajectory can be stopped from diverging from the NLM trajectory. The shorter the timesteps, the more accurate the TLM trajectory will be in relation to the NLM. Since the TLM utilizes the tangent linear version of the nonlinear equations, it means that the accuracy of the TLM will be reduced for a more nonlinear atmosphere, model physics or a longer model run. As long as the length of the TLM model run is constrained and the NLM field is updated and saved at a frequent enough interval, the output of the TLM will be useful because it will constrain the TLM from diverging too far from the NLM. To obtain an AM the tangent linear operator, L, is transposed and the forecast response function, J, is differentiated with respect to the perturbation vector, $\vec{y}$ from t_f to t_0:

$$\frac{\delta J}{\delta \vec{y}(t_0)} = L^T \frac{\delta J}{\delta \vec{y}(t_f)} \tag{21}$$

where, L^T, is the transpose of the tangent linear operator, L. The AM maps a sensitivity gradient backwards in time from t_f to t_0 (Kalnay, 2003).

2.3.1   Adjoint model interpretation and related terminology

Before obtaining the AM sensitivity fields an input field of some parameter, $\vec{a}$, must be given to the model so that it gives an output field of some parameter, $\vec{b}$. The AM is used to obtain the initial field sensitivity with respect to a forecast aspect, $J_n(\vec{b})$, at a final time, where n are specific measures. A forecast aspect, can be any meteorological field variable of interest, for example precipitation, kinetic energy (KE) etc. The function that calculates $J_n(\vec{b})$ is defined as the forecast response function or cost function, J_n. An AM can be utilized to achieve an indication of the smallest changes to the initial fields, $\vec{a}$, that result in the largest change in the final forecast aspect, $J_n(\vec{b})$. The sensitivities are presented by first obtaining a control forecast where the input is $\vec{a}_c$ and the output $\vec{b}_c$. Then the chosen field parameter is perturbed and the input $\vec{a}_p$ and the output $\vec{b}_p$ can be obtained. The calculated forecast aspect $\Delta J_n = J_{np} - J_{nc}$, will now represent the sensitivity. To be able to address all possible variables with respect to a control nonlinear forecast, a_c, one selected J that is first-order differentiable with respect to b is considered, and then the J

and the gradient of J with respect to b $\left(\frac{\delta J}{\delta b}\right)$ for the control solution, b_c, is calculated. The gradient of J with respect to b, can then be interpreted as the sensitivity of J with respect to small perturbations in the output field b. The equation can be written as:

$$J = \sum_k \frac{\delta J}{\delta b_k} \Delta b_k, \tag{22}$$

where J is the forecast response function, the subscript k, is a component in the output field, $\vec{b}$. $\vec{b}$, can for example be the zonal wind, u, at a specific time and location. Δb_k, is the difference between the perturbed field output value, b_p, and the control field output value, b_c. Given a change to the initial state, Δb_k, in the area of maximum sensitivity, one can expect a large change of $\frac{\delta J}{\delta b_k}$, and thus the forecast aspect J, at the final forecast time. This is the initial nonlinear field sensitivity with respect to the final nonlinear field. A much more interesting sensitivity would be the final nonlinear field sensitivity with respect to the initial field, a, i.e the gradient of J with respect to $\vec{a}$, $\frac{\delta J}{\delta a}$.

$$J = \sum_k \frac{\delta J}{\delta a_k} \Delta a_k, \tag{23}$$

Equation 22 can be interpreted in the same way as equation 23, if $\frac{\delta J}{\delta b_k}$ is large for a given Δa_k of some magnitude, then J is sensitive with respect to the given perturbation. Since b is calculated from a, the sensitivity gradient of J with respect to a can be interepreted in the same way as the gradient of J with respect to b. Instead of being the sensitivity with respect to the output field like $\frac{\delta J}{\delta b}$, $\frac{\delta J}{\delta a}$ is the sensitivity with respect to the initial field, and this gradient can be determined by running the AM (Errico, 1997).

Once the response function J is chosen, a specific area of interest must also be chosen at the final time of the nonlinear model run; this area is three dimensional and is known as the response function box. This box specifies where the response of adjustments made in the nonlinear field within the adjoint sensitivity fields can be seen. If a field of positive and negative sensitivities is calculated with the AM, and changes are made within the corresponding sensitive areas at the initial time of a nonlinear forecast, and then this new nonlinear field is evolved in the NLM, a change in the three dimensional response function box at the final time should be seen. If the response function, J, is chosen to be maximized in the response function box, then all perturbations made within the positive and negative sensitivities at the initial nonliear field will increase the respective J within the response function box at the final nonlinear field. However, it is not uncommon if the perturbations

are large, that a change in the final nonlinear field outside the response function box occurs. If the change of the adjustments made in the initial nonlinear field were to grow within the response function box only at the final nonlinear field, in most cases, that would be unphysical, since an atmospheric field variable is complex and continuous.

Sometimes a certain change within the response function box is desired. For example if the J is chosen to be precipitation, then it would be interesting to see which changes in the nonlinear model field, must be done to maximize or minimize the precipitation within the response function box at the final time. The perturbations that give the desired change of J within the response function box is known as the optimal perturbations, and the derivation is outlined below.

2.3.2   Adjoint optimal perturbations

The optimal perturbations are the perturbations that optimize the change of the forecast aspect, J, at the final time. The optimal perturbations are computed from the sensitivity field and scaled to be of similar size as analysis errors (~ 1), which also implies that the largest perturbations are of size ~ 1. Following Doyle *et al.* (2013), the adjoint optimal perturbations are calculated as follows: As explained in the previous section, the forecast aspect perturbations, J' is equal to:

$$J' = \sum_j \frac{\delta J}{\delta x_j} x'_j, \tag{24}$$

where $\frac{\delta J}{\delta x_j}$ is the adjoint gradient of the response function with respect to the initial condition jth component of x. All x are taken at the initial time, t_0, unless stated otherwise. The jth component of the perturbation vector $\vec{x}$', is optimal when:

$$x'_j = \frac{s}{w_j} \frac{\delta J}{\delta x_j} \tag{25}$$

Equation 25, can be solved if the squared value of the jth component of x' is constrained with a weight, w_j, thus:

$$I = \sum_j w_j x'^2_j \tag{26}$$

The scaling parameter, s, in equation 25, can be found by inserting equation 25 into 26. This gives:

$$s = \frac{\sqrt{2I}}{\sum\limits_{j} \frac{1}{w_j} \left(\frac{\delta J}{\delta x_j}\right)^2},$$

(27)

where w_j is equal to one over the absolute difference between the maximum x at the final time, t_f, and initial time, t_0, at the vertical level k and the variable m,

$$w_j = \frac{1}{[max(|x_{t_f}^{m,k} - x_{t_0}^{m,k}|)]^2}$$

(28)

If the largest difference on a vertical level k, of x at the initial and final time of a forecast is 4 m/s, the $w = \frac{1}{16}$ m^2/s^2, and is multiplied with all x at this level. The calculation of w will also give the scaling parameter, s, which makes it possible to compute the optimal perturbations, x_j'.

2.3.3 Use of an adjoint model

As indicated earlier, the AM can be used to achieve an indication of the final time forecast aspect sensitivity to different parameters in the nonlinear field at the initial time. The AM indicates the size, structure and location of the sensitivities to the forecast aspect, of which can be tied to the actual dynamics of the nonlinear forecast model. From the AM output, the optimal perturbations can be calculated (see section 2.3.2). Ideally, depending on what is defined as the forecast metric within the response function box, the initial atmospheric fields of the forecast can be perturbed based on the sensitivity, so that a desired change at the final time within the forecast response function box is obtained.

For instance, consider KE as the response function, J. If the AM calculates the initial nonlinear field sensitivities with respect to the KE at the final nonlinear field, and the sensitivities are large ($\sim \pm 1$ [m^2/s^2]/gkg^{-1}) it means that the respective change within the KE response function box will also be large if a forecast was run with changes made within the sensitive regions at the initial nonlinear field (Errico, 1997).

3 Method

3.1 Synoptic analysis Method and data

3.1.1 Diabatic PV and Tropopause folding

Research has provided several meteorological concepts useful for research of extratropical cyclones and other atmospheric features (Holton and Hakim, 2012; Markowski and Richardson, 2010; Wallace and Hobbs, 2006); one such meteorological concept is potential vorticity (PV). PV is one of the most important concepts in Dynamic Meteorology (Holton and Hakim, 2012). PV combines mass, momentum and energy conservation laws into one equation, and is useful when analysing cyclogenesis and the development of an extratropical cyclone. Before introducing the PV equation, the concept of absolute vorticity, ω_a, must be explained. Following Holton and Hakim (2012), the absolute vorticity measures the rotation of a fluid on a microscopic scale and includes the rotation of the Earth. The absolute vorticity is defined as the curl of the absolute velocity and is given by:

$$\vec{\omega}_a = \nabla \times \vec{U}_a = \vec{\omega}_r + \vec{\omega}_e = \nabla \times \vec{U}_r + \nabla \times \vec{U}_e \tag{29}$$

The absolute vorticity is the sum of the relative vorticity, $\vec{\omega}_r$ (vorticity of cyclones) plus the vorticity of earth, $\vec{\omega}_e$. The absolute vorticity is one of the fundamental components of the PV equation.

Following Holton and Hakim (2012), the PV equation is known as Ertel Potential Vorticity theorem and is given by:

$$\frac{D}{Dt}\left[\frac{\vec{\omega}_a \cdot \nabla\theta}{\rho}\right] = 0 \tag{30}$$

where $\nabla\theta$, is the gradient of potential temperature, ρ is the density and ω_a is the absolute vorticity. Ertels Potential Vorticity theorem (equation 30) says that when following the motion in time, the relation between the absolute vorticity, ω_a, gradient of potential temperature, $\nabla\theta$, and density, ρ, must be constant and equal to zero. Equation 30 only applies when the flow is adiabatic and frictionless. Intuitively it means that if one of the components in the equation 30 undergoes an increase (decrease) another component must decrease (increase). So for example if the gradient of θ decreases, the vorticity component, $\vec{\omega}_a$, must increase.

Following Stoelinga (1996), PV can be produced by diabatic processes or friction. With respect to extratropical cyclones the diabatic PV contribution comes from condensation. Condensation refers to the physical process when water vapor becomes a liquid or solid and is the opposite of evaporation (Burrows *et al.*, 1990). Following Wallace and Hobbs (2006), when water vapor condenses or liquid water evaporates, enthalpy is released. This release of enthalpy is referred to as latent heat. When water vapor condenses, the air–vapor–liquid system reduces the rate of temperature reduction via latent heat release (it warms the ambient air). When the air evaporates liquid water, the opposite happens and the ambient air is cooled.
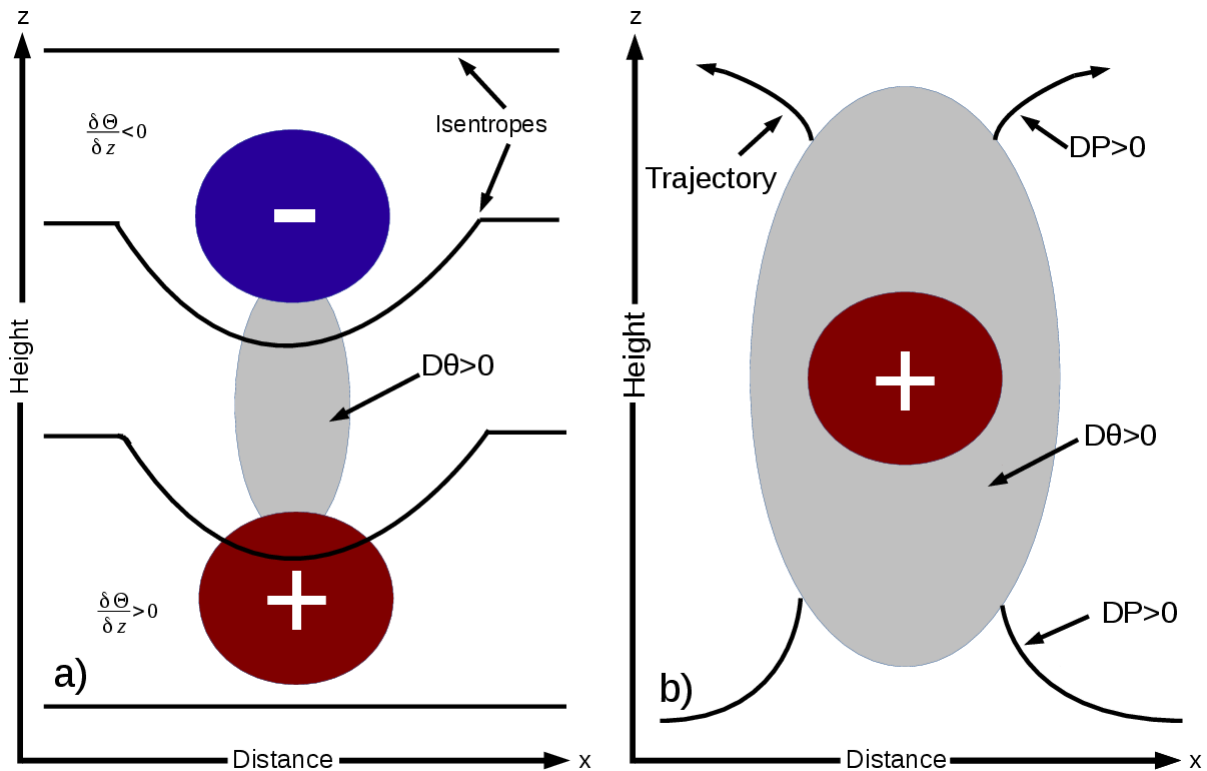
Figure 10: Schematic vertical cross-sections showing diabatic PV is produced (red: positive PV anomaly, blue: negative PV anomaly), for the idealized cases of (a) 'impulsive diabatic heating', and (b) 'steady condensation' in a frontal zone. Shading indicates the region of diabatic heating (DH). In (a) the solid lines are isentropes and in (b) the bold lines with arrows refer to air-parcel trajectories. Dθ and DP denote material tendencies of potential temperature and potential vorticity, respectively. Caption and figure made with inspiration from Wernli and Davies (1997).

Extratropical cyclones are associated with vertical movement of air (Wallace and Hobbs, 2006). When moist air at the surface is lifted vertically by the cyclone, this moist air will eventually cool until saturation and undergo condensation (Markowski and Richardson, 2010). If the vertically ascending air has high moisture content, the latent heat caused by condensation of this moisture can have a great impact on the evolution of the cyclone, through the creation of the positive and negative PV anomalies (Wernli and Davies, 1997; Raymond and Jiang, 1990; Snyder and Lindzen, 1991). The positive PV anomaly is associated with cyclonic rotation and can increase the cyclonic circulation of the cyclone, while the negative PV anomaly is associated with anti-cyclonic rotation and could have the effect of decreasing the cyclonic circulation of the cyclone (Holton and Hakim, 2012).

Following Wernli and Davies (1997), it can be explained how the impact of latent heating occurs. From a eulerian perspective, the midtropospheric latent heat release from condensation of moist air, bends the isentropes downwards above and below the region of maximum diabatic heating (see figure 10a). The PV equation (equation 30) can be rewritten to help understand why the latent heat release changes the PV. If equation 29 is put into equation 30, then the PV can be written as:

$$PV = \frac{\vec{\omega}_a \cdot \nabla\theta}{\rho} = \frac{(\vec{\omega}_r + \vec{\omega}_e) \cdot \nabla\theta}{\rho} = \frac{(\nabla \times \vec{U}_r + \nabla \times \vec{U}_e) \cdot \nabla\theta}{\rho} \tag{31}$$

If the vertical component of equation 31 is taken, and the Coriolis parameter (see equation 10 in section 2.1), f, is utilized, then the vertical component of PV will be approximately equal to:

$$\frac{(\vec{k} \cdot \nabla \times \vec{U}_r + \vec{k} \cdot \nabla \times \vec{U}_e)\vec{k} \cdot \nabla\theta}{\rho} \approx \frac{\zeta + f}{\rho}\frac{\delta\theta}{\delta z} \approx PV \tag{32}$$

where $\vec{k} \cdot \nabla \times \vec{U}_e$ was approximated as the Coriolis parameter f, ζ, is the vertical relative vorticity, ρ is the density, and $\frac{\delta\theta}{\delta z}$, is the vertical component of $\nabla\theta$. By utilizing equation 32, it can see that above the region of maximum heating the distance between the isentropes increase (i.e $\frac{\delta\theta}{\delta z} < 0$), which causes a decrease of PV and a negative PV anomaly. The opposite occurs below the region of maximum heating, the distance between the isentropes decreases (i.e $\frac{\delta\theta}{\delta z} > 0$), and the PV anomaly becomes positive. This stationary heating makes a dipole of PV (see figure 10a).

If the same concept is explained via a lagrangian perspective, the vertical advection of saturated air parcels moving through the region of maximum diabatic heating generates a positive PV anomaly (see figure 10b). The successive passage of saturated air through the region of maximum diabatic heating, leads to in situ generation of PV. When the conden-

sation is steady, the timescale of vertical advection of saturated air parcels is equal to that of latent heating, and a positive PV anomaly is generated (Wernli and Davies, 1997).

Another atmospheric feature that can have a great impact on the evolution of an extratropical cyclone is the dynamic tropopause. The tropopause is the boundary between the troposphere and the stratosphere (Taylor, 1954). Above the tropopause the air is statically stable and there is large positive PV because of its dependence on the $\nabla\theta$ in Ertel's potential vorticity theorem (see equation 30). Sometimes the tropopause folds into the lower atmosphere (see figure 11) and can form a surface cyclone or increase the strength of an already existing surface cyclone through the far field rotational effect associated with a moving tropopause fold and its positive PV (Holton and Hakim, 2012).
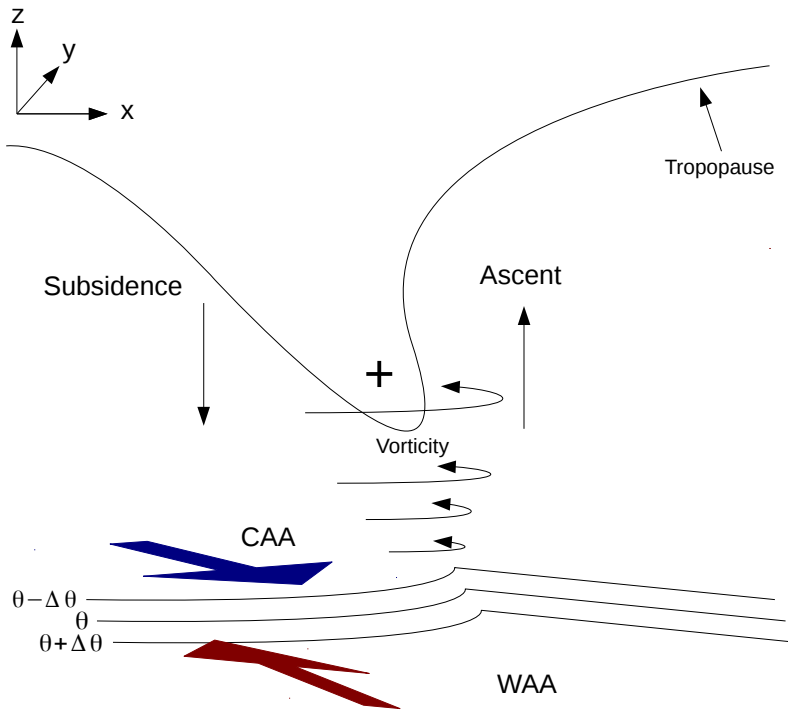
Figure 11: Schematic of a tropopause fold. Vertical black arrows designate the approximate region of ascent and subsidence. The '+' sign designates large positive PV above the tropopause. The effect of the vorticity associated with the positive PV on the surface baroclinic zone is also shown with the horizontal circular shaped arrows. Warm air advection (WAA) and cold air advection (CAA) is designated by the red and blue arrows, respectively. Figure made with inspiration from Holton and Hakim (2012); Plant *et al.* (2003); Gray and Dacre (2006)

The tropopause usually folds on the poleward side of the jet stream associated with the ageostrophic velocity at the entrance and exit regions of a jet stream (Hoskins, 1982). The tropopause typically folds into a frontal zone beneath the jet stream, because of the jet stream's dependence on a ∇T (i.e baroclinicity), via the thermal wind relation (Holton and Hakim, 2012).

When an upper tropopause fold (also known as upper level trough) moves over an already mature surface cyclone a PV-tower may form. A PV-tower is recoginized by a vertical alignment of anomalous positive PV (Wernli *et al.*, 2002). A PV-tower often arises when an extratropical cyclone undergoes explosive cyclogenesis. The upper level positive PV associated with the tropopause fold couples with the low level positive PV associated with the surface cyclone, and mutually amplifies (see Wernli *et al.* (2002) or section 3.1.3 for an example and explanation of how the PV-tower forms).

Voriticity, PV and tropopause folding are important concepts utilized for analysis of extratropical cyclones, to better define their dynamics. These concepts are also utilized when categorizing the cyclones. An extratropical cyclone can undergo cyclogenesis in these four following ways: Type A and B cyclogenesis (Petterssen and Smebye, 1971), Type C cyclogenesis (Deveson *et al.*, 2002) and diabatic rossby vortex (DRV) cyclogenesis (Raymond and Jiang, 1990; Snyder and Lindzen, 1991; Parker and Thorpe, 1995; Moore and Montgomery, 2004). The following section summarizes these four types of cyclogenesis, and explain under which circumstances the extratropical cyclones form.

3.1.2 The cyclogenesis classifications

Petterssen and Smebye (1971) identified two types of evolutions of extratropical cyclones:

Type A

- Cyclone forms in a region of maximum baroclinicity on a front.

- No pre-existing tropopause fold

- A tropopause fold may form as the cyclone evolves, but the distance between the tropopause fold and the cyclone is constant until the cyclone reaches maximum strength.

- Advection of vorticity is small during the cyclones life.

- Thermal advection is strong, and is the main contributor to the deepening of the cyclone

28

Type B

- Cyclone forms due to a tropopause fold that moves over a warm advection region within a baroclinic zone.

- As the cyclone deepens, the structure is vertical, and the distance between the tropopause fold and the cyclone decreases rapidly.

- Advection of vorticity is large at genesis, and decreases as cyclone deepens.

- Thermal advection is weak at first, but increases as cyclone deepens.

In later years, it was discovered that latent heating can have a large impact on the cyclogenesis of a cyclone. Thus, Deveson *et al.* (2002) identified a third way an extratropical cyclone can undergo cyclogenesis:

Type C

- Cyclone forms when a tropopause fold moves over an ocean, and is dominated by this tropopause fold.

- Cyclone forms at higher latitudes

- Cyclone has organized convection which affects evolution of the cyclone

- Cyclone is similar to comma-cloud type polar low pressure system at initial timesteps.

Diabatic Rossby Vortex

Raymond and Jiang (1990) and Snyder and Lindzen (1991) first introduced the concept of a Diabatic Rossby Wave. A Diabatic Rossby Wave is a moist baroclinic wave, that can produce low level diabatic positive PV anomalies due to latent heat release from condensation of vertically lifted moist air (see section 3.1.1 and figure 10, for explanantion of diabatically produced PV). We will follow Moore and Montgomery (2004) and refer to the Diabatic Rossby Wave, as a Diabatic Rossby Vortex (DRV) from now on, due to the vortical structure of this mechanism in 3 dimensions.

From Moore *et al.* (2008), the concept of a growing DRV can be described as; 'An isolated low-level vortex present in the vicinity of a surface frontal zone. Its continued existence is regarded as a synergetic interaction, whereby the vortex contributes to ascent on the frontal slope, which results in condensation and the diabatic production of potential

vorticity (PV). The resulting PV serves to enhance (or replace) the original vortex's PV and concomitantly account at least in part for the vortex's propagation toward or along the frontal zone'. Figure 12, summarizes the DRV concept, from step one to three.
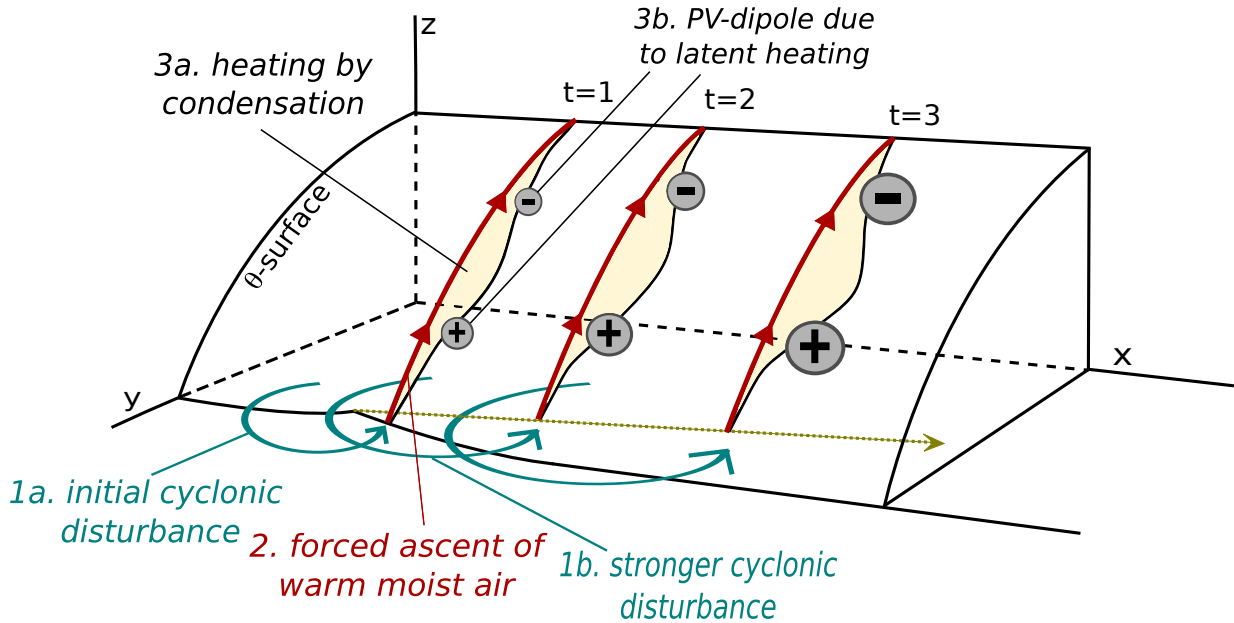

Figure 12: Schematic of the growth mechanism of a Diabatic Rossby Vortex. See text for detailed explanation. Figure taken from Terpstra (2014).

3.1.3   Identification of a Diabatic Rossby Vortex

Boettcher and Wernli (2013) defined critical conditions for formation of a DRV. The critical conditions are as follows; a presence of a strong low level temperature gradient, sufficient moisture in the vicinity where the DRV forms and propagates, and a small influence of friction, since DRV's usually form over the ocean. Boettcher and Wernli (2013) empirically determined synoptic scale environments where the critical conditions are typically fulfilled. These synoptic scale environments are shown on figure 13. One aspect the respective environments have in common is that the DRV's seems to form on the equatorward side of the strongest baroclinic zone, and have an ideally placed sub-tropical high pressure system or low pressure system that continously feeds the baroclinic zone with moist warm air from the subtropics (see figure 13a and b, respectively). The third option is where the initial DRV disturbance is triggered by large scale lifting on the downstream side of the upper level trough. This scenario is similar to the typical "type B" cyclogenesis situation.

However, in contrast to type B cyclogenesis, the DRV does not couple with the upper level disturbance. For this reason, we can exclude it as type B cyclone. Instead of evolving into a mature extratropical cyclone, the DRV propagates quickly downstream into the region of the upper level ridge, with an intense warm front of a pre-existing cyclone (see figure 13c). In the two remaining synoptic scale scenarios, a pre-existing cyclone or a tropical cyclone undergoing extratropical transition, propagates into a strong baroclinic zone and transforms into a DRV (figure 13d and e).

If we want to investigate if an extratropical cyclone might have evolved like a DRV, the first step should be checking the synoptic scale environment. If the synoptic scale environment of the extratropical cyclone in question fits one of the environments presented in figure 13, it could be used as a precursor for further investigation. However, it should be noted that these synoptic scale environments were empirically determined, so if the synoptic scale environment does not fit one of the respective synoptic scale environments in figure 13, it does not imply that the extratropical cyclone under investigation cannot have evolved similar to a DRV.
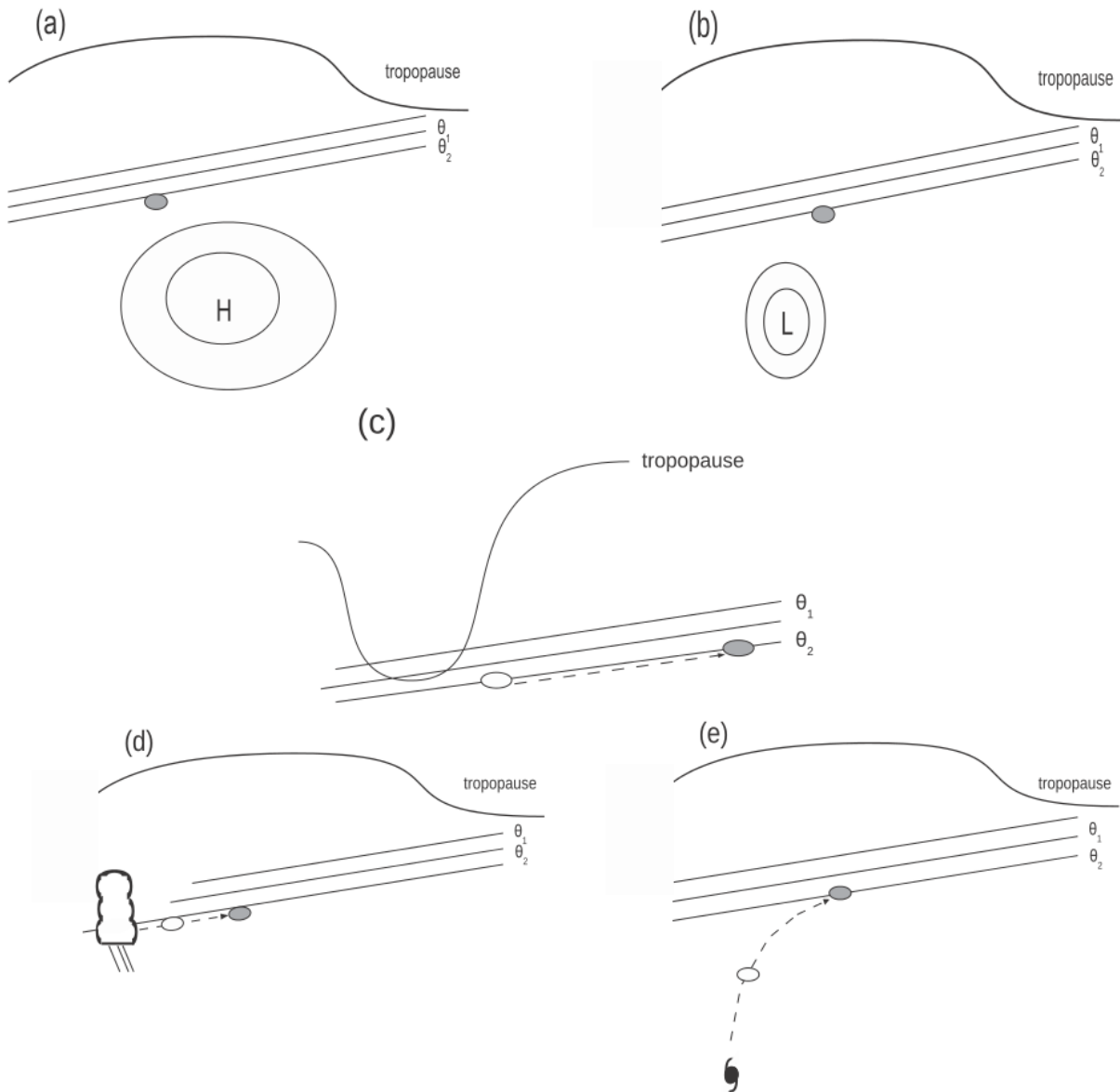
Figure 13: Schematics of typically observed synoptic-scale configurations for DRV genesis. White ellipses denote DRV track starting positions and gray ellipses indicate the start of the DRV propagation phase (a gray ellipse is shown if the two coincide). The scenarios are (a) flow around a subtropical high against the baroclinic zone; (b) flow around a cyclone against the baroclinic zone; (c) surface cyclone formation induced by forcing from upper level trough; and (d) and (e) PV remnants from a mesoscale convective system or tropical cyclone, respectively, moving into the baroclinic zone. Figure and caption taken from Boettcher and Wernli (2013).

If the synoptic scale environment seems to favor DRV formation, a methodology to objectively identify DRV's developed by Boettcher and Wernli (2013), can be utilized. This methodology bases itself on six criteria, and are as follows:

1. Local SLP minimum. Pressure in center 0.5 hPa lower than closest surroundings.

2. There must be a collocated PV anomaly at 850 hPa over the sea level pressure minimum. The average PV at 850 hPa over the grid point and its eight neighbours must be at least 0.8 PVU.

3. High low level baroclinicity. The baroclinicity is measured by taking the difference between the potential temperatures above the 90th percentile and below the 10th percentile in the small grey box on figure 14. If $\delta\theta > 5$ K, the criterion is fulfilled.

4. The propagation speed during the propagation phase must be at least 11.6 m/s. This is checked by measuring the distance the SLP minimum moved in six hours.

5. There must be enough condensational latent heat release. The condensational latent heat release is measured by taking the average of the values above the 10th percentile of relative humidity, H, within the large gray box on figure 14. If the $H_{10th\%}$ is above 90%, the criterion is fulfilled.

6. The upper level forcing must be small. The influence of upper level forcing is checked by taking average PV at 250 hPa (6.1) and the average upper level induced Quasi-Geostrophic (QG) ascent at 700 hPa (6.2), in the large grey box (see figure 14) above the surface cyclone. The PV in this box must be less than 1.0 PVU, and the average upper level induced QG ascent, must be smaller than 0.5 m/s (see Clough *et al.* (1996), for an equation diagnostic that can be applied for quantifying QG ascent).

- **Criterias 1 and 2 must be fulfilled all 6 hour timesteps during the DRV life cycle.**

- **Criterias 3-6 must be fulfilled a minimum of 3 of the 6 hour timesteps during the DRV life cycle.**
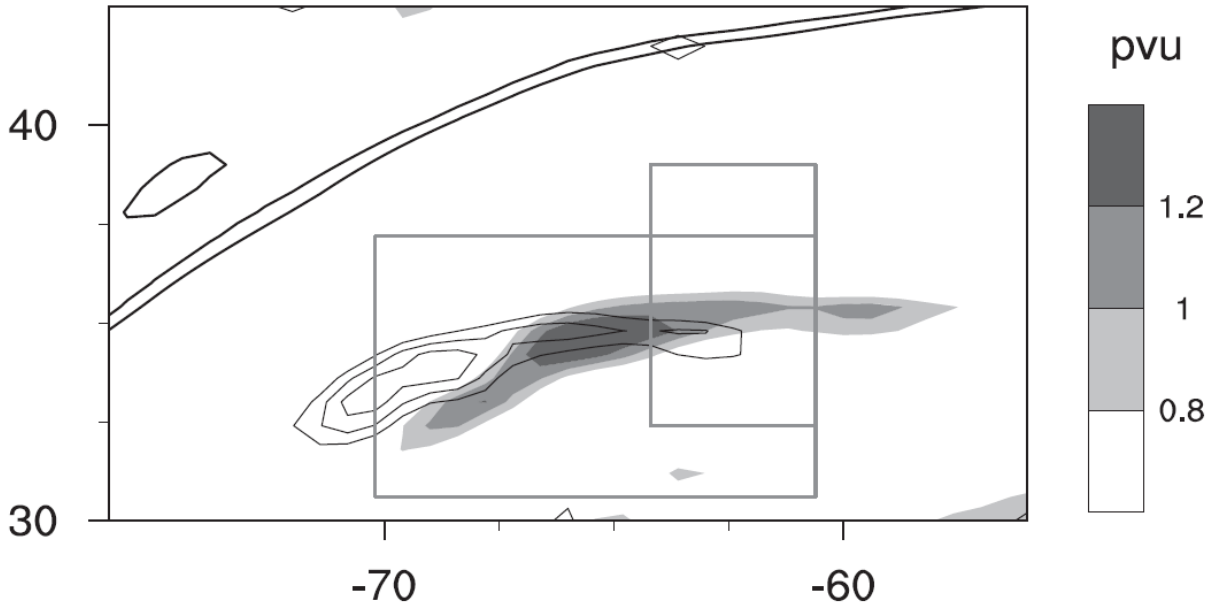
Figure 14: Sketch of a typical DRV, and the placement of the boxes that was used to find the average of relevant variables for a DRV. See text for detailed explanation. Figure taken from Boettcher and Wernli (2013).

If these six criteria are fulfilled, the extratropical cyclone under investigation can be classified as a DRV. We will utilize this method on Nina, but with some modifications. To check if criterion one is fulfilled, we have not utilized the cyclone identification algorithm by Wernli and Schwierz (2006), like Boettcher and Wernli (2013). Since this is a case study, we plotted the SLP minimum for each relevant timestep (18 UTC 7 January 2015 - 12 UTC 9 January 2015) to see if the thresholds of criterion one were fulfilled.

Since criterion six involves two different criterions, we have divided this criterion into two parts. Criterion 6.1 involves the average PV at 250 hPa, and 6.2 involves the QG ascent from upper levels (< 650 hPa) and lower levels (> 850 hPa) forced at 700 hPa. To check if criterion 6.2 is fulfilled, we have not inverted the QG omega equation. We have plotted the potential temperature at the tropopause to get an indication of the contribution of upper level forcing. If the upper level trough at 300 hPa is stationary, or if the upper level trough moves at a significantly different speed as Nina, there should not be upper level forcing of significance forcing Nina (Spengler, T., Private Communication, 2016). If the critical conditions and one of the synoptic scale environments presented by Boettcher and Wernli (2013) fits the synoptic scale environment during Nina, we will check the six criterion to see if we can classify Nina as a DRV.

If an extratropical cyclone can be classified as a DRV, even further investigation can be made. We can, in addition, check if the DRV in question is an explosive DRV. Boettcher and Wernli (2013) made composites that shows what typically leads to the explosive cyclogenesis of the DRV. The first scenario is based on the total number of DRV's undergoing explosive cyclogenesis due to an upper level trough located upstream of the DRV. The second scenario is determined manually by analysis of the explosive DRV cases without an upstream upper level trough.

In the first scenario the upper level trough overtakes the low level DRV, usually in 24 hours (see figure 15). While this occurs, the low level DRV undergoes explosive cyclogenesis and rapidly intensifies. The first couple of hours (figure 15a and b), the upper level tropopause fold begins overtaking the low level DRV and the cyclone undergoes the strongest SLP deepening. Twelve hours later (figure 15c and d), the upper level positive PV anomaly have started merging with the low level PV anomaly. Then at the end of the 24 hour period (figure 15e and f), the upper and low level PV anomalies have merged, and formed a 'PV-tower' (see section 3.1.1 for definition of a 'PV-tower'). The cyclone has deepened from the surface to the tropopause (Boettcher and Wernli, 2013). In the second scenario the strong upper level PV is zonally oriented and there is no indication of an approaching upper level trough in relation to the low level DRV (figure 16 a and b). The situation remains more or less the same twelve hours later (figure 16c and d), the upper levels have not merged with the low level DRV. But then, the last twelve hours (figure 16e and f) the upper levels have merged with the low level DRV, and formed a PV-tower (see section 3.1.1 for explanation of a 'PV-tower'). If we can identify Nina as a DRV, we will investigate Nina further and see if it underwent one of these explosive cyclogeneis scenarios.
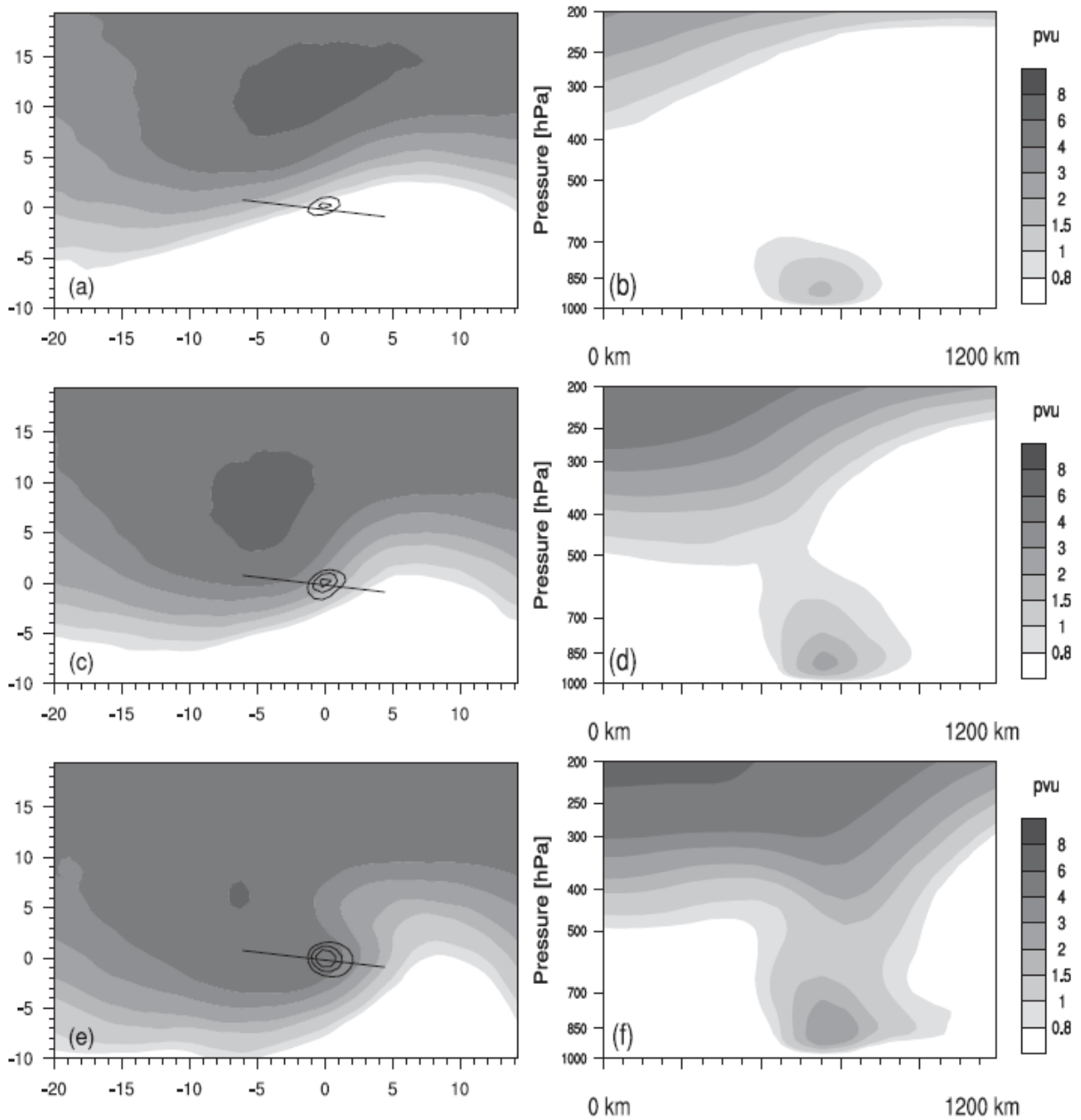
Figure 15: Composites of explosively intensifying DRV's at (a),(b) the beginning of the 24-h period of the strongest pressure deepening; (c),(d) 12 h later; and (e),(f) at the end of the strongest pressure deepening phase (i.e., at about the time of minimum SLP). Left: PV at 250 hPa (shading, PVU) and PV at 850 hPa (black contours for 1, 1.5, and 2 PVU). Right: PV (shading, in PVU) in vertical cross sections along the black lines shown in left. Figure and caption taken from Boettcher and Wernli (2013).

Figure 16: Composites (as in Figure 15) of 10 explosively intensifying DRV's identified as bottom-up cases. Figure taken from Boettcher and Wernli (2013).

3.1.4 Data and ECMWF Integrated Forecasting System

For the synoptic analysis of Nina, we have utilized analysis data from the Integrated Forecasting System (IFS), by the European Centre for Medium-Range Weather Forecast (ECMWF). The operational IFS model has a hydrostatic, two-time level, semi-implicit, semi-Lagrangian dynamical core. The physi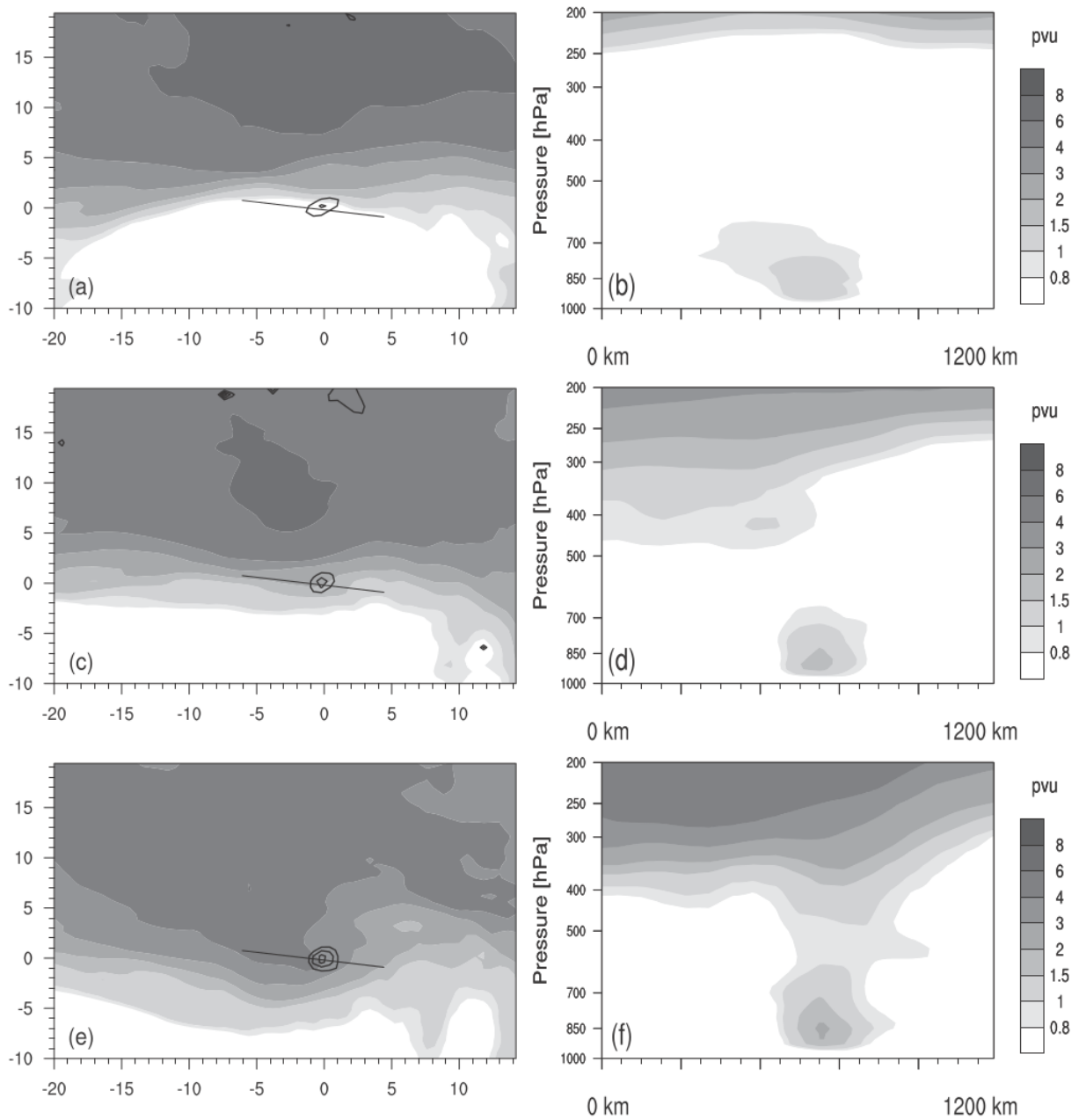cal parameterizations and advection is calculated on a reduced Gaussian grid with horizontal resolution of $0.25° \times 0.25°$. The analysis data was available with a horizontal resolution of $0.125° \times 0.125°$, however we chose $0.25° \times 0.25°$ due to lack of disk space. The model can transform between grid-point space and spectral space. The vertical has 137 levels and makes use of hybrid-pressure sigma coordinates. Analysis fields are available every 6 hours at 00, 06, 12 and 18 UTC. Prognostic variables include a wide variety of useful atmospheric parameters, such as PV on pressure surfaces and vorticity on potential temperature surfaces. Physical parameterizations include radiation, convection, clouds and stratiform precipitation, soil/surface, turbulent diffusion, orographic drag, and non-orographic gravity wave drag. The model also utilizes 4Dvar (see Kalnay (2003), for details on 4Dvar) Model description was obtained from the ECMWF documentation[9]

To plot the high resolution output data we have utilized Matplotlib (Hunter, 2007), and a Dynamical plotting Library (Dynlib) by Spensberger (2015), an extension of Matplotlib. In the synoptic analysis we have utilized a Lamber Conformal projection (see Warner (2011) for details). For the vertical cross sections we utilized data from the following pressure levels: 100, 200 ,300 ,400 ,500 ,600 ,700 ,800 ,850 ,900 and 950 hPa. The horizontal wind and PV analysis data was also available at 250 hPa.

In some figures we have utilized ERA-interim[10] data. ERA-interim is a reanalysis dataset which covers the global atmosphere from 1979-today. The ERA-interim reanalysis data has several available horizontal resolutions. We utilized a horizontal resolution of $0.5° \times 0.5°$ for our reanalysis data. The data is available at the timesteps 00, 06, 12 and 18 UTC. We declare in which figures we have utilized ERA-interim reanalysis data.

3.1.5 Modification of data

To check the six criterions needed to label a cyclone as a DRV (see section 3.1.3 for the six criterions), Boettcher and Wernli (2013) utilized operational data from ECMWF with

---

[9]http://www.ecmwf.int/en/forecasts/documentation-and-support/changes-ecmwf-model/ifs-documentation

[10]http://www.ecmwf.int/sites/default/files/elibrary/2011/8174-era-interim-archive-version-20.pdf

0.6° horizontal resolution, with timestep intervals of six hours. As mentioned in the previous section (section 3.1.4, for our analysis, we utilized analaysis data from ECMWF IFS with timestep intervals of six hours also, but with a horizontal resolution of 0.25°×0.25°. Because of this difference in horizontal resolution, we had to interpolate and modify our data to be able to check the six criteria with the same thresholds that Boettcher and Wernli (2013) set. We interpolated our data with respect to ERA-interim reanalysis data, which had a horizontal resolution of 0.5°×0.5° and utilized this interpolated data to check the six criteria needed to label Nina as a DRV. To interpolate our data, we utilized a remapping function from Climate Data Operators (Schulzweida *et al.*, 2009). This operator performs a bilinear interpolation on all input fields. It takes a text file that contains the grid information of interest, and remaps the grid of the file of interest to the grid given in the text file (see documentation by Schulzweida *et al.* (2009))

After the interpolation of the high resolution analysis data, the difference in horizontal resolution between the data Boettcher and Wernli (2013) utilized, and the modified data was 0.1°. Thus, we could assume that the thresholds set by Boettcher and Wernli (2013) should be valid for our modified high resolution analysis data.

For other modifications of the data (locating position of SLP minimum, selecting boxes, averaging), we utilized NCVIEW (Pierce, 2016) and Climate Data Operators (Schulzweida *et al.*, 2009).

3.2   Sensitivity Analysis Method and Data

3.2.1   Sensitivity in relation to strength of Nina

Since Nina was an extreme cyclone with surface wind speeds reaching ~ 30 m/s, we wanted to investigate the relative importance of the different parameters with respect to the strength of Nina. In addition, we wanted to find the location of the final field sensitivity relative to an initial nonlinear field. We achieved this by utilizing the AM and having KE as the response function (see section 2.3 for explanation of an AM and its usage.). We chose KE as the response function because this provides a good measure of the wind speed. The KE in our study is defined as:

$$KE = \frac{1}{2}(u^2 + v^2) \tag{33}$$

where u and v is the zonal and meridional velocity, respectively.

The AM run with KE as a response function, was initialized at 12 UTC 10 January

2015 (landfall of Nina) and run 36 hours backwards in time until 00 UTC 9 January 2015. The run was limited to 36 hours because the forecast with moisture is highly nonlinear and Nina is strongly influenced by moisture. The limitation of the run will maintain a satisfactory accuracy and avoid the TLM from deviating significantly from the NLM. We placed the three dimensional response function box on the approximate location of maximum low level winds at landfall of Nina (see figure 17). The box stretched from the surface to 1km altitude in the vertical. It is within this box we expect to see the change of the KE when we change the nonlinear parameters within the sensitivity fields at the final time (00 UTC 9 January 2015) of the AM run.
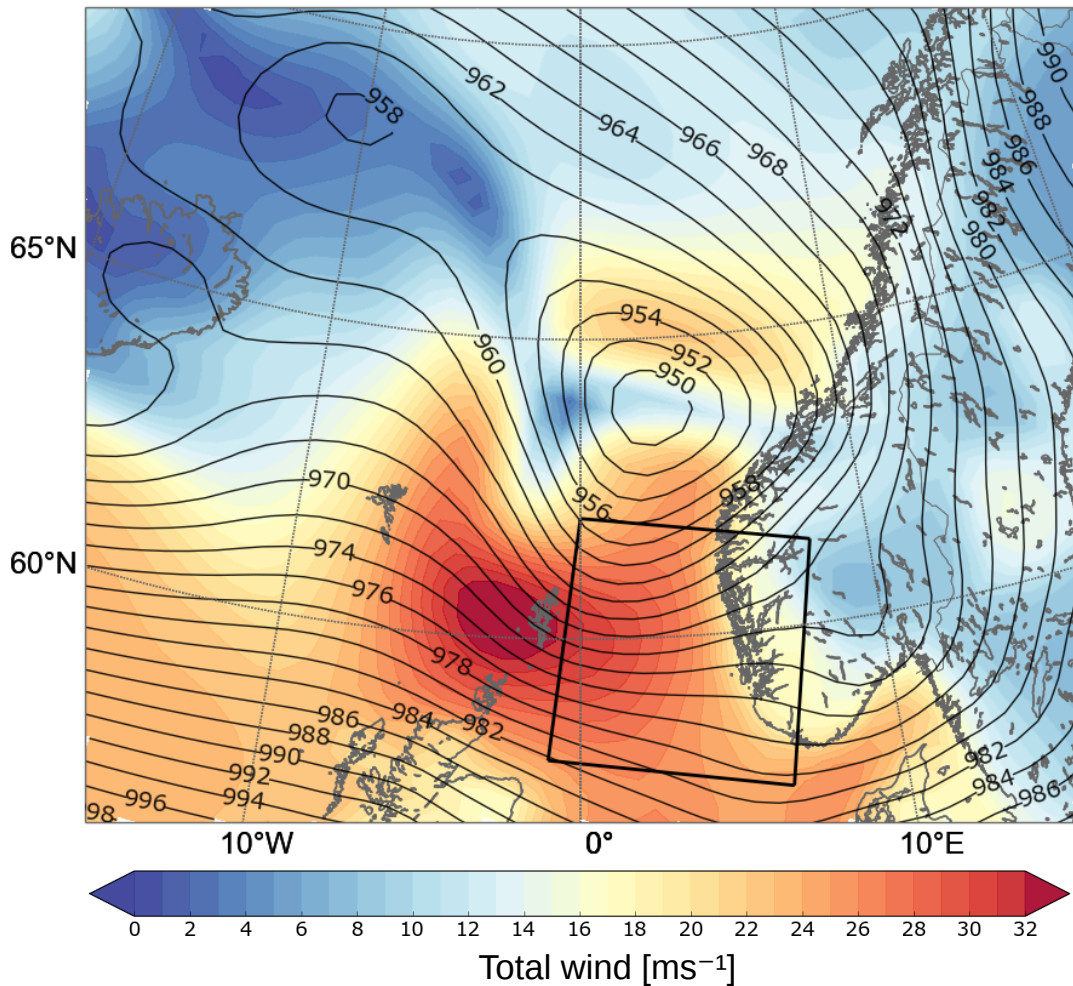

Figure 17: Approximate location of the three dimensional response function box with respect to the maximum winds of Nina, with KE (m^2/s^2) as the response function at 12 UTC 10 January 2015. The top of the box is at 1km altitude and the bottom is at the surface

Our method of analyzing the sensitivities depends on which cyclogenesis classification (see section 3.1.2 for the classifications) Nina undergoes, since we expect the sensitivities to be located in the forcing regions of the different classifications. In other words if Nina turns out to undergo the DRV classification, and since this cyclogenesis concept is highly dependent on the slope of the isentropes ahead of the cyclone (see figure 12, for a schematic of the DRV concept) in the nonlinear model field, we would expect the sensitivities to also be located ahead of the cyclone roughly at the height of condensation.

The optimal perturbations are calculated utilizing the equations presented in section 2.3.2. The optimal perturbations are to be calculated so that the KE within the response function box is maximized.

3.2.2   Sensitivity in relation to track of Nina

Since there was significant forecast uncertainty with respect to the track of Nina, we wanted to relate the sensitivity of the track to the dynamics of the cyclone. One way to examine the sensitivity of the cyclone position at the final time with respect to the initial state is to utilize a PV response function. By averaging the PV (see section 3.1.1 and equation 30, for details on how PV is defined) field from approximately 600-800 hPa and initializing the AM three hours before landfall (09 UTC 10 January 2015), we were located at a high enough elevation so that anomalous PV associated with the mountain range in southern Norway did not disturb the PV associated with Nina. We managed to exclude the anomalous PV from the mountain range and include PV associated with Nina only. By placing the three dimensional response function box to the south of Nina (see figure 38), and then defining the perturbations in the initial nonlinear model field as 'optimal', in order to maximize the PV in the response function box, we could anticipate making Nina's SLP minimum move further south towards the actual location as suggested by the analysis data by ECMWF IFS (see figure 6 in section 1.1, analysis data from COAMPS nonlinear model was not available). The AM run with PV as a response function, was initialized at 09 UTC 10 January 2015 and run 33 hours backwards in time until 00 UTC 9 January 2015.

Our analysis of the PV sensitivities depends on which classification Nina can undergo. If Nina could be identified as a DRV, we will focus on the sensitivities located in the forcing regions of the DRV concept. For the DRV, the forcing regions are located ahead of the cyclone (see section 3.1.2), thus we will focus on the sensitivities located here.
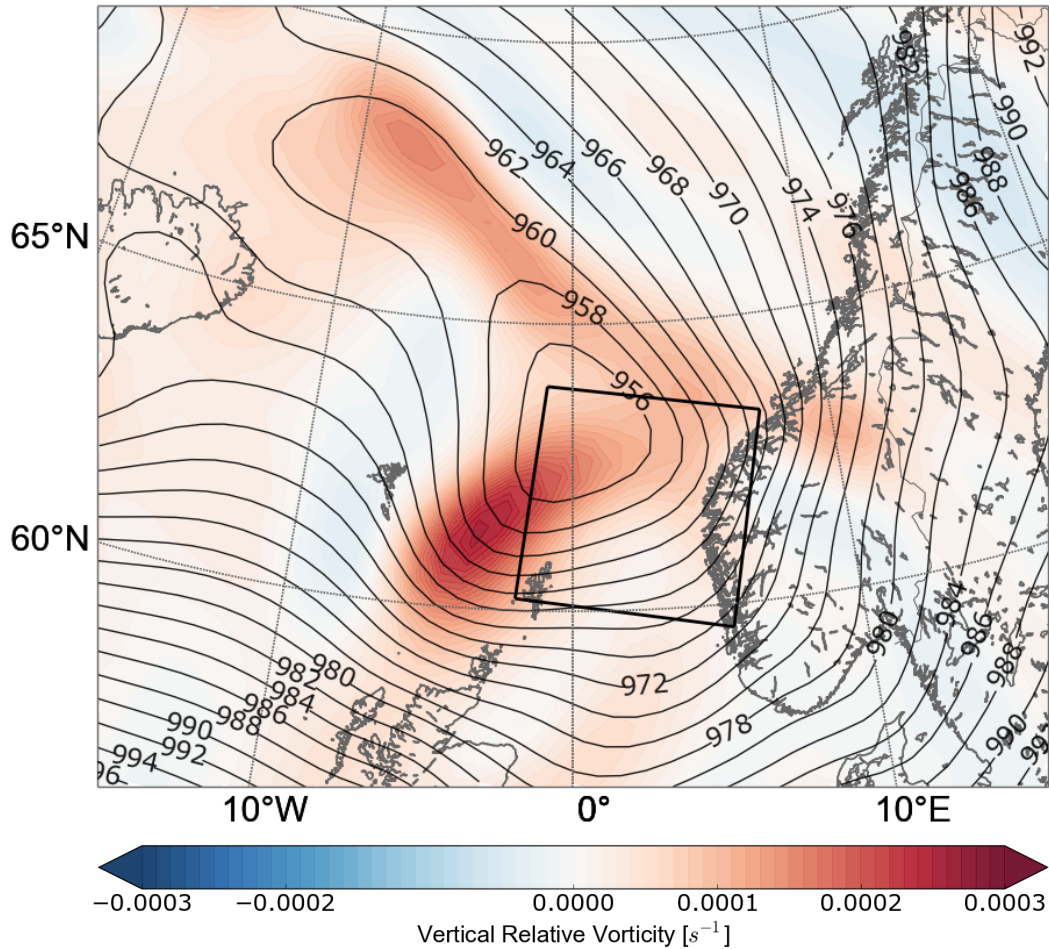
Figure 18: Approximate location of the three dimensional response function box at 2500 meters above sea level where the PV (PVU) was chosen as a forecast response function at 09 UTC 10 January 2015. The box is approximately located at 600 (top)-800 (bottom) hPa.

3.2.3   COAMPS Nonlinear, tangent linear and adjoint model description

The following sections describe the Coupled Ocean/Atmosphere Mesoscale Prediction System (COAMPS) nonlinear, tangent linear and adjoint models. The output data from all the COAMPS models have been plotted by utilizing Hunter (2007) and COAMPS Visualization In Python (COVIP) (Flagg, 2013). The data was available on sigma levels and some pressure levels. A code was provided in COVIP (Flagg, 2013), which interpolates to various vertical coordinates. In the sensitivity analysis we have utilized a rotated Stereographic projection (see Warner (2011), for details).

3.2.4 The nonlinear model

The nonlinear COAMPS model (Hodur, 1997) contains the fully compressible nonhydrostatic equations. Following Klemp and Wilhelmson (1978), the compressible equations are efficiently integrated by solving the vertical acoustic modes with a semi-implicit formulation. The numerical solution of the equations utilizes second order finite-difference approximation, although higher-order alternatives are available. The equations are solved on a limited area staggered Arakawa C grid, with a 45km horizontal resolution (Arakawa and Lamb, 1977). The zonal and meridional wind grid points are staggered one half grid points compared to the mass grid points. The grid contains 201x161 points. With an exception of the perturbation pressure, a fourth order accurate horizontal diffusion is utilized for all variables. The horizontal diffusion effectively dampens short wavelengths in the horizontal, which has the effect of extenuating nonlinear instability. The vertical wind grid points are collocated with the mass grid points. The model has 45 vertical levels, and makes use of a terrain following vertical sigma coordinate transformation, to allow for complex topography. The topography is based on on a digital resolution model with 1 km resolution (GLOBE Task Team and others, 1999). The model top is at a 30 km height. To account for reflection of vertically propagating gravity waves a upper boundary sponge condition is utilized. Prognostic variables include u, v, w, the Exner function, potential temperature, microphysical species, water vapor and turbulent kinetic energy.

The model utilizes several complex physical parameterizations. A modified Kuo convective parameterization, following Molinari (1985), represents the subgrid-scale deep convection. A modified version of Rutledge and Hobbs (1983) explicit moist physics is used to represent the cloud microphysical processes. The surface fluxes and surface energy budget is based on parameterizations by Louis (1979). A prognostic total KE budget equation (Hodur, 1997) parametrizes the free atmospheric turbulent mixing and diffusion, and the planetary boundary layer. Radiation and ice processes are also parametrized. For our sensitivity analysis the radiaion parameterization is neglected, due to the nonlinearities with respect to this parameterization. Model description is based on Hodur (1997), Doyle *et al.* (2013), and the COAMPS model documentation by Chen *et al.* (2003).

43

3.2.5   COAMPS Tangent linear and adjoint models

The tangent linear and adjoint COAMPS model (Amerault *et al.*, 2008) has a nonhydrostatic dynamical core and utilizes the same physical parameterizations as the nonlinear model, also excluding radiative processes. This is to avoid significant challenges in relation to the nonlinearity of such processes. The models have a horizontal resolution of 45 km, and 45 vertical levels. To avoid discontinuities in relation to switches and decision points, they are identical in the nonlinear, tangent linear and adjoint models (Zou *et al.*, 1993; Vukicevic and Errico, 1993). We have neglected gradients and perturbations due to vertical diffusion (Mahfouf, 1999). To make sure the tangent linear and adjoint model has sufficient accuracy, the nonlinear output data was saved every 3 hours and the tangent linear and adjoint model was also output at the same frequency. Description of the tangent linear and adjoint model is based on Doyle *et al.* (2013), and Amerault *et al.* (2008).

3.2.6   Adjoint model evaluation

In this study, we are utilizing initial condition sensitivity to explore the dynamics and predictability of Nina. In order to utilize the sensitivity with confidence, we need to be certain that the adjoint modeling system is valid and appropriate in this application.

In general, the agreement between the TLM and NLM depends on; the exact size and shape of the perturbations, synoptic features of the reference state, physics involved, time period over which perturbation evolves, and the metric used for comparison (Errico and Reader, 1999). Due to the dependence between the TLM and the AM, these accuracy dependencies applies to the AM too. It should also be mentioned that even though we take all precautions and try to make the AM as accurate as possible, the AM is only accurate to the extent that the NLM forecast is accurate. The validity of the AM may also depend on the horizontal resolution in the NLM.

To test the accuracy and correctness of the COAMPS TLM and AM, they have undergone a series of tests. The results of a perturbation test and a numerical gradient check, indicate that the AM has been accurately coded. The test results of the adjoint codes are presented in Amerault *et al.* (2008). The validity of the tangent linear approximation has been tested by utilizing the gradient fields to construct optimal perturbations. Deriving the optimal perturbations from the adjoint gradients and evolving them in the tangent linear and nonlinear model is a standard method to check the validity of the tangent linear approximation for the chosen integration length (similar evaluation can be found in Doyle

et al. (2013)). The perturbation from the NLM is defined as the difference between the control state nonlinear forecast and the nonlinear forecast from the perturbed state. When the evolved perturbations in the nonlinear and TLM is of similar magnitude and have the same structure at the final time, the TLM can be considered useful.

One way of quantifying the appropriateness of the tangent linear approximation, is to compute the correlation over the region in which the forecast aspect, J, is applied. The correlation coefficient can be utilized to measure the coherence between the NLM and the TLM. We have calculated the correlation between the optimal perturbations evolved in the TLM and NLM within the response function box for PV and KE, at the height where the correlations are largest, for both response functions (see table 1). All correlations for both response functions are above 0.7 magnitude, except for the correlation between the evolved optimal specific humidity perturbations.

Parameter	NLM Variable Name	NLM Variable Name	KE correlation	PV correlation
Zonal wind (u, m/s)	aaauu1	aaauu2	0.71	0.81
Potential temperature (θ, K)	aaath1	aaath2	0.71	0.71
Specific humidity (kg/kg)	aaaqv1	aaaqv2	0.51	0.73

Table 1: Correlation between evolved optimal perturbations in TLM and NLM with KE and PV as response functions. The correlation is taken within the response function boxes.

By comparing the evolved optimal u perturbation in the COAMPS tangent linear (a) and COAMPS nonlinear (b) model on figure 19 and 20 , we can see that the TLM (a) is able to capture the main structures of the nonlinear model well, and the magnitudes to a good degree, with PV and KE as a response function. The TLM minimum and maximum values are somewhat higher for all the anomaly areas, compared to the NLM. The maximum magnitude difference between the TLM (a) and NLM (b) is about $\sim 10 m/s$.

Based on comparisons between (a) and (b) in figure 19 and 20, and the correlations (see table 1) within the response function boxes over the 36-h (KE) and 33 h (PV) integration length, we conclude that the AM is appropriate to apply in this case for both the KE and PV response functions. Perturbations evolved in the NLM and the TLM are in very good agreement in spite of the rather complex structures, and the magnitudes agree quite well

(10 m/s maximum difference). The differences are due to nonlinearities since an exact adjoint of the NLM is used. It should be noted that these nonlinearities have a small horizontal extent. We have confidence that the AM will provide a reliable estimate of the initial condition sensitivity, including identifying the most sensitive variable, as well as the sensitivity magnitude and location.

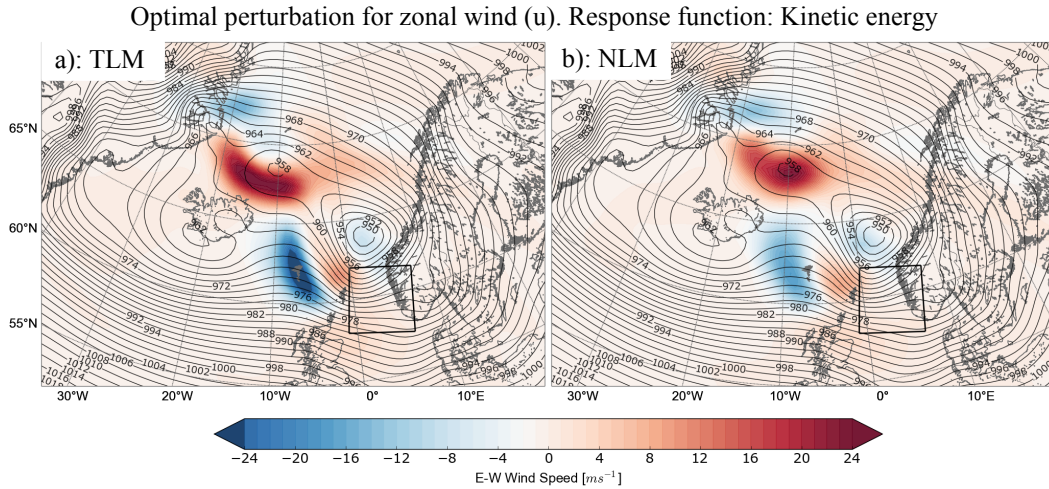Figure 19: Zonal wind (u) adjoint optimal perturbations at 6500 m evolved in the TLM (a) and the NLM (b), with KE as response function. Mean SLP NLM at 12 UTC 10 January 2015 (black contours, 2 hPa interval). The black box is the approximate position of the KE response function box.
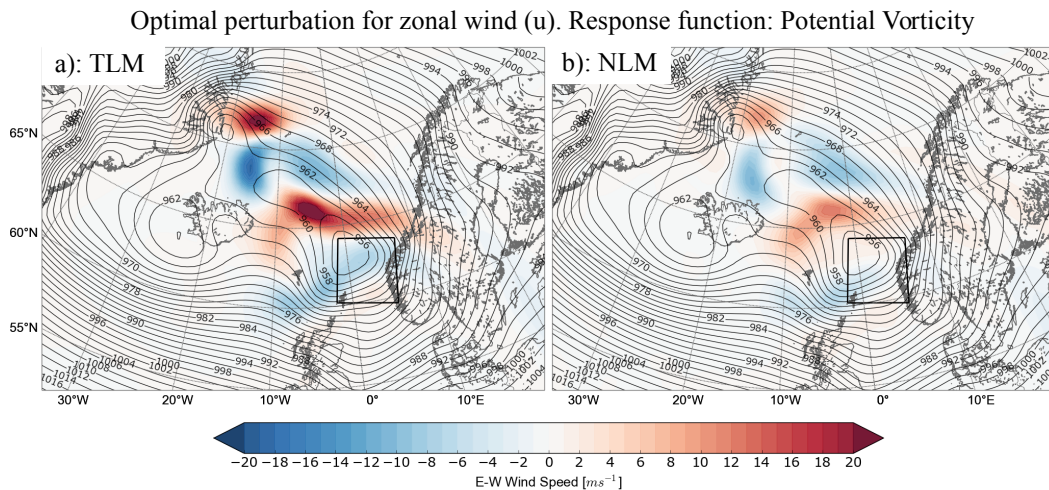

Figure 20: Same as figure 19, but with PV as the response function. Black box is now the approximate position of the PV response function box.

4   Synoptic analysis of Nina

4.1   Synoptic environment during genesis and propagation phase of Nina
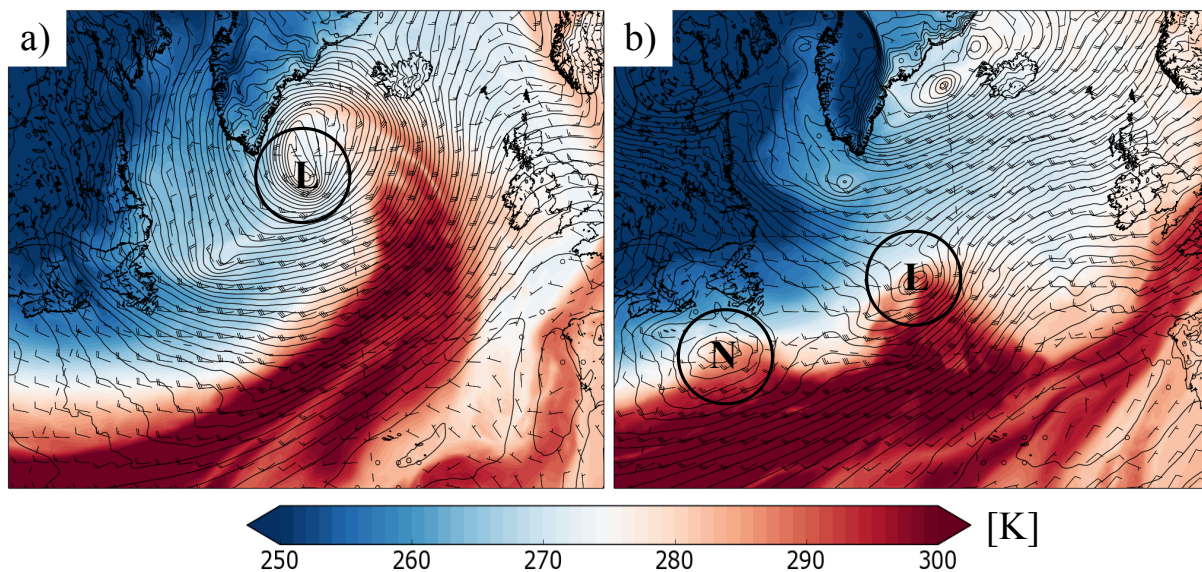

Figure 21: Equivalent potential temperature (shading, K), SLP (black contours) and wind (barbs, m/s) for timesteps a): 18 UTC 6 January 2015 b): 06 UTC 8 January 2015. The 'L' signifies SLP minimum of a low pressure system which created favorable conditions for formation of a DRV. The 'N' signifies the position of Nina.

The atmosphere in the North Atlantic sector featured an anomalously strong temperature gradient and jet stream during the formation of Nina. Together with significant moisture intrusion into mid and higher latitudes, the conditions were conducive for DRV formation (see section 3.1.3 additional details on favorable DRV formation conditions).

The anomalously strong jet stream (see figure 2 and 4) during the week of Nina's development (7 January 2015 - 11 January 2015) featured maximum wind speeds reaching a staggering 116 m/s at 300 hPa. The jet stream was ~ 42 m/s stronger than the average jet stream from 1979 - 2015 (see figure 2). The anomalous jet stream implies an anomalous intense horizontal temperature gradient via the thermal wind relation (see section 2.2).

Two consecutive low pressure systems (see figure 21a and b) aided the significant moisture intrusion into the mid and higher latitudes. The first large cyclone advected warm, moist air up to the coast of Ireland (see figure 21a). While the second low pressure system

enhanced the intrusion of the moist air from the large low pressure system (see figure 21b). This resulted in very moist air ($\sim$ 30-40 kg/m^2) located directly south of Nina (see figure 22a) and the baroclinic zone was continuously fed with moist, warm air while Nina was translating across the North Atlantic ocean.
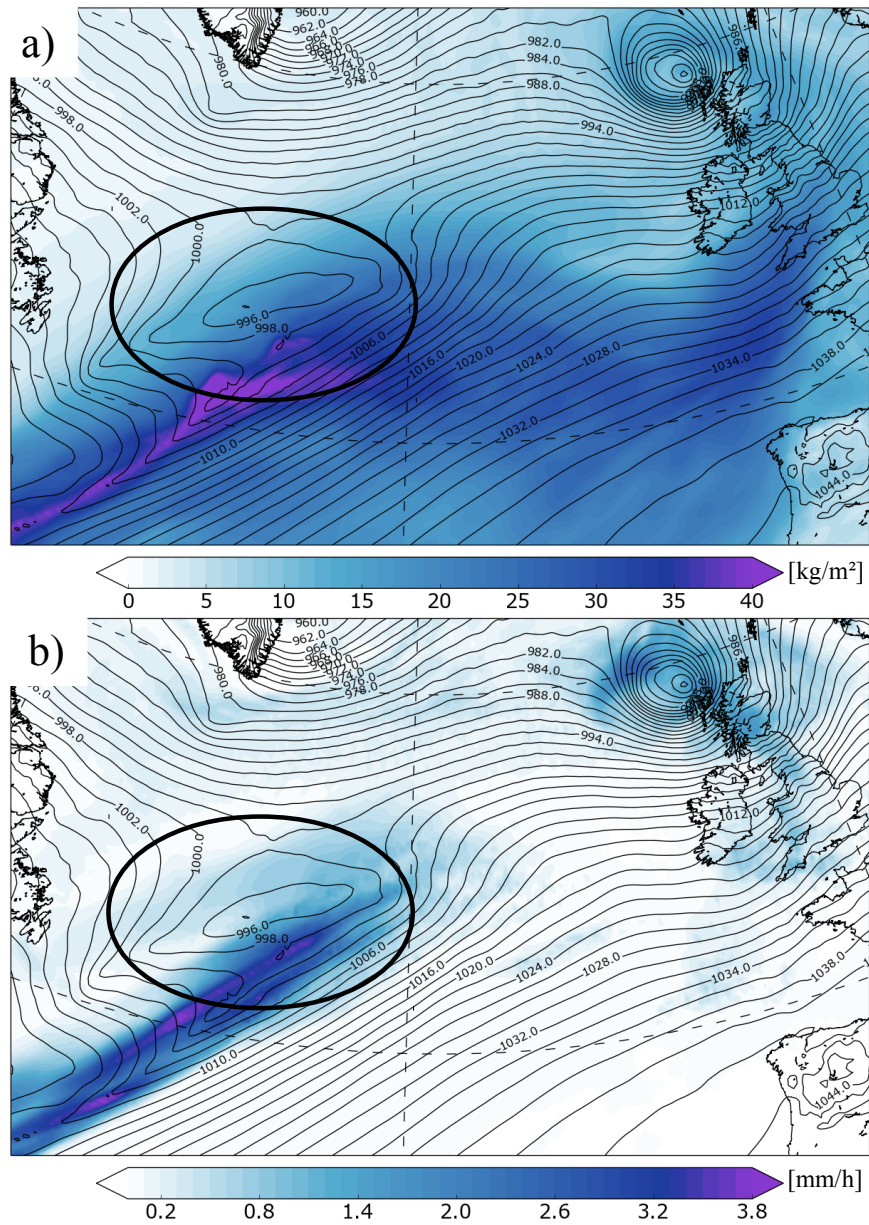

Figure 22: a): Total water column (shading, kg/m^2) and SLP (black contours, 2 hPa interval), b): Accumulated precipitation over one hour (shading, mm/h) and SLP (black contours, 2 hPa interval).

Moisture can readily ascend along the isentropes (constant lines of potential temperature) or moist isentropes (constant lines of equivalent potential temperature) depending on whether or not the air is saturated ahead of Nina, because of Nina's cyclonic circulation. The ascending moist air may have made Nina able to self-sustain through latent heat release associated with condensation of the moist air. The precipitation (see figure 22b) shows that the moisture was able to ascend to saturation, which implies latent heat release. Cyclones that propagate like this are heavily influenced by latent heating and may evolve into "bombs" (Zhu and Newell, 1994), which is exactly what happened to Nina (see section 1). Another important criterion for DRV formation and growth is minimal friction. Since the entire life cycle of Nina is over ocean, it implies less surface friction compared to that over land.

4.2   Upstream upper level trough during genesis and propagation phase of Nina

The synoptic environment during Nina is strikingly similar to scenario C with the presence of an upstream upper level trough in relation to the low level cyclone presented on figure 13 in section 3.1.3. For an easy comparison, we provided scenario C on figure 23a, together with the synoptic environment at the genesis time (18 UTC 7 January 2015) of Nina, figure 23b. Nina formed downstream of an upper level trough, in the trailing baroclinic region (see white θ contours) of a preceding extratropical cyclone (see 'L' and 'N' on figure 23b).

Twenty four hours after genesis at 18 UTC 8 January 2015, Nina began propagating quickly across the North Atlantic within a baroclinic zone (see figure 4 in section 1). Nina propagated ~ 2000 km, from east of Newfoundland to west of Ireland/Scotland in 24 hours (18 UTC 8 January - 18 UTC 9 January), which is equivalent to an average speed of 23 m/s.

Based on the analysis of the synoptic environment from 6-9 January 2015 just presented, the data indicates Nina formed in an environment conducive to DRV genesis and growth. It is therefore valid to test the six criteria presented in section 3.1.3.
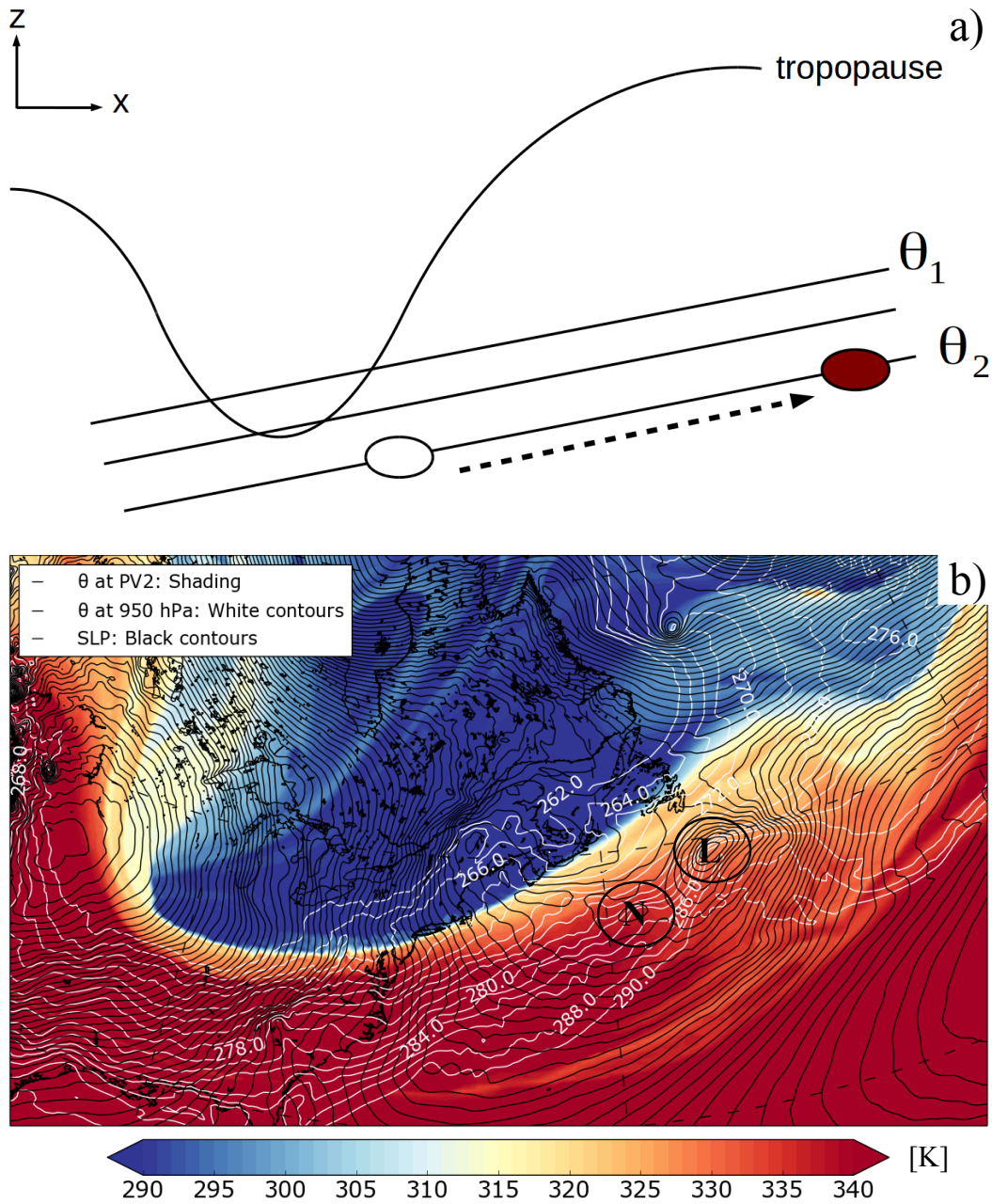
Figure 23: a): Scenario C on figure 13. The white ellipse represents the initial time of the DRV and the grey ellipse represents the beginning of the DRV propagation phase. θ represents the region of baroclinicity. See text for detailed explanation (Boettcher and Wernli, 2013). b): Synoptic environment situation during genesis of Nina at 18 UTC 7 January 2015. The 'N' and 'L' marks the position of Nina and a preceding low pressure system, respectively. PV at tropopause (shading, K), SLP (black contours), and θ at 950 hPa (white contours, 2 K interval).

4.3   Results of Diabatic Rossby Vortex identification

By utilizing the method presented in section 3.1.3, we will investigate if we can classify Nina as a DRV during Nina's genesis (18 UTC 7 January 2015 - 12 UTC 8 January 2015) and propagation phase (18 UTC 8 January 2015 - 12 UTC 9 January 2015). We will go consecutively through each criterion and present them in a table at the end of the section.

Criterion one, a SLP minimum, is fulfilled. The track of Nina and the evolution of the SLP with time (see figure 4 and 5) clearly displays a sea level pressure minimum at all timesteps from 18 UTC 7 January 2015 - 12 UTC 9 January 2015.

Criterion two, which involves a collocated positive PV anomaly at 850 hPa (> 0.8 PVU) with the SLP minimum, was not fulfilled four of eight timesteps. However, by inspecting the ambient region of each timestep that was not fulfilled (see figure 24), it can easily be argued that there was anomalously large values of PV at these respective timesteps too .

The average PV within the box was not above 0.8 PVU at the timesteps 18 UTC 7 January (a), 06 UTC 8 January (b), 12 UTC 8 January (c), and 00 UTC 9 January (d) (see figure 24). The red color designates PV anomalies above the 0.8 PVU threshold, while the blue areas designate PV values below the threshold of 0.8 PVU (see figure 24). For three of these timesteps it can be seen that there is PV values above the threshold close to the SLP minimum ((a), (b) and (d)). It is not co-located with the SLP minimum, but it is very close. For timestep 12 UTC 8 January (c), the average PV within the box was 0.71 PVU, just below the threshold of 0.8 PVU. Boettcher and Wernli (2013) state themselves that the PV anomaly of 0.8 PVU was 'somewhat arbitraily chosen', which indicates that the PV anomaly does not necessarily have to be above 0.8 PVU at all timesteps.

Another point to make regarding the unfulfillment of the PV anomaly is that since Nina is located at relatively high latitudes, and moves farther north during cyclogenesis, the longitude distance changes (see how the small black box becomes narrow on figure 24), and covers a smaller area the further north the cyclone moves. The fact that this happens, may have caused the average PV to be smaller than 0.8 PVU at some of the respective timesteps, because the box becomes smaller. We found no indication that Boettcher and Wernli (2013) takes the change of longitude with latitude into account. A proposed improvement of this criterion, would be to utilize a great circle (see Warner (2011) and Geodesic grids), this way the problem with the change of longitude with latitude would be obsolete. The fact that data different from Boettcher and Wernli (2013) was utilized, and that the data was smoothed and interpolated, may also be potential cause why this criterion was not fulfilled at the respective timesteps.
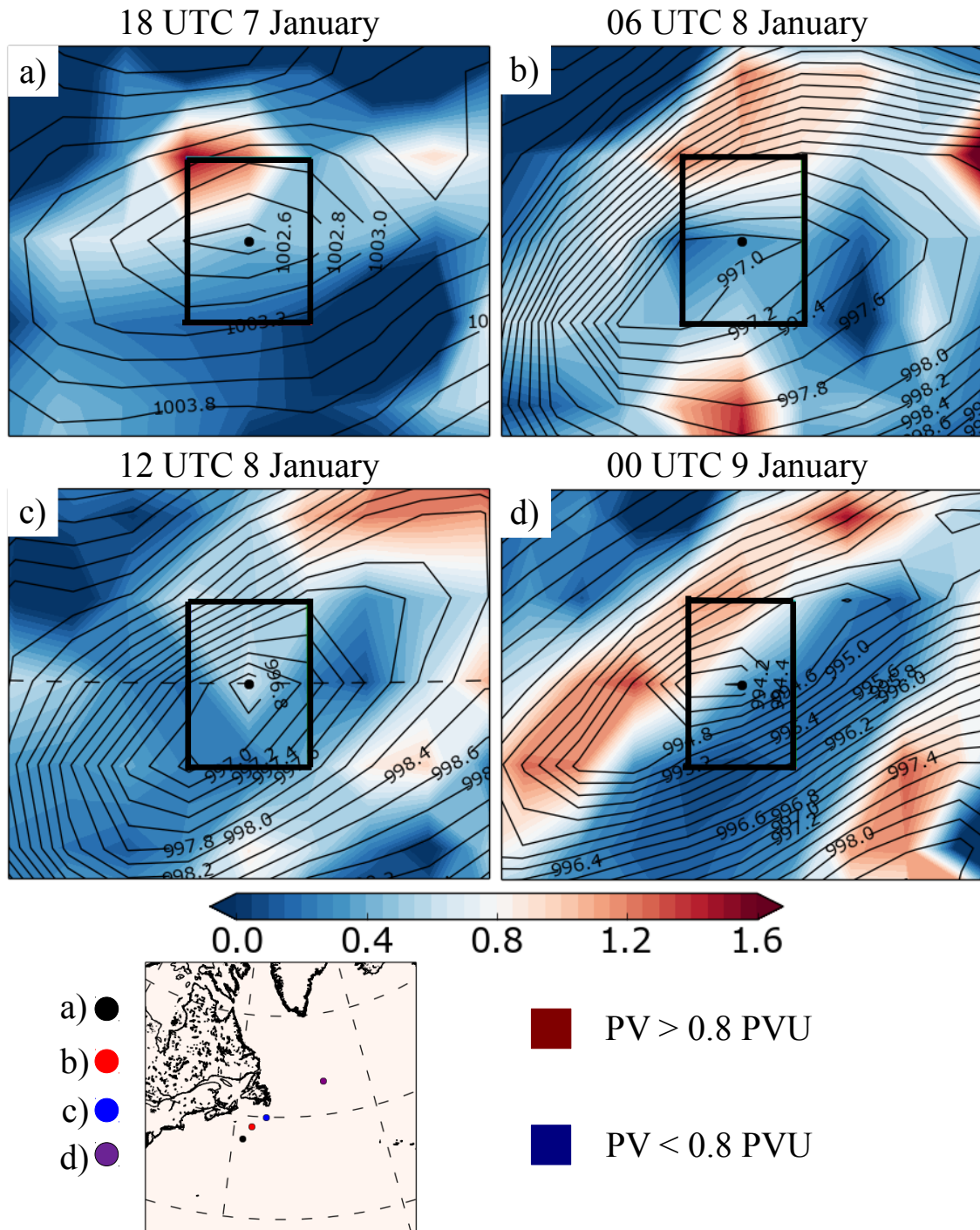
51

Figure 24: PV at 850 hPa (shading, PVU) and SLP (black contours, 0.3 hPa interval) taken over the SLP minimum of Nina at the unfulfilled timesteps for criterion two. See top of each figure for the time. The black box designates the area where the average PV at 850 hPa was taken.

Criterions three to six did not have to be fulfilled from genesis to the end of the propagation phase. These criterions had to be fulfilled at least three timesteps (see section 3.1.3). Careful inspection of every relevant timestep showed that 00 UTC January, 06 UTC 9 January and 12 UTC 9 January, were potential candidates for fulfillment of the remaining criteria.

Criterion three involved strong baroclinicity (> 5 K) in the lower levels. The baroclinicity was 16.30 K at 00 UTC 9 January, 10.45 K at 06 UTC 9 January, and 9.39 K at 12 UTC 9 January, so this criterion was fulfilled. Criterion four, a propagation speed of at least 11.6 m/s was also fulfilled. The propagation speed was 38.68 m/s, 37.74 m/s and 29.17 m/s from 18 UTC 8 January 2015 - 00 UTC 9 January 2015, 00 UTC - 06 UTC 9 January 2015, 06 - 12 UTC 9 January 2015, respectively.

Criterion five, enough condensational latent heat release ($RH_{10th} > 90$ %) was also fulfilled. According to Boettcher and Wernli (2013), this is the most critical criterion of the six, because the fundamental process enabling DRV genesis is latent heat release and low-level PV generation. The tenth percentile of the relative humidity was 100.62 %, 100.40 % and 100.71 % at 00, 06 and 12 UTC 9 January 2015, respectively. The air was supersaturated at these timesteps, providing strong evidence that latent heat release was ongoing and of sufficient magnitude to justify the DRV classification.

The first part of criterion six, average PV at 250 hPa above Nina < 1.0 PVU was fulfilled while Nina was propagating over the North Atlantic Ocean. The PV above Nina was 0.19 PVU, 0.01 PVU and 0.48 PVU at 00, 06 and 12 UTC 9 January 2015, respectively. This indicates that the upper level trough was not above Nina at these timesteps.

The second part of criterion six following Boettcher and Wernli (2013) utilizes the QG omega equation to quantify the upper level forcing. However as indicated in section 3.1.3, since we are inspecting one extratropical cyclone, a manual inspection should suffice. The potential temperature at the tropopause shows the location of the upper level trough located upstream of Nina (see figure 25). At 18 UTC 8 January 2015 (figure 25a), Nina is likely influenced by the upper level trough due to the short horizontal distance between the low level cyclone and the upper level trough. The upper level influence can be seen by the 'kink' of the isentropes at 950 hPa. However at 00, 06, 12 UTC 9 January 2015 (see figure 25b, c and d), we can see that Nina has propagated away from the upper level trough and that the upper level trough is more or less stationary. This implies that Nina cannot have been heavily influenced by the upper level trough during its propagation over the North Atlantic ocean. For Nina to be heavily influenced by the upper level trough, Nina and the upper levels would have to be phase locked (Boettcher and Wernli, 2013).

Based on this analysis it seems that the second part of criterion six is also fulfilled. We realize that the horizontal distance is not large enough to say that there was no influence of the upper levels during these timesteps.n A PV anomaly (of size ∼ 2 PVU) can actually influence the low levels up to 1000km away (Holton and Hakim, 2012). However, criterion 6.2, indicate that some upper level forcing is allowed during the evolution of a DRV. The requirement is that the upper level forcing cannot be significant.
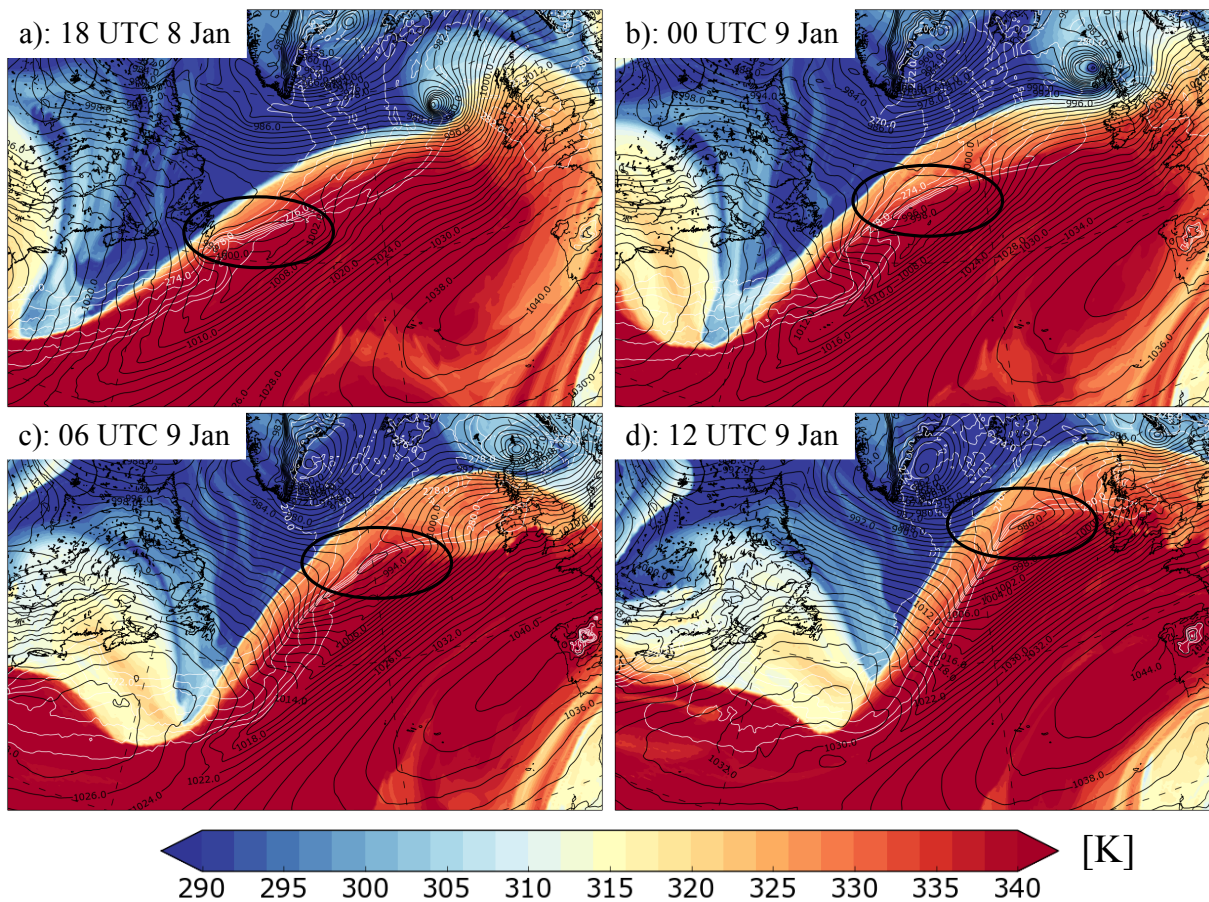
Figure 25: Potential temperature at the tropopause (shading, K) and mean SLP (black contours, 2 hPa interval) for timestep 18 UTC 8 January 2015 (a), 00 UTC 9 January 2015 (b), 06 UTC 9 January 2015 (c) and 12 UTC 9 January 2015 (d).

From further investigation, we found that there is a significant positive PV anomaly (∼ 4 PVU) located southeast of Nina at 500 hPa at 00 UTC 9 January 2015 (see figure 26), and due to its close proximity to the surface cyclone it may have had an effect on the surface cyclone. The southeasterly wind beneath the PV anomaly at 600 hPa indicates the

strength of the cyclonic circulation associated with this PV anomaly (see grey contours on figure 26b), considering there is northwesterly flow almost everywhere else in the field. We believe that this positive PV anomaly is not associated with the upper level trough. This positive PV anomaly may have formed due to diabatic processes associated with the extreme moisture (> 40 kg/m^2) and the intense front (seen by the kink in the surface pressure) located southeast of Nina (see figure 22a and b). The positive PV anomaly does not influence Nina for long, because at 06 UTC 9 January 2015 it is no longer evident. Possibly due to Nina's rapid propagation or due to erosion from significant negative PV anomalies also associated with diabatic processes.
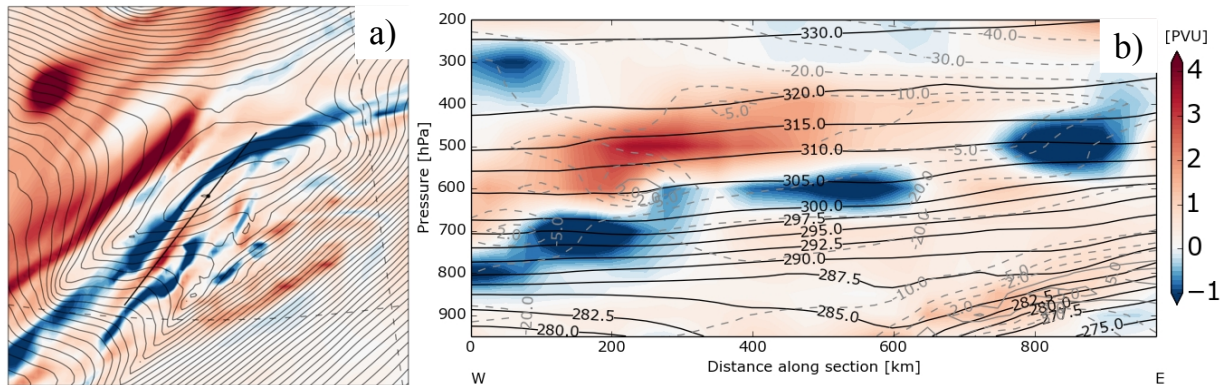

Figure 26: a) PV (shading, PVU), SLP (black contours, 2 hPa interval). The black line shows the vertical cross section in (b). b): PV (shading, PVU), potential temperature (black contours), wind (m/s, grey contours, dashed out of page). Timestep: 00 UTC 9 January 2015

To summarize the threshold values of the six criterions presented above, we have made three tables. Table 2, contains the SLP minimum and location for each timestep of Nina's genesis and propagation stage (18 UTC 7 January 2015 - 12 UTC 9 January 2015). In addition, it contains the average PV at 850 hPa within the eight neighbouring points of the SLP minimum.

Table 3 contains the calculated treshold values for criterions 3-6 for the timesteps during Nina's propagation phase (00 UTC 9 January 2015 - 12 UTC 9 January 2015). Table 4 contains details on how many calculated values were within the threhold values for each timestep and in total. After closer investigation we can with confidence say that six out of six criterions were fulfilled during the genesis and propagation phase of Nina, and that Nina can undergo the DRV classification. It should be mentioned that the DRV identification method presented by Boettcher and Wernli (2013) would not have categorized Nina as a DRV and that their identification method may need more specific criteria and thresholds.
55

Criterion	1		2	
Timestep	PV_{avg} at 850 hPa > 0.8 PVU		SLP minimum	Location(lon, lat)
Genesis phase				
7 Jan 18 UTC	0.50 PVU		1002.49 hPa	[-58.0,41.5]
8 Jan 00 UTC	1.10 PVU		999.87 hPa	[-58.5,42.0]
8 Jan 06 UTC	0.71 PVU		996.92 hPa	[-56.5,43.5]
Propagation phase				
8 Jan 12 UTC	0.48 PVU		996.61 hPa	[-53.5,45.0]
8 Jan 18 UTC	1.00 PVU		996.02 hPa	[-50.5,46.5]
9 Jan 00 UTC	0.50 PVU		993.99 hPa	[-40.5,50.0]
9 Jan 06 UTC	1.05 PVU		989.02 hPa	[-30.5,54.0]
9 Jan 12 UTC	0.82 PVU		983.40 hPa	[-22.0,57.0]

Table 2: Results for criterion 1 and 2. The location of the slp minimum is also presented in the table.

Criterion	3	4	5	6.1
Timestep	($\Delta\theta$ > 5 K)	(V > 11.6 m/s)	$RH_{10th\%}$ ¿ 90%	PV_{avg} 250 hPa < 1.0 PVU
9 Jan 00 UTC	16.30 K	38.68 m/s	100.62%	0.19 PVU
9 Jan 06 UTC	10.45 K	37.74 m/s	100.40%	0.01 PVU
9 Jan 12 UTC	9.39 K	29.17 m/s	100.71%	0.48 PVU

Table 3: Results for criterion 3, 4, 5, and 6.1

Criterion	Timesteps fulfilled
1-2, must be fulfilled all timesteps	
1: SLP min > 0.5 hPa than closest contour	8/8
2: Collocated PV max > 0.8 PVU	4/8 (see dicussion of criterion 2)
3-6, must be fulfilled 3 timesteps	
3: Avg. baroclinicity, $\Delta\theta$ > 5 K	3/3
4: Propagation speed, V > 11.6 m/s	3/3
5: Avg. $RH_{10th\%}$ > 90%	3/3
6.1: Avg. PV at 250 hPa < 1.0 PVU	3/3
6.2: Upper level forcing not significant	3/3
Total criterions fulfilled	6/6

Table 4: Fulfilled criterions at individual timesteps and total.

With the six criteria criteria being fulfilled, Nina can now be classified as a DRV during the genesis and propagation phase. The atmosphere featured anomalously large baroclinicity and moisture content. In addition, Nina propagated at a sufficient speed and the upper level tropopause fold was at such a distance that it cannot have influenced Nina significantly during the propagation phase.

4.4   Intensification phase of Nina

In section 1.1 we stated that Nina was a 'bomb' cyclone based on the definition by Sanders and Gyakum (1980). Because of this we would like to investigate if Nina, in addition to undergoing cyclogenesis similar to a DRV, can be classified as an explosive DRV by utilizing the method presented in section 3.1.3. From 12 UTC 9 January 2015 - 12 UTC 10 January 2015, Nina deepened 34.6 hPa in twenty four hours ($\sim$ 1.4 hPa/hr), which is equivalent to $\sim$1.4 Bergerons. This is above the threshold of 1 Bergeron which is needed to qualify for explosive cyclogenesis (see 2.1 and equation 11, for details on how to calculate the Bergeron). We provided figure 15 in this section too, for an easier comparison (see figure 27). If we compare figure 27 and 28, we can see that Nina's intensification phase matches the explosive DRV scenario presented in section 3.1.3. First, the tropopause fold upstream begins overtaking the low level DRV (see figure 28a and b). Then the tropopause fold and the low level DRV starts merging (c and d) eventually it forms a PV-tower (e and f). The wind (see grey contours on figure 27d, e and f), indicate how the depth of Nina increases from 850 hPa to 400 hPa. The depth increase matches the expectation of a rapidly intensifying cyclone, a large depth increase of the cyclonic circulation. Since, from 12 UTC 9 January 2015, the upper level trough starts merging and phase locks with the low level features of Nina, during the intensification phase, Nina undergoes explosive cyclogenesis typical for a type C cyclone. The upper level tropopause fold overtakes the low level cyclone and the vorticity in relation to both the upper levels and low levels coalesce, leading to an extreme deepening of the sea level pressure. Because of the striking similarities between Nina's intensification phase and Boettcher and Wernli (2013)'s composite of explosive DRV's, Nina can be classified as an explosive DRV.
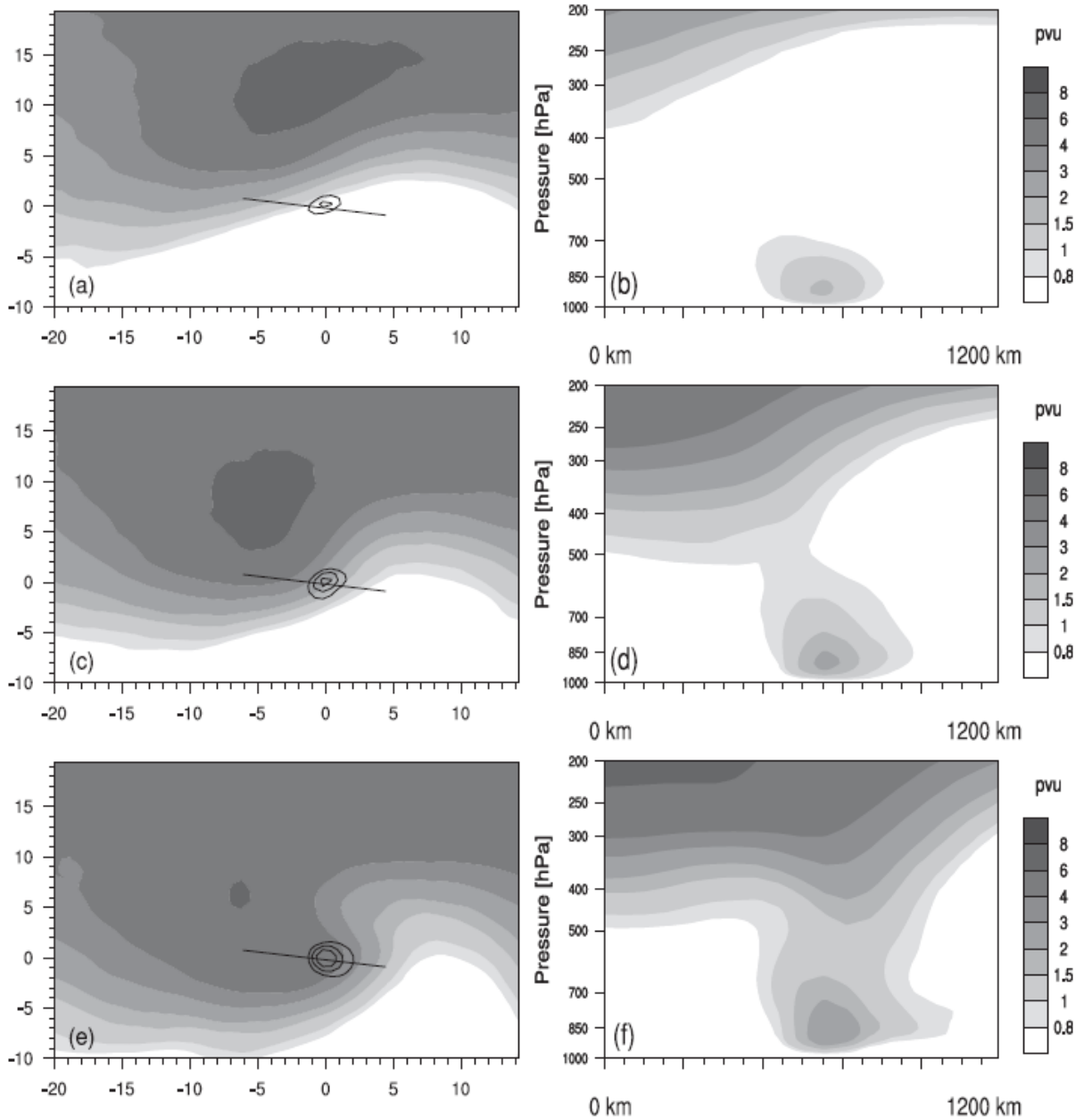
Figure 27: Composites of explosively intensifying DRV's at (a),(b) the beginning of the 24-h period of the strongest pressure deepening; (c),(d) 12 h later; and (e),(f) at the end of the strongest pressure deepening phase (i.e., at about the time of minimum SLP). (left) PV at 250 hPa (shading, PVU) and PV at 850 hPa (black contours for 1, 1.5, and 2 PVU). (right) PV (shading, in PVU) in vertical cross sections along the black lines shown in (left). Figure taken from Boettcher and Wernli (2013).
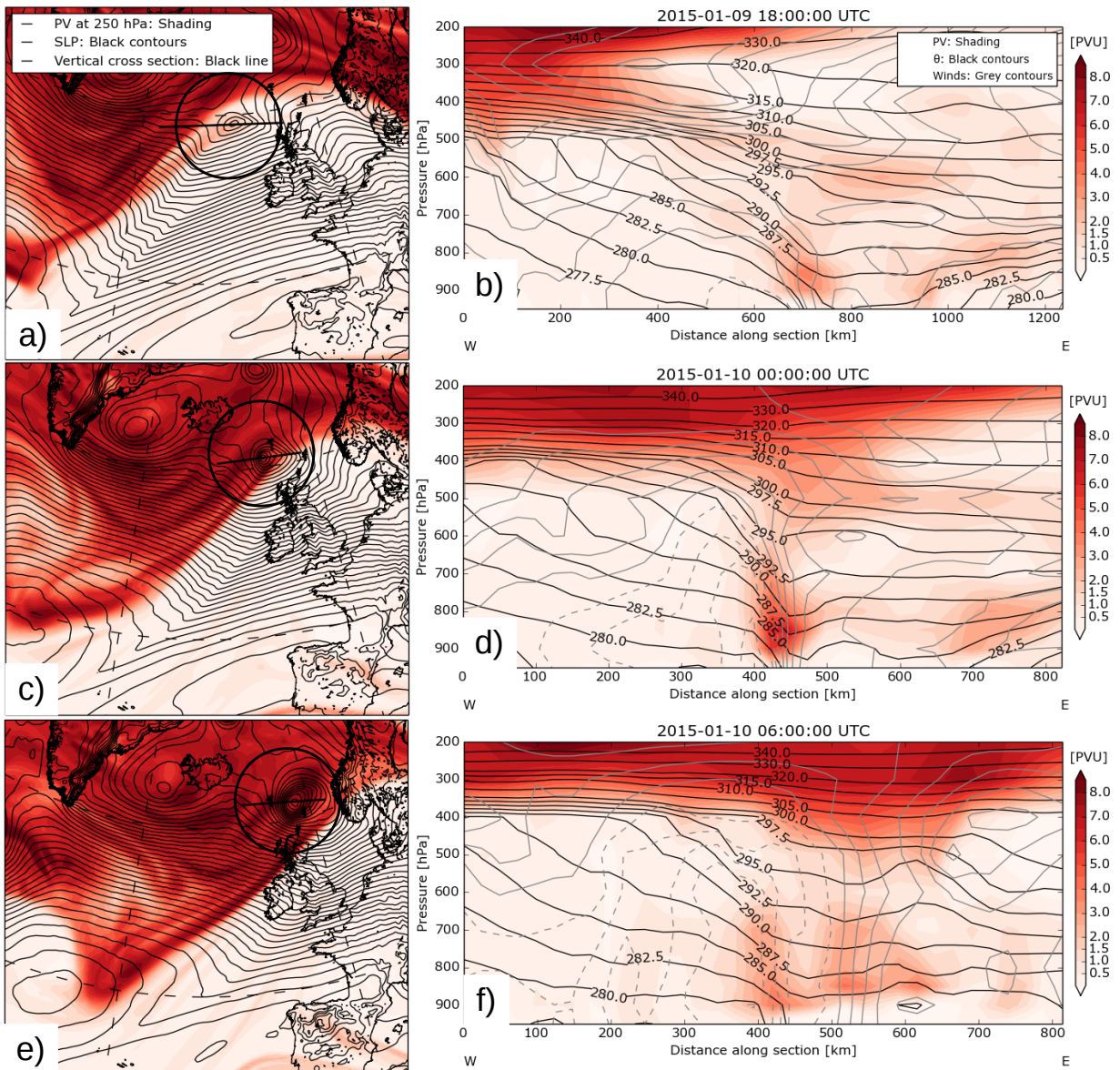
Figure 28: (a),(b): Beginning of the explosive intensification at 18 UTC 9 January, 2015. (c), (d): During explosive intensification at 00 UTC 10 January, 2015. (e), (f): End of the explosive intensifcation at 06 UTC 10 January, 2015. Left: PV at 250 hPa (shading, PVU), sea level pressure (black contours, 2 hPa interval), black line signifies where the vertical cross sections (b, d and f) are taken, black circle indicates the location of Nina. Right: PV (shading, PVU), potential temperature (black contours, 2.5 K interval), total horizontal winds proportional to vertical cross section (grey contours, m/s, dashed out of paper).

4.5   Climatology of Diabatic Rossby Vortexes and a Comparison to Nina

During a 10 year (2001-2010) climatology study of DRV's done by Boettcher and Wernli (2013), 431 tracks of DRV's were found in the North Atlantic (20°N–80°N, 110°W–40°E), most DRV's occurred in the summer months. Out of the 10 years, 54 (12.5%) of the DRV's underwent explosive cyclogenesis. The explosively intensifying DRV's were identified following Sanders and Gyakum (1980) criterion of a SLP deepening of at least 1 hPa in 24 hours over the average latitude of the cyclone during this time, equivalent to 1 Bergeron. Explosive DRV's have the highest frequency in the autumn and winter, associated with enhanced baroclinicity. With a frequency of about five per year from 2001-2010, explosive DRV's are relatively rare cyclones. 10.2 % of all DRV's in the North Atlantic underwent a similar cycle where the intensification phase was triggered by the advancement of a pre-existing upper tropopause fold Boettcher and Wernli (2013).
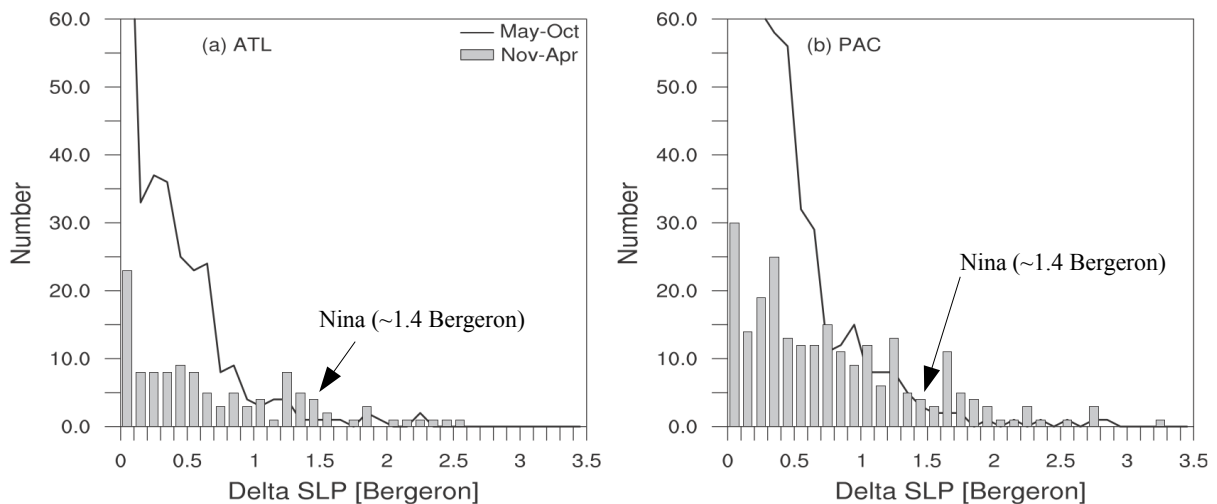
Figure 29: Histogram of DRV intensification (measured in Bergeron, see text for details) for the warm season May–October (black line) and the cold season November–April (gray columns) in the (a) North Atlantic and (b) North Pacific from 2001-2010. Caption and figure is taken from Boettcher and Wernli (2013)

Comparing Nina's Bergeron value of 1.4 with the climatology of DRV intensification in the North Atlantic and North Pacific winter season, it can be seen that the deepening rate can be considered as quite rare (see figure 29). 14.0% of 114 registered DRV's from 2001-2010 in the North Atlantic during the winter months underwent a deepening rate of

60

1.4 Bergeron or higher. While in the North Pacific, 17.6% of 239 registered DRV's from 2001-2010 during the winter months underwent a deepening rate of 1.4 Bergeron or higher. For both basins, 16.4% of 353 registered DRV's from 2001-2010 underwent a deepening rate of equivalent to Nina or higher.

4.6   Decay of Nina

Based on the sea level pressure the decay of Nina began shortly after the minimum SLP of Nina was reached at 10 January 12 UTC 2015, when the cyclone made landfall at the west coast of Norway. On figure 30a, it can seen that the SLP and the geopotential at 700 hPa more or less align and the depth of Nina stretches from the surface to the tropopause (seen by the cyclonic circulation of the wind barbs at tropopause height). This indicates that the cyclone has occluded, and the atmosphere is equivalent barotropic. In an equivalent barotropic atmosphere an extratropical cyclone cannot grow (see section 2.2). Nina moved north after landfall, then remained stationary and decayed on the northwest coast of Norway. By 12 UTC 11 January 2015 Nina undergoing decay. The wind barbs at 850 hPa indicate that there was no clear cyclonic circulation and the SLP has increased from approximately 950 hPa at 12 UTC 10 January 2015 to approximately $\sim$ 988 hPa(see figure 30b).
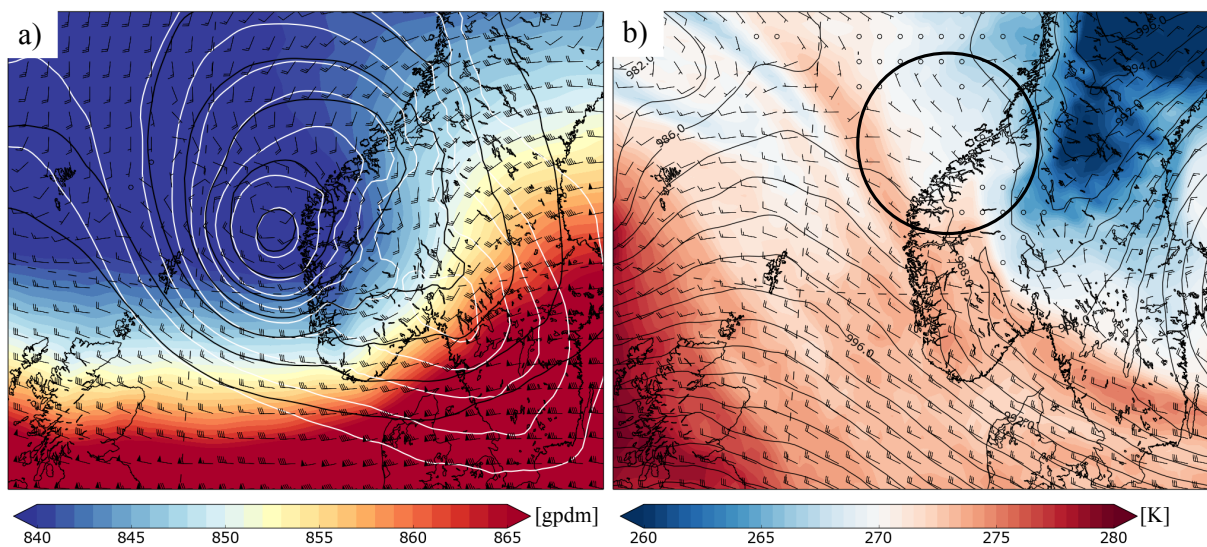

Figure 30: a): Geopotential at 300 hPa (shading), sea level pressure (white contours), geopotential at 700 hPa (black contours) and total horizontal wind (barbs, m/s) at tropopause, at 12 UTC 10 January 2015. b): Equivalent potential temperature (shading, K), SLP (black contours, 2 hPa interval), and total horizontal wind at 850 hPa (barbs, m/s) at 12 UTC 11 January 2015.

5   Sensitivity analysis of Nina

5.1   Kinetic energy sensitivity

We have investigated the KE's sensitivity to specific humidity, potential temperature, zonal wind and meridional wind. A horizontal slice taken at the approximate height of the maximum sensitivities at the final time of the AM model run (00 UTC 9 January, 2015), show that the sensitivities are located north and within the cyclonic structure, and along a frontal structure (seen by the kink in the pressure contours) in the trailing region of Nina (see figure 31 and 32a and b). The different parameter sensitivities are located in approximately the same location, but have significantly different magnitudes. If we look at a vertical cross section, we can see that the sensitivities of largest magnitude are located within the 850-550 hPa layer (see figure 31 and 32c and d).

If we scale the maximum sensitivities with typical values of observational uncertainty, approximately, 1-1.5 gkg^{-1}, 1 K and 1.8 m/s (values obtained from Doyle *et al.* (2013)), we can attain an indication of which parameter the KE is most sensitive to. The KE within the response function box at the initial time of the AM run (12 UTC 10 January 2015), is most sensitive to the specific humidity sensitivity ($[m^2/s^2]/gkg^{-1}$). The specific humidity sensitivity is approximately 2.5-3.5 times larger than potential temperature sensitivity $[m^2/s^2]/K$, 4.5-7 times larger than zonal wind sensitivity ($[m^2/s^2]/ms^{-1}$), and 6-9 times larger than the meridional wind sensitivity ($[m^2/s^2]/ms^{-1}$), respectively. This comparison, and the fact that the sensitivities are located within the 850-550 hPa layer, where moist air reaches saturation, indicate the importance of moisture, diabatic heating and latent heat release at the initial time (00 UTC 9 January 2015) of the NLM run with respect to the strength of the low level KE at landfall of Nina (12 UTC 10 January 2015). We will investigate the sensitivities ahead of Nina because based on the synoptic analysis (see section 4), we suspect that Nina evolved similar to a DRV and the region ahead of a DRV is crucial for its continued cyclogenesis. The large sensitivity to moisture and importance of diabatic and latent heating in relation to Nina is consistent with other studies of extra-tropical cyclones (Doyle *et al.* (2013), Fink *et al.* (2012)).
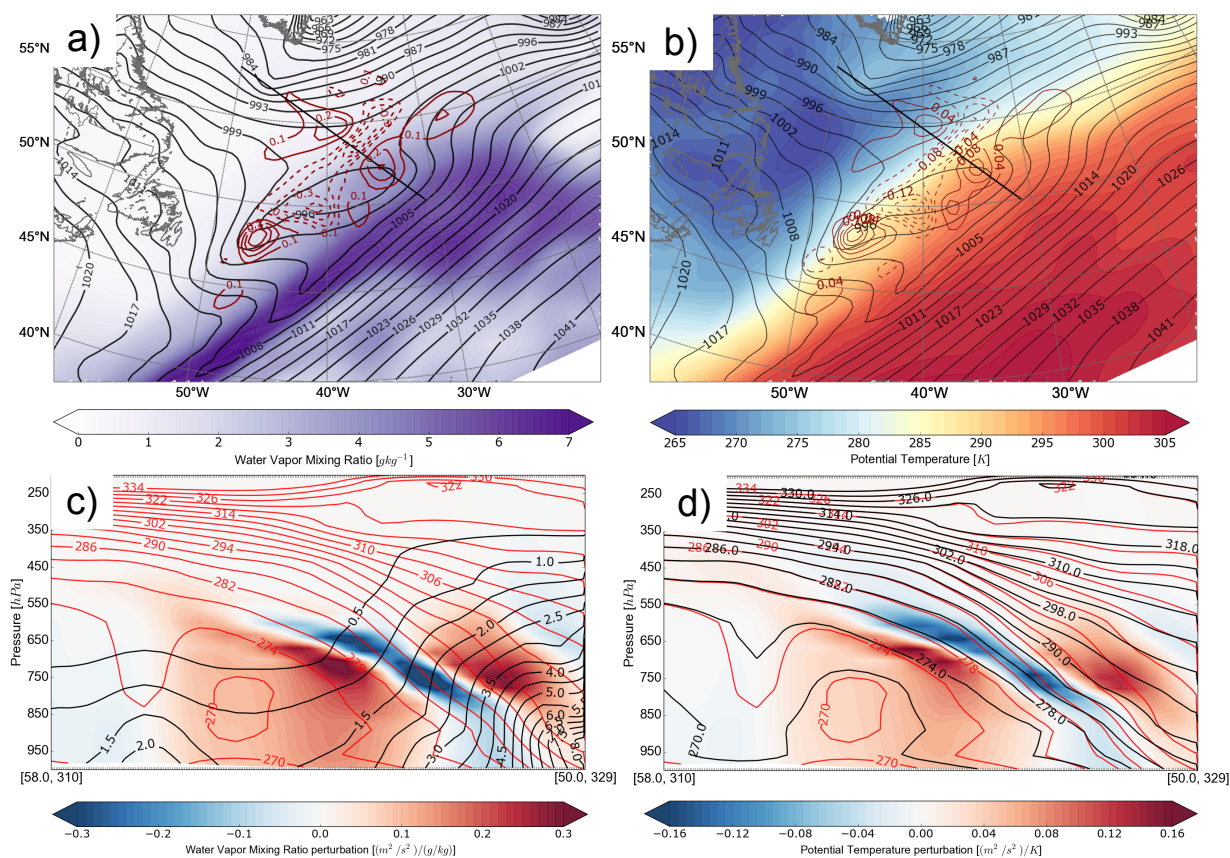
Figure 31: Adjoint sensitivities with KE as a response function for specific humidity and potential temperature. a): Specific humidity sensitivity ($[m^2/s^2]/ms^{-1}$, red contours, dashed negative), specific humidity from nonlinear model (gkg^{-1}, shading) at 750 hPa, and sea level pressure (hPa, black contours) b): Potential temperature sensitivity ($[m^2/s^2]/ms^{-1}$, red contours, dashed negative), potential temperature from nonlinear model (K, shading) at 750 hPa, and sea level pressure (hPa, black contours). c): Vertical cross section (black line in a), specific humidity sensitivity ($[m^2/s^2]/gkg^{-1}$, shading), specific humidity from the nonlinear model (gkg^{-1}, black contours) and moist isentropes from the nonlinear model (K, blue contours) . d): Vertical cross section (black line in b), potential temperature sensitivity ($[m^2/s^2]/K$, shading), potential temperature from nonlinear model (K, black contours) and moist isentropes from the nonlinear model (K, blue contours).

The positive specific humidity and potential temperature sensitivity (figure 31a and b) ahead of the cyclone indicate that an increase of the specific humidity and potential temperature horizontal gradient in the initial forecast fields in the NLM at 750 hPa, will increase the strength of the low level KE at landfall (12 UTC 10 January, 2015). This positive sensitivity could be associated with the fact that Nina evolved similar to a DRV, consistent with the fact that an increase of moisture, should strengthen a DRV. To address

63

this further we have taken vertical cross sections in front of the cyclone (see the lines on figure 31a and b). Because ascending air rises along isentropes (potential temperature contours) when non-saturated and along moist isentropes (equivalent potential temperature contours) when saturated, we have plotted them on the vertical cross sections to see if we can relate the isentrope contours to the sensitivities in the vertical (see figure 31c and d).

The vertical cross section of the specific humidity sensitivity (figure 31c) show that these sensitivities are tilted along the moist isentropes, possibly associated with the front associated with Nina. The sensitivities suggest that an increase of the moisture gradient at approximately 750 hPa will increase the KE at landfall of Nina (12 UTC 10 January, 2015). Though it is difficult to be certain of what the moisture sensitivities actually suggest, we may still present our thoughts regarding this. If we compare the sensitivities from the AM to the moist isentropes from the NLM, we can see that the negative sensitivities are located in the region where the moist isentropic gradient is strongest at 750 hPa. While the positive sensitivities are located relative to the less strong moist isentropic gradients at 750 hPa. If we were to increase the moisture where it is positive and at the same time decrease the moisture where it is negative it seems that the slope of the moist isentropes would become steeper. The steeper moist isentropes would imply an increase of moist ascent which implies more latent heat release and an increase of the positive PV (via $\frac{\delta\theta}{\delta z}$ in equation 32 in section 3.1.1) below the latent heat release. A stronger diabatically produced positive PV, would cause a stronger cyclonic circulation and a stronger storm at landfall (12 UTC 10 January 2015).

The potential temperature sensitivities (see figure 31d) suggest similar interpretation as the moisture sensitivities. The negative potential temperature sensitivity at approximately 750 hPa, is located where the moist isentropic and isentropic gradients are largest, while the positive potential temperature sensitivities, at approximately 750 hPa, are located where the moist isentropic and isentropic gradients are smaller. If we were to increase the NLM potential temperature values where the positive sensitivities from the AM are located and at the same time decrease the NLM potential temperature values where the negative sensitivity from the AM is located, it seems that this would increase the slope of the moist isentropes and the isentropes. A steeper isentropic slope can be linked to enhanced moist ascent, more latent heat release and thus a stronger diabatically produced positive PV anomaly (via $\frac{\delta\theta}{\delta z}$ in equation 32 in section 3.1.1). The stronger positive PV is equivalent to a stronger cyclonic circulation.

We should mention that the positive and negative sensitivities located at a higher altitude (~ 650 hPa), seem to suggest a decrease of the isentropic slope for the moisture sensitivities and the potential temperature sensitivities (see figure 31c and d). This may be associated with the negative PV anomaly also produced by the latent heat release from moisture (via $\frac{\delta\theta}{\delta z}$ in equation 32 in section 3.1.1). A decrease of the slope at 650 hPa would cause the negative PV anomaly (see figure 10, to see how a negative PV anomaly is formed) to be located at larger horizontal distance from the positive PV anomaly located below, and thus the eroding effect of the negative PV anomaly would be decreased.
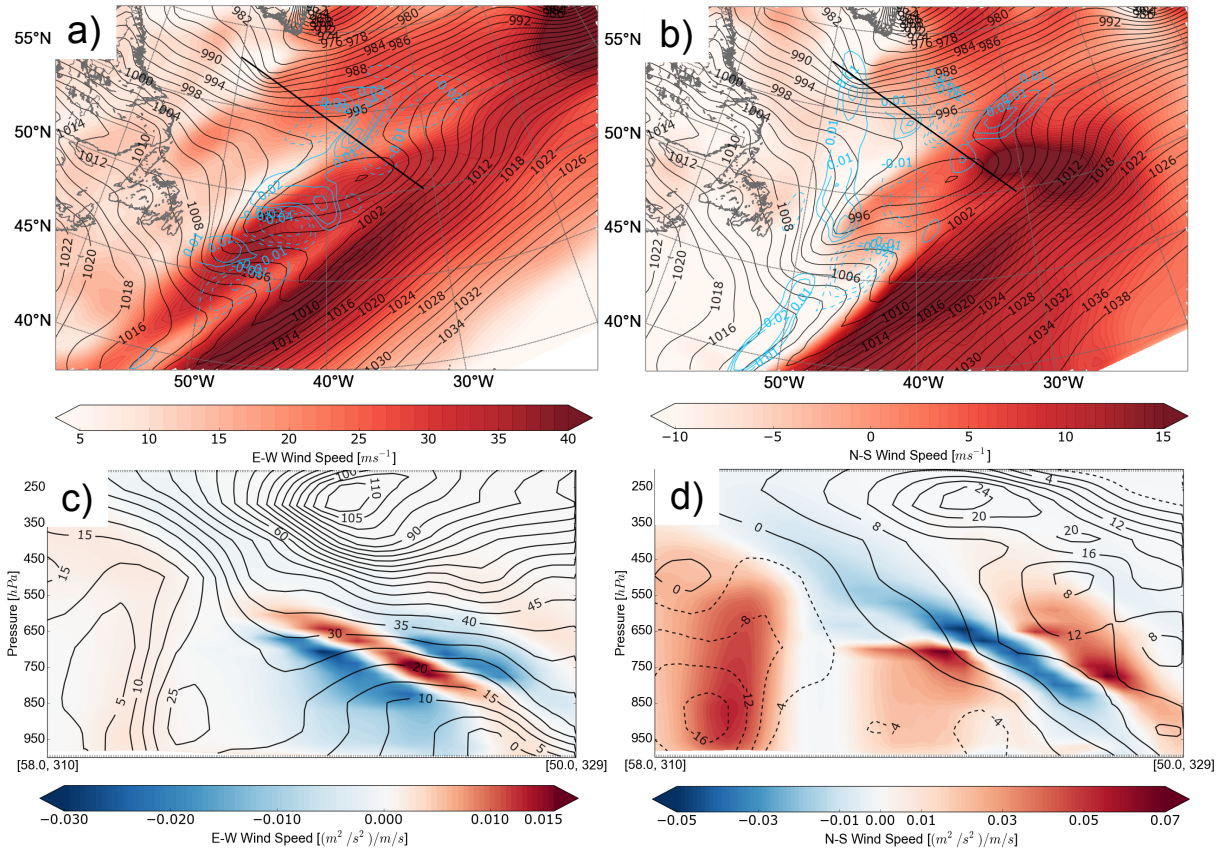
Figure 32: Adjoint sensitivities with KE as a response function for zonal wind and meridional wind. a): Zonal wind sensitivity ($[m^2/s^2]/ms^{-1}$, blue contours, dashed negative), zonal wind from nonlinear model (m/s, shading) at 750 hPa. b): Meridional wind sensitivity ($[m^2/s^2]/ms^{-1}$, blue contours, dashed negative), meridional wind from nonlinear model (m/s, shading) at 700 hPa. c): Vertical cross section (black line in a), zonal wind sensitivity ($[m^2/s^2]/ms^{-1}$, shading) and zonal wind from the nonlinear model (m/s, black contours). d): Meridional wind sensitivity ($[m^2/s^2]/ms^{-1}$, shading) and meridional wind from nonlinear model (m/s, black contours).

When we scaled the different sensitivities in the AM with typical analysis errors, we found that the zonal and meridional wind sensitivities were much smaller than the specific humidity sensitivity. However, by adjusting the zonal and meridional wind in the NLM within the sensitive regions, they could still have an impact on the strength of the storm at the final time (12 UTC 10 January 2015).

The wind sensitivities are very complex and difficult to interpret. We will present our thoughts of how to interpret them. There are many complex sensitivity patterns in the trailing region of Nina for both the zonal and meridional winds. Since Nina evolved similar to a DRV and the forcing regions for a DRV are located ahead of the cyclone, we have decided to focus the zonal and meridional sensitivities located ahead of Nina.

The zonal wind sensitivities (see figure 32a) at 750 hPa suggest that a weaker meridional zonal wind gradient, $\frac{\delta u}{\delta y}$, to the north and within the cyclonic structure, will increase the storms low level KE at landfall (12 UTC 10 January, 2015). If we take a closer look at the zonal sensitivities in the vertical, we can see that the zonal wind sensitivities are located beneath the jet stream and have a tilted structure, possibly associated with the front in relation to Nina (see figure 32c). The positive and negative zonal sensitivities seem to suggest that a stronger and more confined zonal wind at 750 hPa will increase the low level KE at landfall. This could possibly be linked to a stronger incipient cyclonic circulation at the initial NLM forecast field (00 UTC 9 January 2015).

The meridional wind sensitivity at 700 hPa suggest that a weaker northerly flow to the west of the cyclone will enhance low level KE at landfall (the elongated positive sensitivity on figure 32b). If we look at the meridional sensitivities in the vertical they show the same tilted structure which may be linked to a front in association with Nina (see figure 32d). The meridional sensitivities are negatively correlated with the zonal wind sensitivity and they are also located beneath the jet stream. In addition, there seems to be a low level jet located on the northern edge of the cross section (close to 58° latitude). The sensitivities suggest that a weakening of this low level jet would cause stronger KE at landfall of Nina. The positive and negative meridional sensitivities at the most southern edge of the cross section (close to 50° latitude) seem to suggest a more confined southerly flow at approximately 750 hPa will increase the low level KE at landfall. This could be linked to a suggestion of a stronger incipient cyclonic circulation in the intial NLM forecast field (00 UTC 9 January 2015).

Though the sensitivities ahead of Nina were important, they were not the largest sensitivities with respect to moisture, potential temperature and the zonal and meridional

winds. The largest moisture and potential temperature sensitivities are located on and in the ambient region of the frontal structure behind Nina. In this study we have decided to focus on the most significant positive sensitivity anomaly with respect to moisture because Nina was highly sensitive to this parameter. The positive moisture sensitivity is located on the frontal structure behind Nina (see figure 31a).
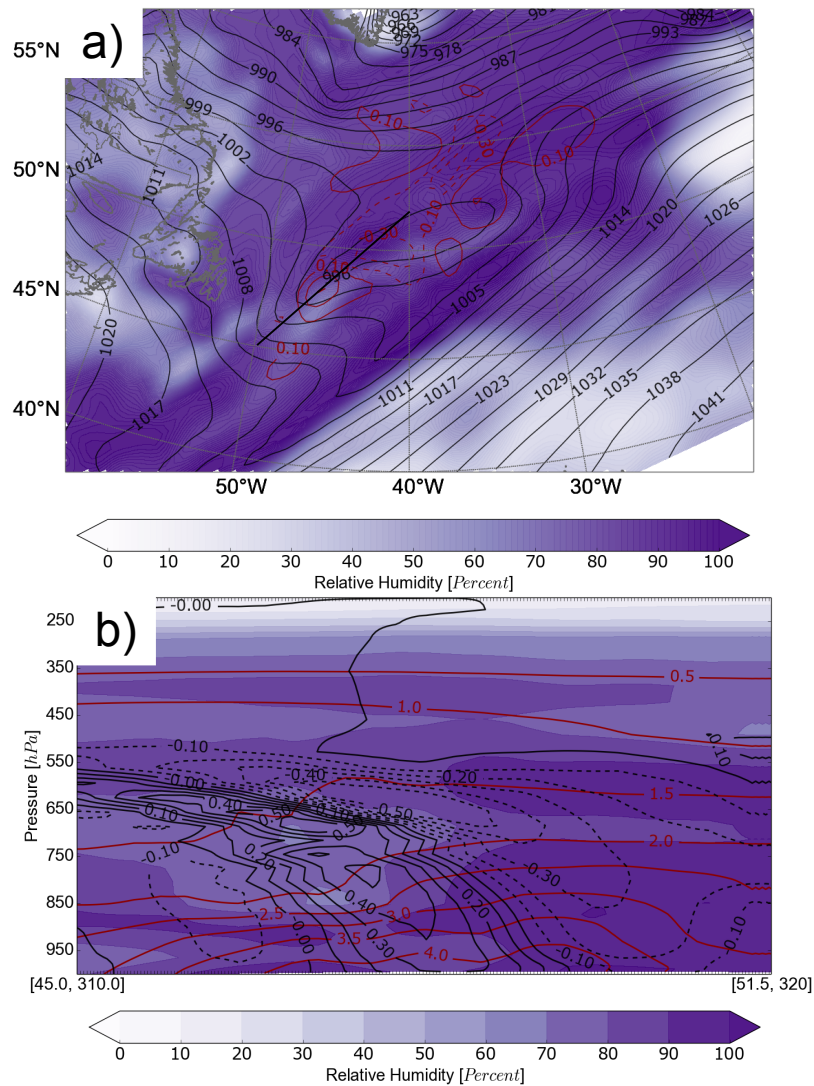
Figure 33: a): Relative humidity (%, shading), specific humidity sensitivity ([m^2/s^2]/gkg^{-1}, red contours, dashed negative) at 750 hPa and sea level pressure (hPa, black contours) at 00 UTC 9 January, 2015. Black line is the vertical cross section shown in b. b): Relative humidity (%, shading), and specific humidity sensitivity ([m^2/s^2]/gkg^{-1}, black contours). Data from the COAMPS models.

To address the largest positive moisture sensitivitiy, we plotted the relative humidity from the nonlinear model and the specific humidity sensitivity at 750 hPa, at the final time of the AM run (00 UTC 9 January, 2015)(see figure 33a). The figure shows that the maximum positive moisture sensitivity is co-located with a local region of small relative humidity (30-60%). The vertical cross section shows the local region of smaller relative humidity more clearly (figure 33b). We can see that there is a deep pocket of lower relative humidity located at approximately 850-600 hPa and that the largest positive sensitivities are located within this drier pocket (see moisture contours on figure 33b). The positive moisture sensitivity suggest that an increase of moisture within this dry pocket will increase the low level KE at landfall. An increase of moisture in this region would make the air closer to saturation (i.e larger relative humidity). The fact that the largest positive moisture sensitivity is located here, may be another indication of the importance of diabatic heating from latent heat release with respect to Nina.

In the synoptic analysis of Nina (see section 4), we showed that Nina evolved similar to a DRV (see section 3.1.2, for explanation of the DRV concept). The sensitivity analysis with KE in the lowest 1 km at landfall of Nina (12 UTC 10 January 2015) as a response function seem to support our statement that Nina evolved similar to a DRV, for the following reasons:

- When we scaled the sensitivities with typical analysis errors of size ~ 1, we found that Nina was much more sensitive to moisture compared to the other sensitivities (2.5-9 times larger) and moisture is a fundamental ingredient for DRV cyclogenesis.

- The sensitivities ahead of the cyclone are located within the 850-550 hPa layer indicating the importance of diabatic heating and latent heat release associated with Nina.

- The moisture and potential temperature sensitivities seem to be positioned in regions that would favor an increase of the isentropic slope, which could be linked to increased moist ascent, more latent heat release and a stronger diabatically produced PV anomaly (via $\frac{\delta\theta}{\delta z}$ in equation 32 in section 3.1.1). The increased positive PV anomaly would then cause a stronger incipient cyclonic circulation at 00 UTC 9 January 2015 and increase the low level KE at landfall (12 UTC 10 January, 2015)

- The sensitivity of largest magnitude is the moisture sensitivity. This moisture sensitivity is located within region of lower relative humidity compared to the rest of

the region. The large moisture sensitivity to drier air emphasises the importance of diabatic heating with respect to this storm.

By choosing KE as a response function, we achieved an indication of which parameters the low level KE at landfall (12 UTC 10 January, 2015) of Nina were most sensitive to. We also achieved an indication of where the largest AM sensitivities were located at the initial time (00 UTC 9 January, 2015) of the nonlinear forecast of Nina. From the sensitivity analysis with KE as a response function, we have learned how we can adjust the parameters in the NLM forecast at 00 UTC 9 January 2015 within the sensitivite regions indicated by the AM so that we can achieve stronger low level KE (i.e stronger low level winds).

5.2   Optimal perturbations with respect to kinetic energy

The optimal perturbations using KE as the response function were calculated following section 2.3.2. The optimal perturbations should maximize the KE below 1km altitude in the three dimensional response function box at the final integration time (12 UTC 10 January 2015). We can see that the sensitive regions in the initial fields have a significant impact on the evolution of the maximum winds with respect to the storm (see figure 34 below). With the optimal perturbations added to the nonlinear forecast field, we can see that the winds have a maximum increase south the Faroe Islands with a magnitude increase of about ∼ 10 m/s (compare figure 34a and b). The increase outside the box is expected because it would be unrealistic if the model adjusted the wind speed inside the box only. Inside the response function box we can see an increase of the winds in the part of the box that is located over the ocean. The maximum increase is located at the western edge of the box with a magnitude of approximately 5 m/s. If we look at the vertical cross sections (figure 34c and d, black lines on a and d), we can clearly see how the wind has increased significantly.

The maximum winds in the nonlinear model within the response function box is approximately ∼ 32 m/s located at 800-1000 meters, while the maximum winds in the nonlinear model run with the optimal perturbations is about > 36 m/s located at 900-1000 meters. However, it is the low levels that are of interest to us. From 0-100 meters the wind field with the optimal perturbations is much stronger compared to the unperturbed nonlinear forecast (compare figure 34c and d). The maximum winds reach ∼ 26-27 m/s in the nonlinear model run without the optimal perturbations. When we include the optimal perturbations we can see that the low level winds reach a maximum of about ∼ 33 m/s.

69
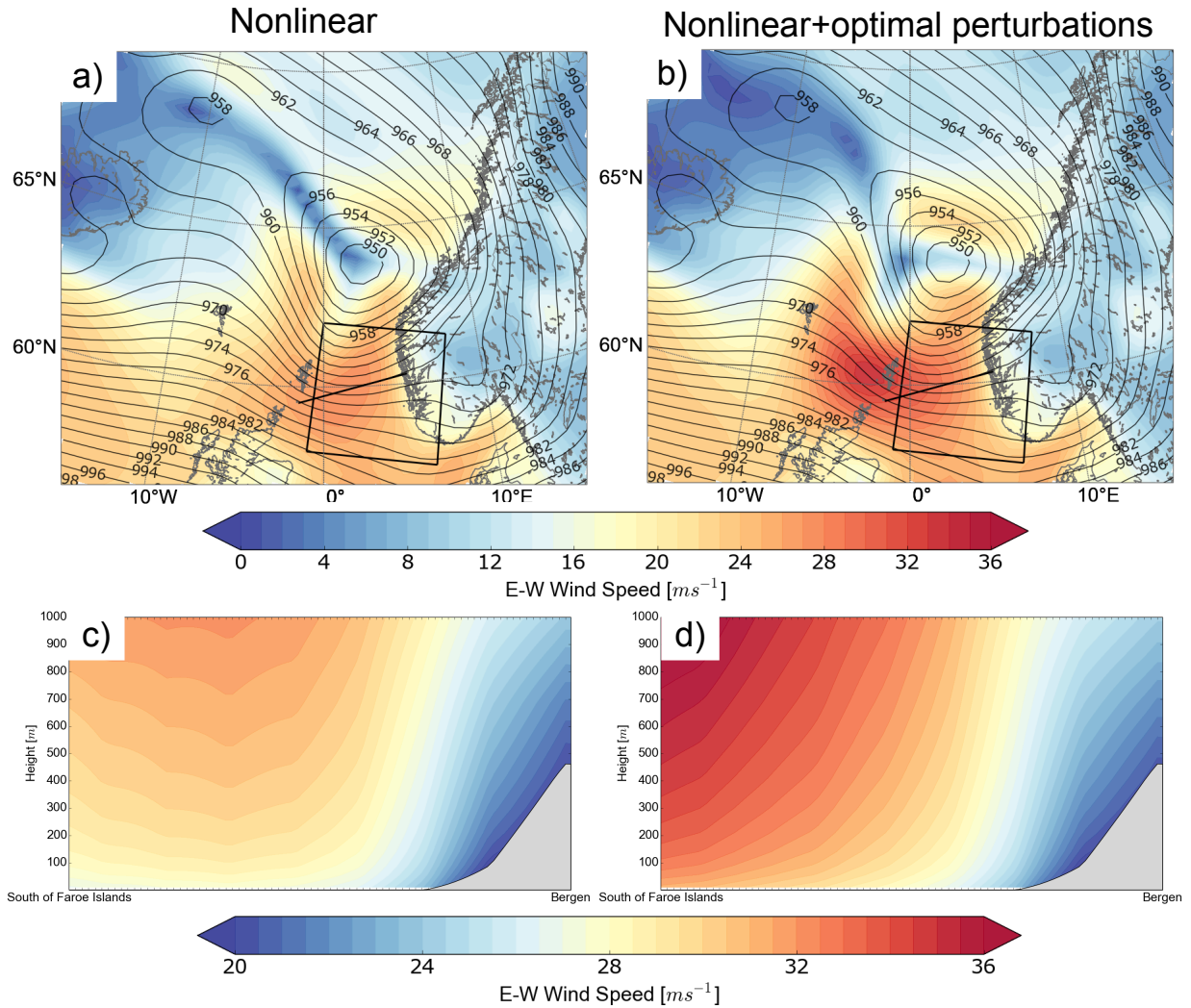
Figure 34: a): 10 meter total horizontal wind (m/s, shading), mean SLP (black contours, 2hPa interval). b): 10 meter total horizontal wind from the nonlinear model with the optimal perturbations (m/s, shading), mean SLP from the nonlinear model (black contours, 2 hPa interval). The black box is the approximate position of the response function box for KE. The black line is the location of the cross sections. c, d): Cross sections from surface to top of response function box (0-1000 meters), from the nonlinear model and the nonlinear model with the optimal perturbations, respectively.

5.3   Potential vorticity sensitivity

Figure 35: Adjoint sensitivities with PV as a response function for specific humidity and potential temperature. a): Specific humidity 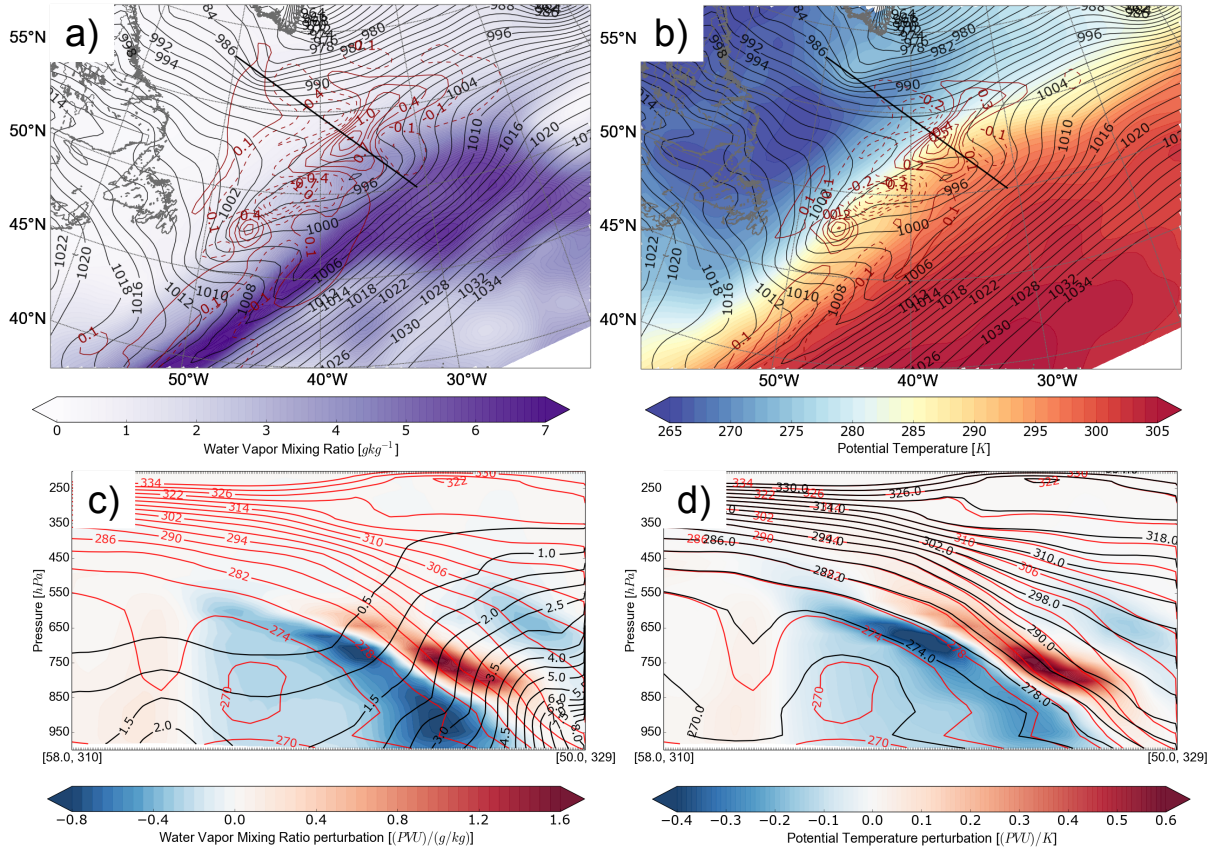sensitivity ([PVU]/gkg^{-1}, red contours, dashed negative), specific humidity from nonlinear model (gkg^{-1}, shading) at 750 hPa, and sea level pressure (hPa, black contours) b): Potential temperature sensitivity ([PVU]/K, red contours, dashed negative), potential temperature from nonlinear model (K, shading) at 750 hPa, and sea level pressure (hPa, black contours). c): Vertical cross section (black line in a), specific humidity sensitivity ([PVU]/gkg^{-1}, shading) and specific humidity from the nonlinear model (gkg^{-1}, black contours). d): Vertical cross section (black line in b), potential temperature sensitivity ([PVU]/K, shading) and potential temperature from nonlinear model (K, black contours).

The sensitivity analysis with KE as the response function gave us an indication of the forcing mechanisms that affect the strength of the low level KE at landfall of Nina. However, the largest complication when forecasting Nina was its track (see section 1.1, for details). To address the track with respect to the dynamics, we chose PV at mid-levels (800-600 hPa altitude) as a response function and investigated the PV's sensitivity at three hours before landfall (09 UTC 9 January 2015) with respect to specific humidity, potential

temperature, zonal wind and meridional wind (see section 3.2.2, for explanation of our choice of response function). The PV sensitivities are, like the KE sensitivities, located north and within the cyclonic structure and along frontal structure (seen by the kink in the pressure contours) in the trailing region of Nina. However, the horizontal extension of the PV sensitivities is much larger (compare for instance figure 31a and b and 35a and b). The increased horizontal extension is expected, because PV depends on a higher number of individual variables than KE. The maximum sensitivities have a larger vertical extension compared to the KE sensitivities, they are located within the 950-550 hPa layer (compare figure 35 and 36c and d). Scaling these sensitivities with the same observational uncertainty as with the KE sensitivities (approximately 1-1.5 gkg^{-1}, 1 K and 1.8 ms^{-1}, from Doyle *et al.* (2013)) shows that the PV within the response function box at 09 UTC 10 January 2015 (see figure 38 in section 3.2.2, for location of the box) is most sensitive to the specific humidity sensitivity ([PVU]/gkg^{-1}) with respect to the final field of the AM run (00 UTC 9 January 2015). The specific humidity sensitivity is approximately 2-3 times larger than the potential temperature sensitivity ([PVU]/K), 4-6.5 times larger than the zonal wind sensitivity ([PVU]/ms^{-1}), and 6-9 times larger than the meridional wind sensitivity, respectively. As expected, the PV has the largest sensitivity to moisture and potential temperature. This indicates, similar to the results using KE as a response function, that diabatic heating was important with respect to this storm. The sensitivities with respect to PV are very complex and it is difficult to relate all the sensitivities to the dynamics of the storm. We will follow the KE sensitivity analysis and focus on the sensitivities ahead of Nina. In addition to this we will also investigate the largest positive sensitivity with respect to PV.

The PV's sensitivity three hours before landfall (00 UTC 9 January 2015) to specific humidity and potential temperature at 00 UTC 9 January 2015, suggest that an increase of the specific humidity and potential temperature gradient ahead and north of Nina, will increase the PV three hours before landfall (35a and b). A closer look at a vertical cross section of the moisture sensitivities ahead of Nina, shows that the maximum sensitivities are located at about 750 hPa at the approximate height of condensation (see figure 35c). The positive moisture sensitivity is co-located with the strongest nonlinear moist isentropic gradient at the same height. While the maximum negative moisture sensitivities are located at approximately 700 hPa and 900 hPa in a region of smaller nonlinear moist isentropic gradient. More moisture at 750 hPa could cause more latent heat release and a stronger positive PV anomaly (via $\frac{\delta\theta}{\delta z}$ in equation 32 in section 3.1.1), hence a stronger

incipient cyclonic circulation at 00 UTC 9 January 2015. The positive and negative PV sensitivities at 750-650 hPa suggest that a sharper moisture gradient at this altitude, will increase the PV at three hours before landfall. The increased moisture gradient may be associated with a stronger front (see section 8 and equation 6, for details on how a front can intensify). We can see that the moist sensitivity also suggest that less moisture at 900 hPa will cause a stronger storm at three hours before landfall.

The positive and negative potential temperature sensitivity suggest that a stronger isentropic gradient at 800-650 hPa will cause a stronger PV at three hours before landfall. This can again be interpreted as the sensitivities suggesting that a more intense front will cause a stronger storm at the 09 UTC 10 January 2015. A stronger front could be linked to more moist ascent and a stronger cyclonic circulation via the stronger diabatically produced PV anomaly.   A horizontal slice of the zonal and meridional wind sensitivities at 950 hPa and 700 hPa, respectively, indicates that the sensitivities are located in the vicinity of Nina and along the frontal structure in the trailing region of Nina (see figure 36a and b). We took a horizontal slice of the zonal wind at 950 hPa in this case because we noticed the large horizontal extension of the sensitivity at this level.

The horizontal zonal wind sensitivity at 950 hPa suggest that an increase of the low level nonlinear zonal winds ahead and a decrease of the southerly flow behind Nina will increase the PV at three hours before landfall (see figure 36a). This may be linked to a suggestion of a stronger incipient cyclonic circulation at low levels at the initial time. A closer look at the vertical structure of the zonal wind sensitivities ahead of Nina shows that stronger winds at 950 hPa and weaker winds at 750 hPa would cause a stronger PV at the final time (see figure 36c).

The horizontal meridional wind sensitivitiy at 700 hPa suggest that an increased southerly flow ahead of Nina and an increased northerly flow behind Nina will increase the PV at three hours before landfall (see figure 36b). This may be interpreted in the same way as the horizontal zonal wind sensitivities as a suggestion of a stronger incipient cyclonic circulation. The maximum vertical meridional winds sensitivities ahead of Nina are confined to the 850-650 hPa altitude. The vertical meridional wind sensitivities suggest that an increased meridional wind gradient at at approximately 750 hPa would cause a stronger storm at the final time (see figure 36d).
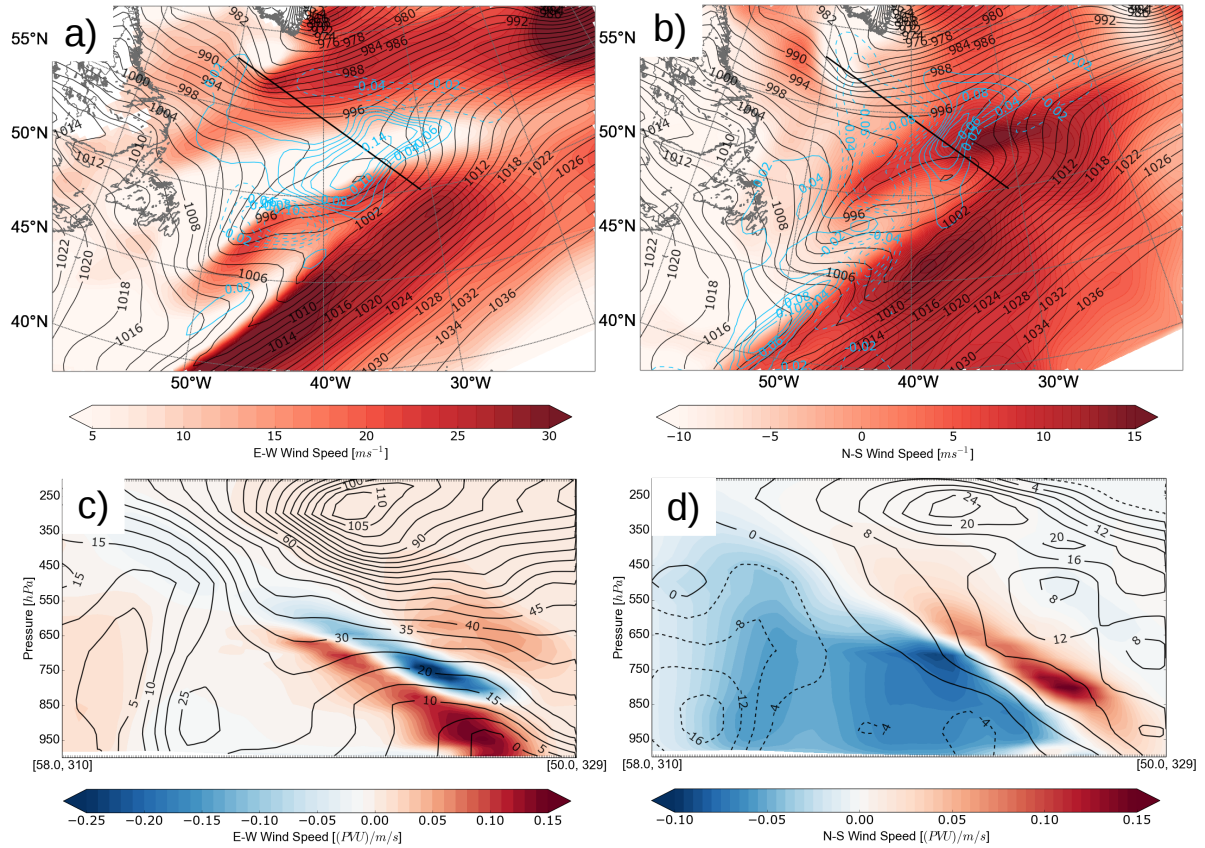
73

Figure 36: Adjoint sensitivities with PV as a response function for zonal wind and meridional wind. a): Zonal wind sensitivity ([PVU]/ms^{-1},blue contours, dashed negative), zonal wind from nonlinear model (ms^{-1}, shading) at 950 hPa. b): Meridional wind sensitivity ([PVU]/ms^{-1}, blue contours), meridional wind from nonlinear model (ms^{-1}, shading) at 700 hPa. c) Vertical cross section (black line in a), zonal wind sensitivity ([PVU]/ms^{-1}, shading) and zonal wind from the nonlinear model (ms^{-1}, black contours). d): Meridional wind sensitivity ([PVU]/ms^{-1}, shading) and meridional wind from nonlinear model (ms^{-1}, black contours).

In the KE sensitivity analysis, we investigated the cause of Nina's largest positive moisture sensitivity anomaly located on the frontal structure behind Nina (see section 5.1 and figure 33). The PV at three hours before landfall also exhibits a large positive moisture sensitivity to the same local area on the frontal structure behind Nina (compare figure 37a and 33a). We can see that the largest positive moisture sensitivity to PV at three hours before landfall is also located within the pocket of low relative humidity (30-60%) at approximately 850-600 hPa (see figure 37b). The positive moisture sensitivity suggest that if we increase the moisture within the dry pocket in the initial field we would achieve a stronger positive PV, and thus a stronger storm at the 09 UTC 10 January 2015. However,

the moisture sensitivities also suggest a decrease of moisture content in the NLM above and to the east of the positive moisture sensitivity would cause a stronger PV at the final time. This could be linked to the fact that a more evenly distributed nonlinear moisture field with large relative humidity at the low levels that gradually decreases with altitude, would cause an ideal set up causing more latent heat release at the same height and thus a stronger diabatically produced positive PV.
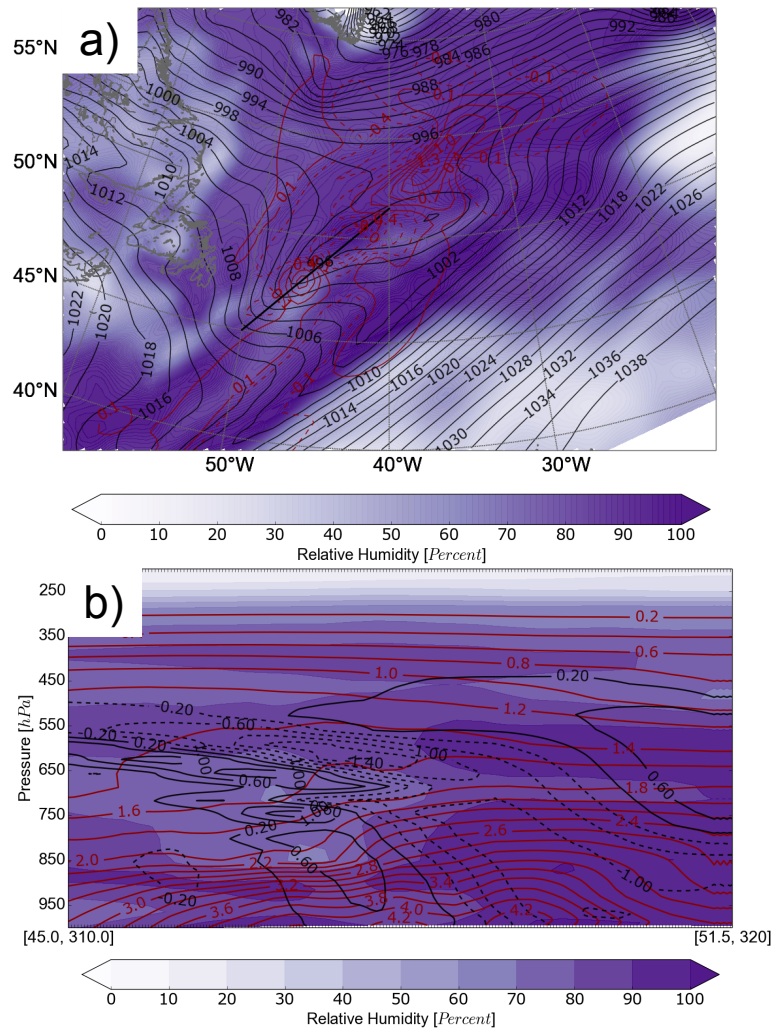

Figure 37: a): Relative humidity (%, shading), specific humidity sensitivity ([PVU]/gkg^{-1}, red contours, dashed negative) at 750 hPa and sea level pressure (hPa, black contours) at 00 UTC 9 January 2015. Black line is the vertical cross section shown in b. b): Relative humidity (%, shading), and specific humidity sensitivity ([PVU]/gkg^{-1}, black contours).

75

The sensitivities at the initial time (00 UTC 9 January, 2015) with respect to the PV at approximately 600-800 hPa three hours before landfall (09 UTC 10 January, 2015) agrees with our statement that Nina evolved similar to a DRV for the following reasons:

- When we scaled the sensitivities with typical analysis errors of size ~ 1, we found that Nina was much more sensitive to moisture compared to the other sensitivities with respect to the PV (2-9 times larger). This is in agreement with the KE sensitivity analysis and underscores the strong connection to the diabatic heating component.

- The largest sensitivities ahead of the cyclone are located within the 550-1000 hPa layer within the condensational layer, but also expanding beyond the typical layer of condensation. This may be due to the fact that the PV has a higher number of individual variables (compare equation 30 and equation 33).

- The moisture and potential temperature sensitivities favors an increase of the non-linear moisture gradient and potential temperature gradient, which could be linked to a suggestion of a stronger front in association with Nina. A stronger front could cause increased moist ascent, which can be linked to an increased incipient cyclonic circulation via the positive PV produced by the latent heat release. There are strong moisture and potential temperature sensitivities located within the forcing regions of a DRV. There is a large positive moisture sensitivity to a dry pocket in the initial nonlinaer model field located on a frontal structure behind Nina. This underscores, yet again, the importance of diabatic heating and latent heating with respect to Nina.

The PV sensitivities show similar patterns as the KE sensitivities, as expected. The PV and KE sensitivity analyses agree with our statement that Nina evolved similar to a DRV. However, our main goal with the PV sensitivities was to see if we could relate the track of Nina to the dynamics of Nina. We wanted to see if we could optimally perturb the initial NLM field so that Nina would evolve further south at landfall.

5.4   Optimal perturbations with respect to potential vorticity

The optimal perturbations with PV as the response function were calculated following section 2.3.2. We wanted maximum PV within the response function box, so we calculated the optimal perturbations that would give maximum PV in the box. On figure 38, we can see that the unperturbed nonlinear forecast (black contours) is further north compared to the optimally perturbed nonlinear model forecast (red contours). If we compare figure 38

and 39, we can see that we successfully managed to perturb the initial NLM field so that the cyclone center evolved further south, closer to the proposed position by the analysis data. We compared the COAMPS forecast output with the ECMWF IFS output because the analysis fields were not available from the COAMPS model. We do realize that it may be difficult to compare output data from two different models. However, since the COAMPS model and the ECMWF IFS are both atmospheric models, they should be equal to such an extent that they can be comparable. Figure 38 shows that we successfully managed to perturb the initial NLM field so that Nina chose a more southern track. We were successful in showing that small perturbations of the NLM field within the sensitivite locations can change the track of Nina at three hours before landfall.
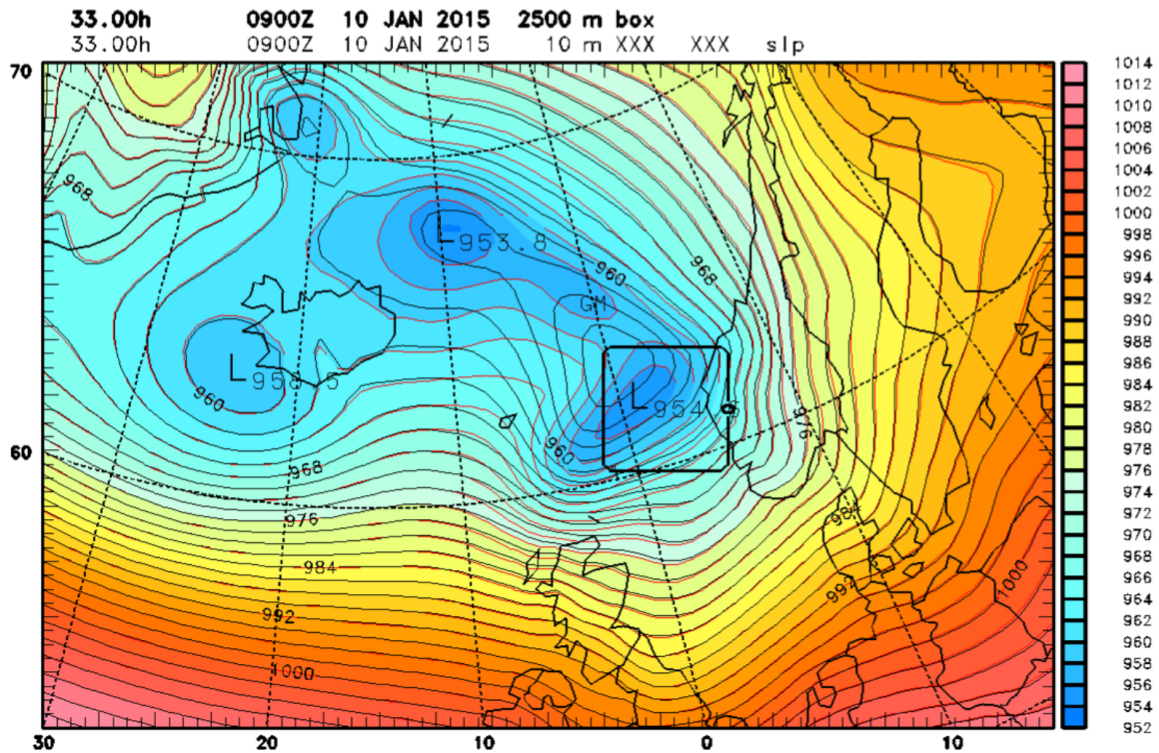
Figure 38: Nonlinear COAMPS forecast (black contours, 2 hPa interval). Nonlinear COAMPS forecast + optimal pressure perturbations evolved in the nonlinear COAMPS model (red contours, 2 hPa interval). Intitialized at 00 UTC 9 January 2015. Integration length of forecast: 33 hours, from 00 UTC 9 January 2015 to 09 UTC 10 January 2015. The black box show the position of the three dimensional PV response function box located at approximately 600-800 hPa altitude. Figure made by Prof. Dr. James Doyle.

Figure 39: Mean SLP at 12 UTC 10 January 2015 (black contours and shading, 2 hPa interval), analysis fields from the ECMWF IFS. The position of Nina has been marked with a red circle.

6 Summary and Conclusion

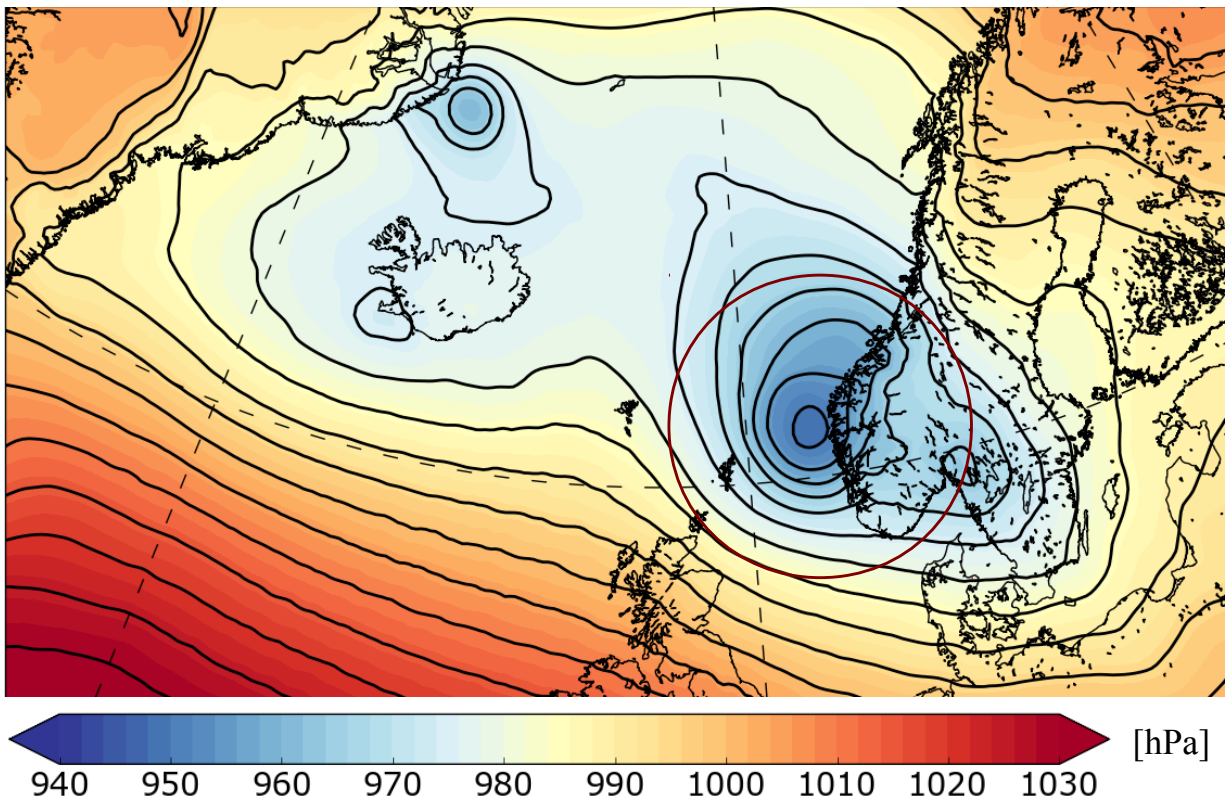Nina was an extratropical cyclone that formed at the east coast of Nova Scotia and New Foundland, 18 UTC 7 January 2015. After genesis the system propagated across the North Atlantic ocean, evolved into an extreme extratropical cyclone and struck the western coast of Norway at 12 UTC 10 January 2015 (see figure 4, for the track of Nina). The storm caused significant damage to property at the Norwegian west coast due to the extreme surface wind that came with this storm. The estimated economical impact after the storm was about ~ 450 million NOK. Since Europe is situated at the termination of the North Atlantic storm track which is linked to the average position of the jet stream (see figure 1b), this part of the world has a history of extreme extratropical cyclones that cause a lot of destruction (see section 1.3, for examples). As long as the North Atlantic storm track does not change, Europe will keep receiving destructive extratropical cyclones. Due to this fact it is important to investigate how these extreme systems evolve and to learn what causes them to evolve into extreme systems. By performing a synoptic analysis we learned how Nina evolved and that the cyclone can be classified as a DRV (section 4). We also performed a sensitivity analysis (section 5) to learn how KE and PV at landfall (12 UTC 10 January 2015) and three hours before landfall (9 UTC 10 January 2015) of Nina, respectively, is sensitive with respect to the nonlinear specific humidity, potential temperature, meridional and zonal wind fields at our chosen initial time, 00 UTC 9 January 2015. The sensitivity analysis strengthened the result of our synoptic analysis because the sensitivities were large in forcing regions of a DRV and the cyclone was highly sensitive to moisture.

When we performed the synoptic analysis we followed a method by Boettcher and Wernli (2013), which involved investigating if the synoptic environment of Nina was similar to typical synoptic environments that favor formation of DRV's (see section 3.1 for the method, and figure 13 for the respective synoptic environments). We found that the synoptic environment of Nina was strikingly similar to scenario C in figure 13 (see figure 23) and that the synoptic environment contained strong low level baroclinicity, high moisture content and an upstream upper level trough. These conditions pointed towards the possibility that Nina may have evolved similar to a DRV. Thus, we continued our investigation by checking if each timestep (available at 00, 06, 12, 18 UTC) from 18 UTC 7 January to 12 UTC 9 January contained a SLP minimum associated with Nina (1.), a co-located PV anomaly at 850 hPa (2.) above the threshold of 0.8 PVU. Then we checked if the

atmosphere featured low level baroclincity (3.) and moisture content (4.) above 5K and 90%, respectively, at the timesteps 00, 06 and 12 UTC 9 January 2015. In addition we checked if Nina propagated at a speed above 11.6 m/s (5.) from 18 UTC 8 January 2015 - 12 UTC 9 January 2015. Finally, we checked the influence of the upstream upper level trough by checking if the average PV at 250 hPa above Nina was below 1.0 PVU and if the trough was stationary (6.). Since these six criteria, defined by Boettcher and Wernli (2013), were fulfilled we could label Nina as evolving similar to a DRV.

Based on the SLP we found that Nina could be labeled as a 'bomb' cyclone during its intensification phase (12 UTC 9 January 2015 - 12 UTC 10 January 2015). Thus, we continued our investigation to see if we could also label Nina as an explosive DRV. Boettcher and Wernli (2013) made composites that showed how DRV's from 2001-2010 typically underwent explosive cyclogenesis (see section 3.1.3 and figure 15 and 16). We compared the composites of explosive DRV's by Boettcher and Wernli (2013) with Nina's intensification phase and we found the comparison to be strikingly similar (see figure 27 and 28 in section section 4.4). The upstream upper level trough overtook the low level cyclone, which lead to the formation of a PV-tower and an extreme deepening of the cyclone. Because of the striking similarities, we believe that Nina also underwent cyclogenesis as an explosive DRV. We found that out of all registered DRV's in the climatology of DRV's done by Boettcher and Wernli (2013) from 2001-2010 in the North Pacific and North Atlantic, only 16.4% of them underwent an intensification phase equal to or more extreme than Nina (see figure 29 in section 4.5).

When we performed the sensitivitiy analysis we first investigated if the output of the AM model can be considered useful by evolving the zonal wind optimal perturbations in the TLM and the NLM, and we calculated the correlations between the TLM and NLM within the KE and PV response function box (see table 1 and figure 19 and 20 in section 3.2.6). We found the evolved zonal wind optimal perturbations to be similar and we found the correlations to be of a satisfactory positive magnitude. Thus, we concluded that the AM model is able to calculate sensitivities that can be related to the actual dynamics of Nina. We chose KE and PV as response functions, because with these functions we could learn which regions in the initial NLM field (00 UTC 9 January 2015) can be perturbed to cause a stronger storm and a changed track of Nina at landfall (12 UTC 10 January 2015 and 09 UTC 10 January 2015, respectively). We first investigated Nina's landfall KE sensitivity (from the surface to 1 km altitude) to initial nonlinear specific humidity, potential temperature and zonal and meridional wind at 00 UTC 9 January 2015 (see section 5.1). Then we investigated Nina's PV sensitivity (at approximately 600-800 hPa altitude) to the

same parameters and same initial time as the KE sensitivities (see section 5.3). The final time was in this case set to 09 UTC 10 January 2015 (i.e three hours before landfall).

We found that the low level KE at landfall was highly sensitive to moisture. The moisture sensitivities ($[m^2/s^2]/gkg^{-1}$) were about 2.5-3.5 times larger than the potential temperature sensitivity ($[m^2/s^2]/K$), 4.5-7 times larger than the zonal wind sensitivity ($[m^2/s^2]/ms^{-1}$), and 6-9 times larger than the meridional wind sensitivity ($[m^2/s^2]/ms^{-1}$), respectively. This comparison, and the fact that the sensitivities were located within the 850-550 hPa layer, where moist air reaches saturation, indicated the importance of moisture and latent heat release in with respect to the strength of the low level KE at landfall of Nina. Because we concluded that Nina evolved similar to a DRV in the synoptic analysis, we focused on the KE sensitivities located ahead of Nina. We took vertical cross sections in the region ahead of Nina and our interpretation of the moisture and potential temperature sensitivities (see figure 31) was that they suggested that the front associated with Nina should become stronger. The stronger front would cause stronger low level KE at landfall of Nina. The stronger front could be linked to enhanced moist ascent, more latent heat release, a stronger positive PV anomaly and thus enhanced incipient cyclonic circulation at 00 UTC 9 January 2015. Our interpretation of the zonal and meridional wind sensitivities (figure 32) was that they suggested that an enhanced incipient cyclonic circulation would cause the KE at landfall to become stronger. When we added the evolved zonal wind optimal perturbations to the nonlinear forecast at 12 UTC 10 January (see figure 34), we found that the maximum surface winds increased from ~ 28 m/s to ~ 33 m/s, an increase of ~ 5 m/s.

The mid-level PV sensitivities were highly sensitive to moisture, in agreement with the KE sensitivities. The moisture sensitivities ($[PVU]/gkg^{-1}$) were about 2-3.5 times larger than the potential temperature sensitivity $[PVU]/K$, 4.5-7 times larger than the zonal wind sensitivity ($[PVU]/ms^{-1}$), and 6-9 times larger than the meridional wind sensitivity ($[PVU]/ms^{-1}$), respectively. The PV sensitivities were located more or less in the same regions as the KE sensitivities, however the PV sensitivities had a larger horizontal and vertical extension. In the vertical the PV sensitivities were also located within the condensational layer (850-550 hPa), but they also expanded all the way to the surface (550-1000 hPa). Our interpretation of the moisture and potential temperature PV sensitivities (see figure 35) was that they suggested that the front associated with Nina should become stronger, in agreement with the KE moisture and potential temperature sensitivities. The stronger front would cause the mid-level PV at 09 UTC 10 January 2015 to become stronger

and can be explained in the same way as the KE moisture and potential temperature sensitivities, via enhanced moist ascent leading to a stronger positive PV anomaly and increased incipient cyclonic circulation. Our interpretation of the zonal wind sensitivity (see figure 36a and c) was that it suggested that a stronger incipient circulation at aproximately 950 hPa would cause increased intensity of the mid-level PV at 09 UTC 10 January 2015. We think that the meridional wind sensitivity (see figure 36b and d) suggested stronger southerly flow to the east of the center of the cyclone and a stronger southerly flow to the west of the center of the cyclone would increase the mid-level PV three hours before landfall. This may also be interpreted as a suggestion of a stronger incipient cyclonic circulation at 00 UTC 9 January 2015. When we added the optimal perturbation pressure evolved in the NLM to the mean SLP at 09 UTC 10 January 2015 (see figure 38), we found that the NLM field at 00 UTC 9 January 2015 could be perturbed in such a way that Nina evolved further south closer to the location suggested by the analysis fields (see figure 39). We were successful in showing that perturbations of the NLM field within the sensitivities from the AM can change the track of Nina.

We also investigate the cause of the largest positive moisture sensitivity found with both KE and PV as the response function (see figure 33 and 37).For both cases this moisture sensitivity was located on a frontal structure behind Nina. This maximum positive moisture sensitivity was large and very confined, which made it interesting to investigate it closer. It seems that this maximum positive moisture sensitivity was associated with a pocket of drier air relative to the ambient region and that it was located at approximately 850-600 hPa altitude (see figure 33b and 37b). This pocket of air had a relative humidity of 30-60 %, much lower than the ambient region which had a relative humidity of 60-100 %. Both KE and PV suggested that if the moisture content within this drier pocket was increased, it would increase the storm intensity at landfall. The large sensitivity to the dry pocket signifies, yet again, the importance of moisture with respect to Nina.

Following the method of Boettcher and Wernli (2013), we have sufficient evidence to conclude that Nina evolved similar to a DRV. The sensitivity backs up the results from the synoptic analysis because of Nina's large sensitivity to moisture and due to the large sensitivities located at 850-500 hPa ahead of Nina in the forcing region of a DRV. We think that the KE and PV sensitivities suggest that the front associated with Nina should increase in strength to increase the storm at landfall. A stronger front could be linked to enhanced moist ascent and a stronger diabatically produced positive PV. Moisture is the primary driver of cyclogenesis for a DRV, thus the results from the sensitivity analysis underscores our conclusion that Nina evolved similar to a DRV.

7 Suggestions of Further Research

During our synoptic analysis criterion two, a PV anomaly of 0.8 PVU co-located with the minimum SLP, was not fulfilled. We suggest that further research as to why this criterion was not fulfilled should be performed. Criterion two might not have been fulfilled simply due to the fact that we did not use the same data as Boettcher and Wernli (2013) or the unfulfillement of the criterion could mean that Boettcher and Wernli (2013) set their threshold to high or it could be linked to the dynamics of Nina. In addition, a PV inversion should be performed during Nina so that we can quantify the upper level forcing ($<$650 hPa) relative to the low level forcing ($>$ 750 hPa) at 700 hPa. This could be done by following for instance Deveson *et al.* (2002). In Deveson *et al.* (2002) they solve the QG-omega equation by following Clough *et al.* (1996). The solution by Clough *et al.* (1996) allows quantification of the omega and this would show relative contribution from this variable from $>$ 650 hPa (the upper levels) and $>$750 hPa (the lower levels) at 700 hPa.

The sensitivities with respect to Nina were very complex. We focused on the sensitivities located ahead of Nina and the moisture sensitivity of largest magnitude located on the frontal structure behind Nina. Suggestions of further research could be finding the cause of the dry pocket which the moisture was very sensitive to and investigating the complex sensitivities located southwest of Nina. Other possible experiments could be to move the response function box, or make it larger or deeper. A dry experiment could also be performed. The dry experiment would involve removing all moisture in the atmosphere. The removal of all moisture in the atmosphere would indicate the importance of moisture with respect to the strength and evolution of Nina. Another suggestion of further research is nesting (see for instance Doyle *et al.* (2013)). Nesting refers to an increase of the resolution as we move closer to the response function box.

References

Amerault C, Zou X, Doyle JD. 2008. Tests of an adjoint mesoscale model with explicit moist physics on the cloud scale. *Mon. Wea. Rev* **136**: 2120–2132, doi:10.1175/2007MWR2259. 1.

American Meteorological Society. 2016. Glossary of Meteorology. `http://glossary. ametsoc.org/wiki/Equivalent_potential_temperature`.

Arakawa A, Lamb VR. 1977. Computational design of the basic dynamical processes of the ucla general circulation model. *Methods in Computational Physics* **17**: 173–265, doi:10.1016/B978-0-12-460817-7.50009-4.

Boettcher M, Wernli H. 2013. A 10-yr climatology of diabatic rossby waves in the northern hemisphere. *Mon. Wea. Rev.* **141**: 1139–1154, doi:10.1175/MWR-D-12-00012.1.

Burrows HD, Weir RD, Stohner J. 1990. Pure and applied chemistry. *The Scientific Journal of IUPAC* **62**: 2167–2219, doi:10.1080/10601325.2016.1176439.

Chen S, *et al.* 2003. COAMPS Version 3 Model Description - General Theory and Equations. Available at: `http://www.nrlmry.navy.mil/coamps_docs/base/docs/COAMPS_ 2003.pdf`, version 3.

Clough SA, Davitt C, Thorpe AJ. 1996. Attribution concepts applied to the omega equation. *Q.J.R. Meteorol. Soc.* **122**: 1943–1962, doi:10.1002/qj.49712253610.

Dacre HF, Hawcroft MK, Stringer MA, Hodges KI. 2012. An extratropical cyclone atlas: A tool for illustrating cyclone structure and evolution. *Bull. Amer. Meteorol. Soc.* **n/a**: 1497–1502, doi:10.1175/BAMS-D-11-00164.1.

Davies-Jones R. 2009. On formulas for equivalent potential temperature. *Mon. Wea. Rev.* **137**: 3137–3148, doi:10.1175/2009MWR2774.1.

Deveson A, Browning K, Hewson T. 2002. A classification of FASTEX cyclones using a height attributable quasi-geostrophic vertical-motion diagnostic. *Q.J.R. Meteorol. Soc.* **128**: 93–117, doi:10.1256/00359000260498806.

Doyle JD, Amerault C, Reynolds CA, Reinecke AP. 2013. Initial condition sensitivity and predictability of a severe extratropical cyclone using a moist adjoint. *Mon. Wea. Rev* **142**: 320–342, doi:10.1175/MWR-D-13-00201.1.

Engdahl BJK. 2015. Hvorfor var nina saa vrang? `http://om.yr.no/2015/01/15/hvorfor-nina-var-sa-vrang/` (last accessed January 28, 2015).

Errico RM. 1997. What is an adjoint model? *Bull. Amer. Meteor. Soc.* **78**: 2577–2591, doi:10.1175/1520-0477(1997)078⟨2577:WIAAM⟩2.0.CO;2.

Errico RM, Reader KD. 1999. An examination of the accuracy of the linearization of a mesoscale model with moist physics. *Q.J.R. Meteorol. Soc.* **125**: 169–195, doi:10.1002/qj.49712555310.

Fink AH, Pohle S, Pinto JG, Knippertz P. 2012. Diagnosing the influence of diabatic processes on the explosive deepening of extratropical cyclones. *Geophysical Research Letters* **39**(7): n/a–n/a, doi:10.1029/2012GL051025.

Flagg D. 2013. COAMPS Visualization In Python (COVIP). Adapted from version available at: `http://code.google.com/p/pywrfplot/source/browse/trunk/example.py`.

GLOBE Task Team and others. 1999. The Global Land One-kilometer Base Elevation (GLOBE) Digital Elevation Model. Available at: `http://www.ngdc.noaa.gov/mgg/topo/globe.html`, version 1.0.

Gray S, Dacre H. 2006. Classifying dynamical forcing mechanisms using a climatology of extratropical cyclones. *Q.J.R. Meteorol. Soc.* **132**: 1119–1137, doi:10.1256/qj.05.69.

Harstveit K, Aune B. 1992. The storm of january 1. 1992. *The Norwegian Meteorological Institute* **23/92**: n/a.

Hartmann D. 1994. *Global physical climatology*. Academic Press: 525B Street, Suite 1900, San Diego, California 92101-4495, USA.

Hodur RM. 1997. The Naval Research Laboratory's Coupled Ocean Atmosphere Mesoscale Prediction System. *Mon. Wea. Rev.* **125**: 1414–1430, doi:10.1175/1520-0493(1997)125⟨1414:TNRLSC⟩2.0.CO;2.

Holton JR, Hakim GJ. 2012. *An introduction to dynamic meteorology, 5th edition*, vol. 88. Academic press: London, U. K.

Holton RJ. 1992. *An introduction to dynamic meteorology, 3rd edition*, vol. 48. Academic Press: London, U. K.

Hoskins BJ. 1982. The mathematical theory of frontogenesis. *Ann. Rev. Fluid Mech* **14**: 131–151, doi:10.1146/annurev.fl.14.010182.001023.

Hunter JD. 2007. Matplotlib: A 2d graphics environment. *Computing In Science & Engineering* **9**(3): 90–95, doi:10.1109/MCSE.2007.55.

Kalnay E. 2003. *Atmospheric modeling, data assimilation and predictability*. Cambridge University Press: New York, United States.

Klemp J, Wilhelmson R. 1978. The simulation of three-dimensional convective storm dynamics. *J. Atmos. Sci.* **35**: 1070–1096, doi:10.1175/1520-0469(1978)035⟨1070:TSOTDC⟩2.0.CO;2.

Liberato MRL, *et al.* 2013. Explosive development of winter storm xynthia over the subtropical north atlantic ocean. *Nat. Hazards Earth Syst.* **13**: 2239–2251, doi:10.5194/nhess-13-2239-2013.

Lorenz EN. 1965. A study of the predictability of a 28-variable atmospheric model. *Tellus* **17**: 321–333, doi:10.1111/j.2153-3490.1965.tb01424.x.

Louis JF. 1979. A parametric model of vertical eddy fluxes in the atmosphere. *Bound.-Layer Meteor.* **17**: 187–202, doi:10.1007/BF00117978.

Mahfouf J. 1999. Influence of physical processes of the tangent linear approximation. *Tellus* **51A**: 147–166, doi:10.1034/j.1600-0870.1999.00001.x.

Markowski P, Richardson Y. 2010. *Mesoscale meteorology in midlatitudes*. Wiley-Blackwell: Hoboken, New Jersey, United States.

Molinari J. 1985. General form of kuo's cumulus parameterization. *Mon. Wea. Rev* **113**: 1411–1416, doi:10.1175/1520-0493(1985)113⟨1411:AGFOKC⟩2.0.CO;2.

Moore RW, Montgomery MT. 2004. Reexamining the dynamics of short-scale, diabatic Rossby waves and their role in midlatitude moist cyclogenesis. *jas* **61**: 754–768, doi:10.1175/1520-0469(2004)061⟨0754:RTDOSD⟩2.0.CO;2.

Moore RW, Montgomery MT, Davies H. 2008. The integral role of a diabatic Rossby vortex in a heavy snowfall event. *Mon. Wea. Rev.* **136**: 1878–1897, doi:10.1175/2007MWR2257.1.

Moore, R W, Private Communication. 2016.

National Academy of Sciences. 1963. *Ocean wave spectra.* Prentice Hall: Englewood Cliffs, New Jersey, USA.

Olsen AM, *et al.* 2015. Ekstremværrapport, hendelse: Nina 10. januar 2015. External extreme weather report of Nina, public version available at: `http://met.no/filestore/METinfo14-2015.pdf`.

Papritz L, Spengler T. 2015. Analysis of the slope of isentropic surfaces and its tendencies over the north atlantic. *Q. J. R. Meteorol. Soc.* : 1477–870doi:10.1002/qj.2605.

Parker DJ, Thorpe AJ. 1995. Conditional convective heating in a baroclinic atmosphere: a model of convective frontogenesis. *J. Atmos. Sci.* **52**: 1699–1711, doi: 10.1175/1520-0469(1995)052⟨1699:CCHIAB⟩2.0.CO;2.

Petterssen S, Smebye SJ. 1971. On the development of extratropical cyclones. *Q.J.R. Meteorol. Soc.* **97**: 457–482, doi:10.1002/qj.49709741407.

Pierce DW. 2016. Ncview: A netcdf visual browser.

Plant R, Craig G, Gray S. 2003. On a threefold classification of extratropical cyclogenesis. *Q.J.R. Meteorol. Soc.* **129**: 2989–3012, doi:10.1256/qj.02.174.

Raymond D, Jiang H. 1990. A theory for long-lived mesoscale convective systems. *J. Atmos. Sci.* **47**: 3067–3077, doi:10.1175/1520-0469(1990)047⟨3067:ATFLLM⟩2.0.CO;2.

Rommetveit A. 2014. Dette er tegn på farlig vær. `http://www.yr.no/artikkel/_-dette-er-tegn-pa-farlig-vaer-1.12002284` (Last accessed 1 June 2016).

Rutledge SA, Hobbs PV. 1983. The mesoscale and microscale structure of organization of clouds and precipitation in midla- titude cyclones. viii: A model for the "seeder-feeder" process in warm-frontal rainbands. *J. Atmos. Sci.* **40**: 1185–1206, doi:10.1175/1520-0469(1983)040⟨1185:TMAMSA⟩2.0.CO;2.

Sanders F, Gyakum J. 1980. Synoptic-dynamic climatology of the "bomb". *Mon. Wea. Rev.* **108**: 1589–1606, doi:10.1175/1520-0493(1980)108⟨1589:SDCOT⟩2.0.CO;2.

Schulzweida U, Kornblueh L, Quast R. 2009. CDO User's Guide. Available at: `https://www.rsmas.miami.edu/users/rajib/cdo.pdf`, version 1.4.1.

Snyder C, Lindzen RS. 1991. Quasi-geostrophic wave-CISK in an unbounded baroclinic shear. *J. Atmos. Sci.* **48**: 76–86, doi:10.1175/1520-0469(1991)048⟨0076:QGWCIA⟩2.0. CO;2.

Spengler, T, Private Communication. 2016.

Spensberger C. 2015. Welcome to dynlib's documentation! Documentation available at: `http://folk.uib.no/csp001/dynlib_doc/index.html`.

Stoelinga MT. 1996. A potential vorticity based study of the role of diabatic heating and friction in a numerically simulated baroclinic cyclone. *Mon. Wea. Rev.* : 849–874doi: 10.1175/1520-0493(1996)124⟨0849:APVBSO⟩2.0.CO;2.

Sun C. 2005. Equivalent-barotropic definition of tropospheric mean temperature. *J. Atmos. Sci.* **62**: 3172–3192, doi:10.1175/JAS3546.1.

Taylor GF. 1954. *Elementary meteorology.* Prentice-Hall: New York, United States.

Terpstra A. 2014. Dynamical perspectives on the formation and intensification of polar lows. PhD thesis, University of Bergen.

Ulbrich U, Fink AH, *et al.* 2001. Three extreme storms over europe in december 1999. *Weather* **56**: 70–80, doi:10.1002/j.1477-8696.2001.tb06540.x.

Vukicevic T, Errico RM. 1993. Linearization and adjoint of parameterized moist diabatic process. *Tellus* **45A**: 493–510, doi:10.1034/j.1600-0870.1993.0012.x.

Wallace JM, Hobbs PV. 2006. *Atmospheric science: An introductary survey.* Academic Press: Oxford.

Warner TT. 2011. *Numerical weather and climate prediction.* Cambridge University Press: New York, USA.

Wernli H, Davies HC. 1997. A Lagrangian-based analysis of extratropical cyclones. I: The method and some applications. *Q.J.R. Meteorol. Soc.* **123**: 467–489, doi:10.1002/qj. 49712353811.

Wernli H, Dirren S, Liniger MA, Zillig M. 2002. Dynamical aspects of the life cycle of the winter storm 'lothar' (24-26 december 1999). *Q.J.R. Meteorol. Soc.* **128**: 405–429, doi:10.1256/003590002321042036.

Wernli H, Schwierz C. 2006. Surface cyclones in the era-40 dataset (1958–2001). part i: Novel identification method and global climatology. *J. Atmos. Sci.* **63**: 2486–2507, doi: 10.1175/JAS3766.1.

Zhu Y, Newell R. 1994. Atmospheric rivers and bombs. *Geophys. Res. Lett.* : 1999–2002doi: 10.1029/94GL01710.

Zou X, Navon IM, Sela J. 1993. Control of gravitational oscillations in variational data assimilation. *Mon. Wea. Rev.* **121**: 272–289, doi:10.1175/1520-0493(1993)121⟨0272: COGOIV⟩2.0.CO;2.